

# ScholarWorks@GSU

## DMI Interaction and Domain Evolution in Magnetic Heterostructures with Perpendicular Magnetic Anisotropy

Authors	Nanayakkara, Jagodage Kasuni S
Citation	Nanayakkara, Jagodage Kasuni S. "DMI Interaction and Domain Evolution in Magnetic Heterostructures with Perpendicular Magnetic Anisotropy." 2018. Dissertation, Georgia State University. <a href="https://doi.org/10.57709/12006508">https://doi.org/10.57709/12006508</a>
DOI	<a href="https://doi.org/10.57709/12006508">https://doi.org/10.57709/12006508</a>
Download date	2026-06-06 19:43:08
Link to Item	<a href="https://hdl.handle.net/20.500.14694/12246">https://hdl.handle.net/20.500.14694/12246</a>

DMI INTERACTION AND DOMAIN EVOLUTION IN MAGNETIC  
HETEROSTRUCTURES WITH PERPENDICULAR MAGNETIC ANISOTROPY

by

JAGODAGE KASUNI NANAYAKKARA

Under the Direction of Alexander Kozhanov, PhD

ABSTRACT

My thesis is dedicated to the study of the magnetic interactions and magnetization reversal dynamics in ferromagnetic heterostructures with perpendicular magnetic anisotropy (PMA). Two related projects will be included: 1) investigating interfacial Dzyaloshinskii-Moriya interaction (DMI) in multilayer structures; 2) controlled stripe domain growth in PMA heterostructures. Magneto Optic Kerr Effect microscopy and magnetometry techniques along with vibrating sample magnetometry were used to investigate these phenomena.

The CoPt bi-layer system is a well-known PMA material system exhibiting DMI. However, films with many CoPt bi-layers are known as having zero effective DMI due to its inversion symmetry. I focused my research on CoNiPt tri-layer heterostructures with broken

inversion symmetry. In my project, the interfacial DMI as a function of the number of CoNiPt trilayers in multilayered films was investigated and non-zero DMI in this constructed “bulk” magnetic materials were observed. For the project of stripe domain manipulation, the CoNi bilayer system with PMA was studied. CoNi “bulk” multilayered materials with PMA allow for controlled direction of stripe domain growth. The formation of variable angle domain intersection segments is comprised of the stripe domains.

INDEX WORDS: PMA, DMI, MOKE, Multilayers, Domains, Domain walls

DMI INTERACTION AND DOMAIN EVOLUTION IN MAGNETIC  
HETEROSTRUCTURES WITH PERPENDICULAR MAGNETIC ANISOTROPY

by

JAGODAGE KASUNI NANAYAKKARA

A Dissertation Submitted in Partial Fulfillment of the Requirements for the Degree of

Doctor of Philosophy

in the College of Arts and Sciences

Georgia State University

2018

Copyright by  
Jagodage Kasuni Shermila Nanayakkara  
2018

DMI INTERACTION AND DOMAIN EVOLUTION IN MAGNETIC  
HETEROSTRUCTURES WITH PERPENDICULAR MAGNETIC ANISOTROPY

by

JAGODAGE KASUNI NANAYAKKARA

Committee Chair: Alexander Kozhanov

Committee: Unil Perera

Vadym Apalkov

Douglas Gies

Electronic Version Approved:

Office of Graduate Studies

College of Arts and Sciences

Georgia State University

May 2018

## **DEDICATION**

To my loving parents and husband.

## ACKNOWLEDGEMENTS

First of all, I wish to thank my advisor, Dr. Alexander Kozhanov for his valuable guidance, support, encouragement, and opportunities given me during the last four years of my Ph.D.

I am grateful to the former graduate director and my committee member Dr. Unil Perera, and other committee members Dr. Douglas Gies, Vadym Apalkov and former committee members Dr. Brian Thomes, Dr. Yohannas Abate for their advice and support during my time in Georgia State University. Also, I would like to thank my former advisor Dr. Nicoulus Dietz for his support during my first two and half years at Georgia State University. I want to extend my gratitude to all the professors in the Physics and Astronomy Department for teaching different areas of Physics.

I wish to express my gratitude to former group members, especially Madison Hanberry for developing LabVIEW programs which made it easy for me to collect data, and to Cody Kellog for his friendly discussions in research.

My special thanks to the technical staff including Pieter Walker and Sam Mayberry for helping my research by machining parts. I also take this opportunity to express my special gratitude to our lab coordinator Carola Butler for her support in teaching labs.

My special thanks to our collaborators in Emory, Dr. Urazhdin Sergey and his group for growing samples for our experiments.

I am privileged to have many good friends in GSU who provided great company during all the years. Thank you all my friends in GSU Physics and Astronomy department for being a part of my life during these past years at GSU.

Finally, I would like to thank my parents, husband, brother, and sister for their encouragement, support, and caring during this time.

## TABLE OF CONTENTS

ACKNOWLEDGEMENTS.....	V
LIST OF TABLES.....	IX
LIST OF FIGURES.....	X
LIST OF ABBREVIATIONS.....	XVIII
<b>1 INTRODUCTION .....</b>	<b>19</b>
<b>2 BACKGROUND THEORY .....</b>	<b>22</b>
<b>2.1 Ferromagnetism .....</b>	<b>22</b>
<b>2.2 Magnetic Interactions in Ferromagnetic Materials .....</b>	<b>23</b>
<b>2.3 Anisotropy .....</b>	<b>24</b>
<i>2.3.1 Magnetocrystalline Anisotropy.....</i>	<i>24</i>
<i>2.3.2 Shape Anisotropy.....</i>	<i>26</i>
<i>2.3.3 Magneto-elastic Anisotropy.....</i>	<i>27</i>
<i>2.3.4 Perpendicular Magnetic Anisotropy (PMA).....</i>	<i>27</i>
<b>2.4 Domain Structure .....</b>	<b>29</b>
<b>2.5 Domain Walls .....</b>	<b>32</b>
<b>2.6 Domain wall Observation.....</b>	<b>34</b>
<b>2.7 Magnetic Field induced Domain wall motion.....</b>	<b>35</b>
<b>2.8 Dzyaloshinskii –Moriya Interaction .....</b>	<b>39</b>
<i>2.8.1 LLG Model of Domain Wall Motion in the presence of DMI.....</i>	<i>40</i>

2.8.2	<i>Creep Theory of Domain Wall Motion in the presence of DMI</i> .....	41
2.9	Chiral Domain Walls and DMI.....	42
3	<b>EXPERIMENTAL METHODS</b> .....	55
3.1	Introduction.....	55
3.2	Samples and structures .....	55
3.3	Magneto-Optical Kerr Effect (MOKE) .....	55
3.3.1	<i>MOKE Theory</i> .....	55
3.3.2	<i>MOKE Geometries</i> .....	59
3.4	MOKE magnetometer with Phase Modulation.....	61
3.5	MOKE magnetometer without phase modulation .....	65
3.6	MOKE Microscopy .....	66
3.7	Vibrating Sample Magnetometer (VSM) .....	69
4	<b>DMI IN PT/CO/NI HETEROSTRUCTURES</b> .....	70
4.1	Introduction.....	70
4.2	Sample description .....	72
4.3	MOKE measurements and Domain wall motion .....	76
4.4	Extracting DMI in [Pt/Co/Ni] <sub>n</sub> heterostructures. ....	82
4.5	Conclusion .....	89
5	<b>STRIPE DOMAIN MANIPULATION IN MAGNETIC MULTILAYER STRUCTURES WITH PMA</b> .....	90

<b>5.1</b>	<b>Introduction.....</b>	<b>90</b>
<b>5.2</b>	<b>Sample Description.....</b>	<b>91</b>
<b>5.3</b>	<b>MOKE measurements and domain evolution .....</b>	<b>93</b>
<b>5.4</b>	<b>Conclusion .....</b>	<b>103</b>
<b>6</b>	<b>SUMMARY .....</b>	<b>104</b>
	<b>REFERENCES .....</b>	<b>106</b>
	<b>APPENDICES .....</b>	<b>111</b>
	<b>Appendix A: Electromagnet design.....</b>	<b>111</b>
	<i>Appendix A.1 FEMM simulations of magnetic field calculation for the designed electromagnet. ....</i>	<i>111</i>
	<i>Appendix A.2 CAD designs of the electromagnet. ....</i>	<i>112</i>

**LIST OF TABLES**

<b>Table 4-1</b> The coercive fields of [PtCoNi] <sub>n</sub> extracted from the hysteresis loops.....	75
<b>Table 4-2</b> The calculated parameters for the DW velocity fitting .....	84
<b>Table 4-3</b> The variable fitting parameters obtained from the creep model fits with Bloch-Neel DW, and pure Neel DW conditions on experimental DW velocity vs. in-plane field graphs.....	87
<b>Table 5-1</b> The coercive fields of [CoNi] <sub>n</sub> extracted from hysteresis loops .....	92

## LIST OF FIGURES

<b>Figure 2.1</b> Bathe-Slater curve for the ferromagnetic and ferrimagnetic materials. The exchange integral is plotted as a function of interatomic spacing [15]. .....	24
<b>Figure 2.2</b> The graph of Effective anisotropy times Co thickness Vs. Co thickness for Co/Pd multilayers. The slope indicates the volume anisotropy contribution while the Y intercept yields the interface anisotropy contribution [23]. .....	28
<b>Figure 2.3</b> Domain formation to reduce the magnetostatic anisotropy .....	30
<b>Figure 2.4</b> (a) The closure domain formation. (b) The extended domain structure due to the magnetostrictive energy. ....	31
<b>Figure 2.5</b> The sketch of a $180^0$ domain wall. ....	32
<b>Figure 2.6</b> (a) The schematic of magnetic moments rotation in Neel domain walls and Bloch domain walls. (b) domain wall energy density and (c) domain wall width as a function of the film thickness [27, 28]. ....	33
<b>Figure 2.7</b> The schematic of precession of magnetic moments rotation with an external magnetic field. The red arrow indicates the direction of torque that arises from the external magnetic field and the blue arrow shows the damping vectors [34, 35]. ....	36
<b>Figure 2.8</b> The schematic of domain wall motion with an external magnetic field [36]. ....	36
<b>Figure 2.9</b> Hysteresis measured on $[\text{CoNi}]_6$ using MOKE microscopy. 1, 2, and 3 images show the domain nucleation and growth at the different external magnetic fields. ....	38
<b>Figure 2.10</b> The domain wall velocity as a function of external magnetic field, at three different regimes depending the strength of applied magnetic field [39]. ....	39
<b>Figure 2.11</b> The schematic representation of the Dzyaloshinskii-Moriya interaction in the Ferromagnetic(gray color)/ heavy metal (blue color) interface. $S_i$ and $S_j$ are the neighboring	

atomic spins in the ferromagnetic system which are coupled through a heavy metal atom due to the spin orbit interaction. ....40

**Figure 2.12** LLG model of domain wall motion in the presence of DMI field, in-plane and out-of-plane magnetic fields in a ferromagnetic layer with PMA. The color lines indicate the position of the domain wall at different times [45]. ....41

**Figure 2.13** The Spin Polarized Low Energy Electron Microscopic (SPLEEM) images of the Fe/Ni bilayers on Cu. (a), (b) and (c) indicates the magnetization components along Z, X, and Y directions respectively. (d) Compound SPLEEM image indicates right-handed, in-plane DW magnetization point from  $+M_z$  to  $-M_z$ . (e) magnetic moment configuration of the corresponding right-handed chiral DW structure. (f) reversing the bilayer growth order leads to left-handed chiral Neel walls observed. (g) left-handed chiral magnetic moment texture across the domain wall in (f) [48]. ....42

**Figure 2.14** The compound SPLEEM images of the Fe/Ni bilayers on Cu. Fe thickness increases while keeping Ni thickness fixed. (a), (b), (c), (d), (e), (f), (g), indicates domain width decreases as the Fe thickness is increased. Right-handed Neel DW configuration transform into Bloch walls at higher thickness. [48]. ....43

**Figure 2.15** The compound SPLEEM images of  $[\text{Co/Ni}]_n/\text{Pt}$ . (a) right-handed chiral Neel domain walls, (b) achiral Bloch domain walls, (c) left-handed chiral Neel domain walls, can be observed at different Ir thicknesses. (d) Ir thickness dependence on the angle  $\alpha$  ( $\alpha$  is the angle between the magnetization vector at the center of the DW and the normal vector of the DW) [49]. ....44

**Figure 2.16** DMI constant for the bilayers as a function of total thickness [52]. ....46

**Figure 2.17** (a) The MOKE image of symmetric bubble domain growth with out-of-plane magnetization. The magnetization inside the bubble domain is along the +Z direction. (b) The asymmetric bubble domain growth with both in-plane field ( $H_x$ ) and the out-of-plane field ( $H_z$ ). (c) The asymmetric velocity contour with the fields  $H_x$  and  $H_z$  [53]. .....47

**Figure 2.18 (A)** The differential MOKE images of DW motion of Pt/Co/Ir/Pt with in-plane and out-of-plane magnetic fields. (a) Structure with zero Ir (b) Ir thickness is 2.3 Å (c) Ir thickness is 4.6 Å. (d) The domain wall velocity as a function of in-plane field for different Ir thickness. **(B)** The bubble domain expansion for (b) epitaxial (d) for sputtered samples [54]. .....48

**Figure 2.19** Bubble DW motion with magnetic fields. (a) Bloch DWs have same energy density which expands the bubble domain symmetrically with the out-of-plane magnetic field. (b) positive DMI has Neel DWs pointing outward (white arrows), and negative DMI has Neel DWs pointing inward (purple arrow). (c) and (d) DW energy density profile for  $H_x$  in-plane magnetic field [55]. .....50

**Figure 2.20** (a) - (f) Domain Wall velocity as a function of in-plane magnetic field for different Ar pressure. Velocity variation increases as Ar pressure increases, but DW velocity asymmetry is the same. (g)-(l) DW velocity profile in logarithmic scale as a function of the in-plane field [55]. .....51

**Figure 2.21** The DMI field as a function of the deposition temperature for different base pressures [56]. .....52

**Figure 2.22** The field driven DW motion observation for Pt/[CoNi]<sub>4</sub>/X multilayer structures, where X is MgO, Cu, Pt, and Ta. (a) The schematic of the magnetization directions of the structure. (b) MOKE images of asymmetric DW motion with in-plane and out of plane magnetic fields. (c) The dependency of DW motion on in-plane magnetic field [57] .....53

<b>Figure 3.1</b> The schematic representation of three different MOKE geometries. (a) Polar MOKE (b) Longitudinal MOKE and (c) Transverse MOKE configurations for both s and p- polarized incident light. ....	60
<b>Figure 3.2</b> The experimental set up of MOKE magnetometer with phase modulation. ....	62
<b>Figure 3.3</b> The experimental set up of fast MOKE magnetometer without phase modulation. ....	65
<b>Figure 3.4</b> The experimental set up of MOKE microscope.....	67
<b>Figure 3.5</b> The MOKE microscopy domain images of CoNi heterostructure. (a) Direct domain image from the camera before image processing. (b) The same domain image after subtraction the saturated reference image. (Differential MOKE image). (c) The image after averaging 200 Differential MOKE images. ....	68
<b>Figure 3.6</b> The experimental set up Vibrating Sample Magnetometer. ....	69
<b>Figure 4.1</b> The sketch of the ferromagnetic structure of Pt/Co/Ni tri-layer repetition. n is the number of Pt/Co/Ni tri layer repetitions. The numbers in the brackets indicate the layer thickness in nm.....	73
<b>Figure 4.2</b> The out-of-plane hysteresis graphs of $[\text{Pt/Co/Ni}]_n$ heterostructures obtained from Vibrating Sample Magnetometer. (a) the hysteresis loop before the correction (b) the hysteresis loop after the correction. ....	74
<b>Figure 4.3</b> The modified hysteresis loops (after subtracting the paramagnetic effect from the substrate) of $[\text{Pt/Co/Ni}]_n$ heterostructures obtained from VSM. (a), (b), (c), (d), (e), and (f) indicates the hysteresis loops corresponding to the 1, 2, 3, 4, 5, and 10 tri-layer repetitions respectively. ....	75

**Figure 4.4** Schematic of sample and electromagnet alignment used in polar MOKE measurements. (a) MOKE geometry for the out-of-plane field measurements. (b) MOKE geometry for the combination of out-of-plan and in-plane magnetic field pulse application. ....76

**Figure 4.5** The MOKE images of symmetrical bubble domain expansion with two consecutive reverse magnetic field pulses with same pulse amplitude and duration (315 Oe, 400ms pulse). (a) bubble growth after the 1<sup>st</sup> field pulse. (b) bubble growth after the 2<sup>nd</sup> field pulse. ....77

**Figure 4.6** The differential MOKE image domain wall expansion during 315 Oe, 400ms, +Z magnetic field pulse. (a) The image of the domain structure before applying the 315 Oe, 400ms, +Z field pulse (reference image). (b) The image of the domain structure after applying the 315 Oe, 400ms, +Z field pulse. (c) The differential MOKE image which represents the domain wall displacement during the 315 Oe, 400ms, +Z field pulse. ....78

**Figure 4.7** The differential MOKE images of the  $[\text{Pt}/\text{Co}/\text{Ni}]_n$  heterostructures show the anisotropic domain wall displacement parallel to the in-plane field direction. (a) 315 Oe, 400ms pulse (b) 582 Oe, 1000ms pulse (c) 790 Oe, 20000ms pulse (d) 1000 Oe, 6000ms pulse (e) 66800 Oe, 4000ms pulse (f) 60000 Oe, 4000 ms indicate 1, 2, 3, 4, 5, and 10 repetitions of the tri-layer, respectively. The domain wall shape changes from a smooth bubble domain to rough bubble type domain as the number of repetitions increases. The highest DW asymmetry is observed for the 3-layer repetition, which indicates the strongest DMI. ....80

**Figure 4.8** Dependence of DW displacement on the magnetic field pulse duration. Black dots indicate the experimental data and the red line represents the linear best fit. (a) along (b) against the in-plane field for the 1 tri-layer repetition. (c) along (d) against the in-plane field for the 5 repetitions of tri-layers. ....83

**Figure 4.9** Bloch-Neel DW fit on the graphs of logarithmic DW velocity as a function of in-plane magnetic field for  $[\text{PtCoNi}]_n$ . Black dots indicate experimental data and red curves indicate the best fits of the creep model. (a)  $[\text{PtCoNi}]_1$ , (b)  $[\text{PtCoNi}]_2$ , (c)  $[\text{PtCoNi}]_3$ , (d)  $[\text{PtCoNi}]_4$ , and (e)  $[\text{PtCoNi}]_5$ .....85

**Figure 4.10** Pure Neel DW fit of experimental data of DW velocity as a function of in-plane magnetic field for  $[\text{PtCoNi}]_n$ . (a)  $n=1$ , (b)  $n=2$ , (c)  $n=3$ , (d)  $n=4$ , and (e)  $n=5$ . Black dots indicate the experimental data and red curves indicate the best fits of the creep model.....86

**Figure 4.11** The graph of calculated DMI field with pure Neel condition and the Bloch-Neel condition for 1-5 repetitions of Pt/Co/Ni. ....88

**Figure 5.1** The sketch of the ferromagnetic  $[\text{CoNi}]_n$  structure.  $n$  is the number of CoNi bilayer repetitions. The numbers in the brackets indicate the layer thickness in nm. ....91

**Figure 5.2** The hysteresis loops of  $[\text{CoNi}]_n$  heterostructures obtained from Vibrating Sample Magnetometer. (a)  $n=8$ , (b)  $n=9$ , (c)  $n=10$ .....92

**Figure 5.3** MOKE images of domain evolution of  $[\text{CoNi}]_9$  with out-of-plane magnetic field. (a)-(c) The nucleated domain grows isotopically in the form of a dendritic type domain with continuous field pulses. (a) 200Oe, 100ms first field pulse (b) 200Oe, 100ms second field pulse (c) 200Oe, 100ms third field pulse.....93

**Figure 5.4** MOKE images of domain evolution with out-of-plane magnetic field. (a)  $H_z=220\text{Oe}$ , 150ms (b)  $H_z=200\text{Oe}$ , 300ms (c)  $H_z=78\text{Oe}$ , 200ms (d) formation of new nucleation centers while the existing centers are growing. The black color indicates the grown domain with the previous field pulse and red color indicates growth of new domains. ....94

**Figure 5.5** The MOKE images of domain evolution of a nucleation center for  $[\text{CoNi}]_n$ , with the in-plane field plus a small out-of-plane field component. (a)  $H_{ZN}=180\text{Oe}$ , 100ms;  $H=1050\text{Oe}$ ,

300ms (b)  $H_{ZN}=200\text{Oe}$ , 100ms;  $H=1980\text{Oe}$ , 100ms (c)  $H_{ZN}=110\text{Oe}$ , 100ms;  $H=950\text{Oe}$ , 200ms  
 .....96

**Figure 5.6** MOKE images of domain evolution in  $[\text{CoNi}]_9$  from (a) nucleated domain;  $H_{ZN}=200\text{Oe}$ , 100ms;  $H=1980\text{Oe}$ , 100ms (b) middle sized domain;  $H_{ZN}=200\text{Oe}$ , 140ms;  $H=1900\text{Oe}$ , 100ms, (c) Large sized domain;  $H_{ZN}=200\text{Oe}$ , 180ms;  $H=1850\text{Oe}$ , 100ms. The domain structure formed with reverse field is shown by the solid green color. The stripe domains growth along the in-plane field are shown by red color.  $H_{ZN}$  is the reverse field which formed the domains. ....97

**Figure 5.7** Kerr images of possible independent domain growth along two different in-plane magnetic field directions  $H_1=1900\text{Oe}$ , 100ms and  $H_2=1900\text{Oe}$ , 100ms on  $[\text{Co/Ni}]_9$ . (a) domains grow starting from the same nucleation center in both directions. (b), (c) domains start to grow from different nucleation centers for the two different growth directions. ....99

**Figure 5.8** Probability distribution of stripe domain length measured at 1980 Oe, 100 ms field pulse. .... 100

**Figure 5.9** MOKE images of stripe domain manipulation by varying the in-plane magnetic field direction. Stripe domain turns by (a)  $90^\circ$  and (b)  $130^\circ$  in  $[\text{CoNi}]_9$  structure.  $H_{ZN}=200\text{Oe}$ , 100ms;  $H=1900\text{Oe}$ , 100ms. Stripe domain turns by (c)  $90^\circ$  and (d)  $130^\circ$  in  $[\text{CoNi}]_{10}$  structure.  $H_{ZN}=110\text{Oe}$ , 100ms;  $H=950\text{Oe}$ , 200ms. The  $H_1$  is the first field pulse direction and  $H_2$  is the second field pulse direction. .... 101

**Figure 5.10** Kerr images of complex geometry of stripe domain manipulation with in-plane magnetic field as field turns by  $90^\circ$  in (a),  $45^\circ$  in (b), and in a circle segment in (d), for  $[\text{Co/Ni}]_9$  structure and by  $90^\circ$  for  $[\text{Co/Ni}]_{10}$  structure in (c). The direction A indicates the primary field direction of magnetic field rotation and direction B is the field direction at the critical angle. ... 102

**Figure 0.1** FEMM simulations of electromagnet considering axisymmetric (a) Mesh generation and Material parameters. (b) Analysis results with the Flux density plot.....111

**LIST OF ABBREVIATIONS**

DMI – Dyzalooshinskii-Moriya Interaction  
MOKE – Magneto Optical Kerr Effect  
PMA – Perpendicular Magnetic Anisotropy  
VSM – Vibrating Sample Magnetometer  
DW – Domain Wall  
MRAM – Magnetic Random Access Memory  
LLG – Landau-Lifshitz-Gilbert  
FM– ferromagnetic  
PEM– Photoelastic Modulator  
SPLEEM– Spin-Polarized Low Energy Electron Microscopy  
FEMM– Finite Element Method Magnetics  
FVMSW– Forward Volume Magnetostatic Spin Wave

## 1 INTRODUCTION

The world storage technology has transformed rapidly from analog storage methods such as paper, film, videotape to digital storage methods like hard disks, and memory cards over the last two decades [1]. Due to the high demand, computing and digital storage devices have reached their limitations in speed, capacity, and scalability. Conventional memory and logic devices utilize the charge of the electrons to perform memory and logic operations. The information is stored in the form of storing electrons in a capacitive device. The logic operations are performed by controlling the flow of electrons. The single unit of the conventional electronics is the transistor, and its further development is limited by its high power consumption and size.

The spin property of electrons enables new functionalities in the area of Spintronics. Spintronics has influenced the evolution of nonvolatile magnetic memory devices such as Magnetic hard disk drive, Magnetic Random Access Memory (MRAM) to 3D Solid State Racetrack memory. Magnetic storage and logic devices do not consist of transistors to perform operations and the information is carried by the spin of the electrons. Therefore, magnetic memory and logic devices show a higher performance and lower power consumption than conventional electronic devices. In Magnetic hard disk drives data is stored in small magnetic regions. Spin valves based on the Giant Magneto Resistance[2-5] and magnetic tunneling junction devices[6, 7] improve the scalability and the information detecting sensitivity in magnetic hard disk drives. The developed MRAM has higher performance (fast reading and writing) than the hard disk drive but has the same storage capacity. The existing domain-based magnetic hard disk drives have reached their limits of scalability. Spin-based 3D memory and storage devices such as Magnetic Racetrack Memory are proposed as one possibility to overcome this limitation. The other possibility is implementing nanometer-scale domain structures which are called "skyrmions" in storage devices.

Skyrmions are topologically stable chiral domain structures on the nanometer scale that have governed a great interest in high information storage densities in memory device applications[8, 9]. Skyrmions can be observed with the Dzyaloshinskii Moriya interaction (DMI) in material systems which have favorable chiral domain wall structures. The stability and the nanometer scale of skyrmions enhance the capability of high information storage at very small scales.

The domain wall based logic architecture which is called "Magnetic Domain wall Logic" is reported [10]. Domain wall logic exhibits a low heating only at data switching in comparison to transistor-based conventional logic. The domain wall dynamics and pinning which causes the propagation delay ( $\sim 0.1-2$  ns) are needed to be investigated.

Investigating the material systems having chiral domain wall structure and understanding domain wall motion are essential for the development of future memory and logic devices. The thin magnetic material combinations which exhibit chiral domain walls and DMI are needed to build thick multilayer structures for device applications. Therefore, magnetic multilayer structures which enhance the DMI to sustain strong chiral domain wall textures were investigated. Current driven domain wall studies are needed using a lithographic technique to drive current in the structure. Therefore, the direct field-driven domain wall motion method is of a great interest in the area of domain wall motion storage applications. Narrower domain walls are essential to optimize the capacity of memory devices. The domain walls observed in ferromagnetic materials with Perpendicular Magnetic Anisotropy (PMA) are much narrower than those in soft magnetic materials.

In chapter 2, the basic theory and concepts in the area of ferromagnetic structures with Perpendicular Magnetic Anisotropy and DMI are introduced. The magnetic interactions, domains

and domain wall motion with an external applied magnetic field are discussed. DMI studies in ferromagnetic material systems with PMA are explained in greater detail.

Experimental methods and techniques used to obtain the results are explained in Chapter 3. The Magneto-Optical Kerr effect (MOKE) is the main experimental technique used to study magnetic properties of the structures and domain observation. Different experimental setups based on the MOKE theory are discussed. The image processing methodology used to observe the domain structures is explained.

Chapter 4 is dedicated to investigations of the DMI in Pt/Co/Ni multilayer structures. Symmetric domain growth in the presence of an out-of-plane magnetic field and the asymmetric domain wall motion with an in-plane magnetic field are discussed. Evolution of the shape of the domain wall from bubble to dendritic as the number of Pt/Co/Ni tri-layer repetition increases is explained. DMI values extracted for different multilayer structures and domain wall chirality are discussed.

Our recent discovery of stripe domain manipulation with an external out-of-plane and in-plane magnetic fields in Co/Ni multilayer structure is reported in chapter 5. Stripe domain manipulation for different Co/Ni bilayer repetitions with varying the in-plane field direction is explained.

## 2 BACKGROUND THEORY

### 2.1 Ferromagnetism

Magnetic materials can be categorized as diamagnetic, paramagnetic, antiferromagnetic, ferromagnetic and ferrimagnetic according to the ordering of the magnetic moments of the material. All the magnetic materials, except ferromagnetic and ferrimagnetic, require rather high external magnetic fields to cause small changes in the magnetization of the material. Ferromagnetic materials are of great interest in the area of spintronics due to the higher thermal stability (higher Curie Temperature) than that of ferrimagnets [11].

Ferromagnetic materials such as Ni, Co exhibit parallel magnetic moment ordering and they have a larger susceptibility than diamagnetic and paramagnetic materials. Therefore, by applying a small magnetic field on ferromagnetic materials, comparatively a larger magnetization than the diamagnetic or paramagnetic materials could be obtained. Once the ferromagnetic material is saturated, usually a non-zero magnetization exists even without any external magnetic field.

Ferromagnetic materials become paramagnetic above the Curie temperature ( $\theta$ ), and then the susceptibility ( $\chi$ ) behaves according to the Curie-Weiss law,  $\chi = C/(T - \theta)$  where  $C$  is the Curie constant per gram. It was first explained by Weiss (1907) introducing a “molecular field ( $H_m$ )” to the system.  $H_m$  is directly proportional to the magnetization, hence can be written as  $H_m = \gamma M$  where  $\gamma$  is called the molecular field constant. The large  $\theta$  of the ferromagnetic materials causes a strong “molecular field” as  $\theta = \rho\gamma C$ . Here  $\rho$  is the density of the material. The existence of strong a "molecular field" at low fields, or even at zero field, can saturate the material which is called self-saturation or spontaneous magnetization. Spontaneous magnetization has been explained using the domain theory. In the demagnetized state, spontaneously magnetized small

areas which are called domains can be found. The magnetization direction of the individual domains is pointed in random directions such that the net magnetization becomes zero.

Later, in 1928 Heisenberg explained the origin of the “molecular field” using the exchange interaction [12, 13].

## 2.2 Magnetic Interactions in Ferromagnetic Materials

The interplay between the exchange, dipolar and Dzyaloshinskii-Moriya (DMI) interactions governs the magnetic properties of the ferromagnetic materials. Dipolar interaction is a weak, long-range coupling between two magnetic dipoles.

The exchange interaction is a strong, short-range interaction which arises due to the coupling between the adjacent magnetic moments. The exchange interaction defines the magnetic ordering of the material to be either ferromagnetic or antiferromagnetic depending on the interatomic distances. The exchange energy between the two atoms  $i$  and  $j$  can be written as;

$$E_{exchange} = -2J_{ex}\mathbf{S}_i \cdot \mathbf{S}_j \quad (2.1)$$

Here,  $J_{ex}$  is the exchange integral and  $\mathbf{S}_i$ ,  $\mathbf{S}_j$  are the spin angular momentum of the  $i^{\text{th}}$  and the  $j^{\text{th}}$  atom. When the two atoms are very close, according to the Bathe-Slater curve [14] shown in Figure 2.1,  $J_{ex}$  is negative. Therefore, to have the minimum energy state, spins become antiparallel (antiferromagnetic), and this obeys the Pauli exclusion principle. As the interatomic distance increases,  $J_{ex}$  becomes positive, so that it favors the parallel spin configuration (ferromagnetic) to minimize the exchange energy. However,  $J_{ex}$  becomes zero as the interatomic distance increases further.

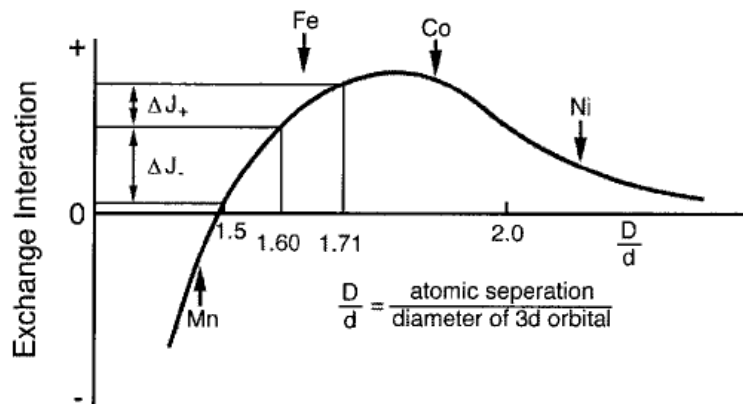


**Figure 2.1** Bath-Slater curve for the ferromagnetic and ferrimagnetic materials. The exchange integral is plotted as a function of interatomic spacing [15].

The antisymmetric exchange which is called DMI is explained in a later paragraph in this chapter.

## 2.3 Anisotropy

Magnetic anisotropy occurs where the magnetization of the material tends to lie in a certain preferred direction or directions. Magnetic anisotropy affects the shape of the hysteresis curve of the magnetic material. Crystal anisotropy (magnetocrystalline anisotropy), shape anisotropy and Magneto-elastic anisotropy are the important categories to understand the magnetic materials and are described below.

### 2.3.1 Magnetocrystalline Anisotropy

Magnetocrystalline anisotropy explains the tendency of aligning the magnetization along a preferred crystallographic direction. The spontaneous magnetization direction of the domains of cubic structures lay along the easy magnetization direction. A low magnetic field is enough to

saturate the magnetic structure along the easy axis by moving the domain walls. A relatively large magnetic field is required to saturate the structure along the hard axis to compensate the domain rotation other than the domain wall motion. The energy corresponds to the work done by the applied magnetic field against the anisotropy forces in the process of domain rotation and this energy is stored as the magnetocrystalline anisotropy energy. Magnetocrystalline anisotropy energy originates from the spin-orbit coupling. The applied magnetic field forces the axis of the spin to reorient along the field direction. Spin-orbit coupling forces the orbit of the electron to reorient with the new direction of the spin axis. However, the orbits have fixed orientation relative to the lattice due to the strong coupling. The energy needed to reorient the spin axis, i.e., the energy needed to overcome the spin-orbit interaction is called as the magnetocrystalline anisotropy energy. Body-centered cubic structures such as Fe have an easy magnetization direction along the  $\langle 100 \rangle$  direction while face centered cubic structures like Ni, and most of the ferrites except  $\text{CoFe}_2\text{O}_4$  have the easy axis along the  $\langle 111 \rangle$  direction. The magnetocrystalline anisotropy energy of cubic structures can be expressed in terms of the directional cosines of the angles between the  $\overline{M}_s$  and the crystal axes.  $\alpha_1, \alpha_2, \alpha_3$  are the directional cosines of those angles. Then, anisotropy energy can be expressed as:

$$E = K_0 + K_1(\alpha_1^2\alpha_2^2 + \alpha_2^2\alpha_3^2 + \alpha_3^2\alpha_1^2) + K_3(\alpha_1^2\alpha_2^2\alpha_3^2) + \dots \quad (2.2)$$

$K_0, K_1,$  and  $K_2$  are constants for a particular material at a given temperature and measured in  $\text{J/m}^3$  (SI) and depend on the material and the temperature.  $K_0$  is less significant as it does not depend on the angle between  $\overline{M}_s$  and the crystal axes.

Hexagonal close-packed structures like Co have magnetization easy axis aligned along the  $[0001]$  direction. That leads spontaneously magnetized domains to orient parallel and antiparallel

to the [0001] direction. The anisotropy energy can be written in terms of the single angle ( $\theta$ ) between the [0001] axis and the  $\overline{M}_s$  as follows.

$$E = K_0 + K_1(\sin \theta)^2 + K_2(\sin \theta)^4 + \dots \quad (2.3)$$

where  $K_0, K_1, K_3$  are constants [12].

### 2.3.2 Shape Anisotropy

Usually, polycrystalline materials have zero net magnetocrystalline anisotropy but domains orient along the easy magnetization axis along long axis of the shape due to the long-range magnetic dipolar interactions. The demagnetizing field which points in the opposite direction to the applied field is weaker along the long axis than the short axis. Therefore, a lower external magnetic field is required along the long axis to saturate the magnetic structure.

The demagnetization field ( $H_d$ ) inside the material arises from the magnetization ( $M$ ) of the sample can be written as  $H_d = -NM$ ;  $N$  is the shape dependent demagnetization factor, and it is smaller along the long axis and larger along the short axis. Therefore, if an external field is applied along the long axis, the effective magnetic field along the axis is almost equal to the applied magnetic field. If the external field is applied along the short axis, most of the applied field goes to compensate the demagnetization field, hence the effective field along the short axis is small. Therefore, the magnetic structure can be magnetized more easily along the long axis than the short axis. Other competing anisotropy fields like magnetocrystalline anisotropy and magneto-elastic anisotropy require overcoming the demagnetizing field to rotate the magnetization from in-plane to an out-of-plane direction. For spherical structures, the same external field strength is required to magnetize along all the directions [13].

### 2.3.3 Magneto-elastic Anisotropy

The magnetization direction of a magnetic material can be changed by introducing strain to the system. Strain originates from lattice mismatch of different materials brought together, thermal expansion coefficient mismatch, and the deposition process. The magneto-elastic energy of a material with isotropic magnetostriction can be written as;

$$E_{me} = K_{\sigma} \sin^2 \theta \quad (2.4)$$

Where,  $K_{\sigma} = \frac{3}{2} \lambda \sigma$  is the stress anisotropy constant,  $\lambda$  is the magnetostriction constant defined as the fractional change in length between the demagnetized state and the saturated magnetization state,  $\sigma$  is the stress, and  $\theta$  is the angle between the direction of the magnetization relative to the direction of uniform stress [12].

### 2.3.4 Perpendicular Magnetic Anisotropy (PMA)

In magnetic films and multilayers, the magnetic anisotropy direction can be changed from the common in-plane direction to the out-of-plane direction by changing the thicknesses of each layer and the material combination. In materials with PMA, the direction of the magnetic moments of the ferromagnetic layer are perpendicular to the plane of the surface. Materials with PMA are important for magnetic information storage applications due to the existence of narrow domain walls which enhance the storage capacity.

The effective magnetic anisotropy  $K_{eff}$  has two terms; volume anisotropy  $K_v$  and surface anisotropy  $K_s$ . The  $K_v$  term is contributed by the volume magnetic moments, and negative  $K_v$  indicates the magnetization is aligning in the in-plane direction. The  $K_s$  term is caused by the interfacial magnetic moments, and positive  $K_s$  implies that the magnetization direction is perpendicular to the surface. Interface anisotropy was first predicted by Neel in 1954 [15] and then

experimentally observed for NiFe films grown on Cu (111) by Gradmann and Muller in 1968 [16]. PMA in multilayers was first observed for Co/Pd in 1985 [17] and later for Co based multilayers of Co/Pt, Co/Pd, Co/Au, Co/Ru, Co/Ir and Co/Ni [18-21].

The effective anisotropy  $K_{eff}$  ( $\text{Jm}^{-3}$ ) of a magnetic structure can be expressed using volume magnetic moment contribution and the surface magnetic moment contribution as follows [22]:

$$K_{eff} = K_v + 2K_s/t \quad (2.5)$$

Here,  $t$  is the thickness of the magnetic layer.

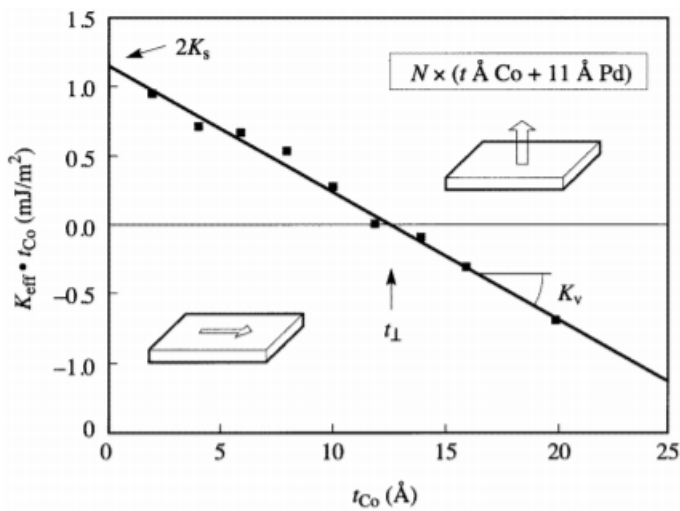


**Figure 2.2** The graph of Effective anisotropy times Co thickness Vs. Co thickness for Co/Pd multilayers. The slope indicates the volume anisotropy contribution while the Y intercept yields the interface anisotropy contribution [23].

The positive values of  $K_{eff} \cdot t$  shown in Figure 2.2 [22] indicate that magnetic structure favors the out-of-plane magnetization direction. The negative slope indicates that volume anisotropy contribution  $K_v$  prefers an in-plane magnetization direction. The positive Y intercept

denotes that the interface anisotropy contribution  $K_s$  favors out-of-plane magnetization. The critical thickness ( $t_{\perp}$ ) at which the magnetic anisotropy switches from out-of-plane to in-plane magnetization direction can be calculated by the expression  $-2 K_s / K_v$ . Below  $t_{\perp}$ , the magnetic structure shows PMA as interface anisotropy contribution compensates the volume anisotropy contribution. When the ferromagnetic layers are thin, interface effects become more prominent than bulk effects. Magnetocrystalline anisotropy is more prominent than the shape anisotropy [23].

The reported values of the interface anisotropies for Co, Fe are usually positive indicating an out-of-plane magnetization direction [21, 24], while they are typically negative for Ni. Anisotropy values for the same material show different values depending on the growth technique used, growth parameters and structural parameters like interface roughness. The critical thickness ( $t_{\perp}$ ) at which the magnetization easy axis direction transforms from in-plane to out-of-plane direction for Co multilayers is typically 0-25 Å depending on the structural properties of the material. It is typically smaller for Fe multilayers (0-10 Å) [24, 25]. It is reported that the interface roughness creates a demagnetization field along the in-plane axis and it reduces the shape anisotropy favoring PMA [26].

## 2.4 Domain Structure

In the demagnetization state of ferromagnetic materials, its magnetization breaks into regions with the collinear alignment of magnetic moments. These are called domains. The minimum energy comprised of magnetostatic energy, magnetocrystalline energy, magnetostriction energy and the exchange interaction energy defines the characteristic size of the domain structure.

In ferromagnets with uniaxial anisotropy (anisotropy with only one easy magnetization axis), magnetic moments are expected to be aligned along the easy axis in the demagnetization

state due to the exchange interaction. The single domain can be viewed as a magnet that produces a large demagnetizing field as shown in Figure 2.3(a). This demagnetization energy results in a large magnetostatic energy. The large magnetostatic energy can be reduced by splitting the magnetic structure into several regions with antiparallel magnetic moment alignment as in Figure 2.3(b). Likewise, by introducing small domains in the structure, the magnetostatic energy can be decreased while storing some portion of it in the domain wall. The equilibrium uniaxial domain size  $d_0$  is defined by at the balance between energies as follows:

$$d_0 = L \left( \frac{\sigma_{dw}}{\mu_0 M_s^2 t} \right)^{1/2} \quad (2.6)$$

where,  $L$  is the length and  $t$  is the thickness of the single crystal.  $\sigma_{dw}$  is the domain wall energy density which is described in greater detail in section 2.5.  $M_s$  is the saturation magnetization of the material.

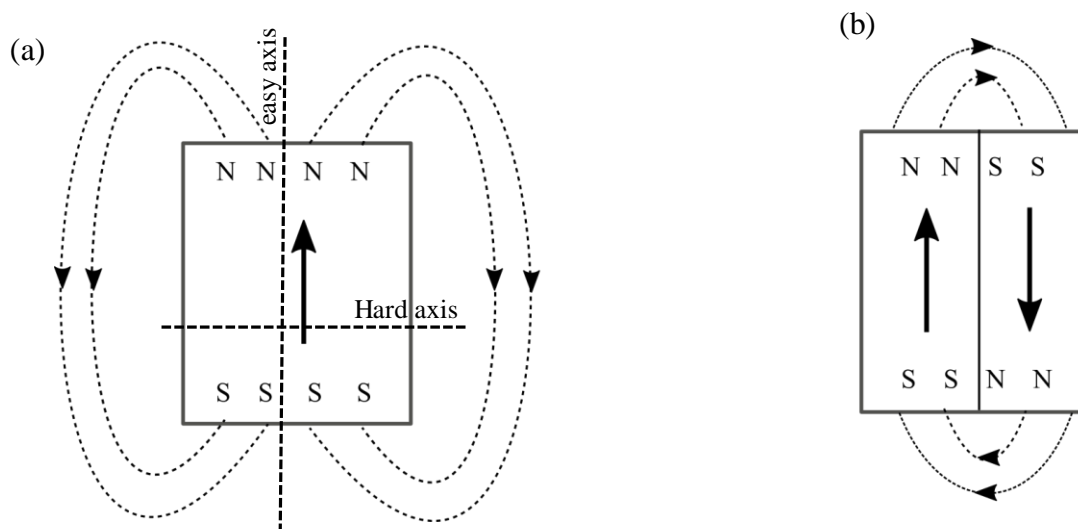


**Figure 2.3** Domain formation to reduce the magnetostatic anisotropy

The magnetization energy difference per unit volume between the easy axis and the hard axis is called as the magnetocrystalline energy. Cubic crystal structures have four easy magnetization axes. Magnetization aligns along one of the easy axes to minimize the magnetocrystalline energy. Domains typically form along the crystallographic easy axis directions. The magnetic flux forms the poles on the surface of the magnetic structure which is shown in Figure 2.3 (b). The triangular shape domains which are called as “closure domains” form to prevent the formation of surface poles by flowing flux in a closed path (Figure 2.4 (a)). If the film has positive magnetostriction, (length increase along the magnetization direction), there will be additional energy which is called magnetostrictive energy. The extended domain structures (Figure 2.4 (b)) gain strain energy (magnetostriction energy) which is proportional to the volume of the closure domain. Magnetostrictive energy can be minimized by decreasing the domain size of the structure. The minimum total energy which is a compromise of exchange energy, magnetostatic energy, magnetocrystalline energy and the magnetostrictive energy gives the final domain structure[12].

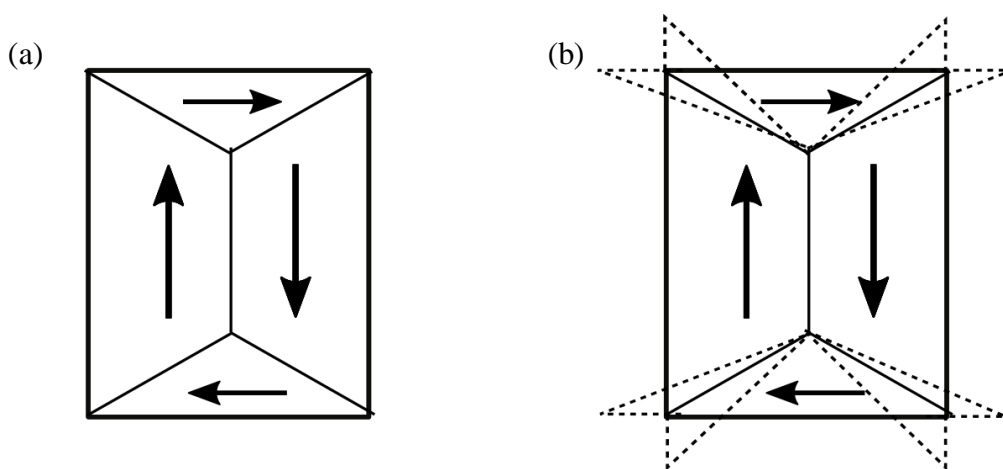


**Figure 2.4** (a) The closure domain formation. (b) The extended domain structure due to the magnetostrictive energy.

## 2.5 Domain Walls

Domain walls are the boundaries between the regions of different magnetization directions. The width of the domain wall is defined by the energy balance between the exchange energy and the magnetocrystalline anisotropy energy. In ferromagnetic materials, exchange energy is minimized for parallel alignment of the magnetic moments (Equation 2.1). Therefore, a wide domain wall structure is favored by exchange energy. The magnetic moments rotate in small rotation angles ( $\theta$ ) within the domain wall (Figure 2.5). In this case, the angle between neighboring magnetic moments is minimized. On the other hand, the magnetocrystalline anisotropy favors thin domain walls as magnetic moments are preferring to align along the easy axis. The energy tradeoff between exchange and magnetocrystalline energies defines the domain wall thickness.

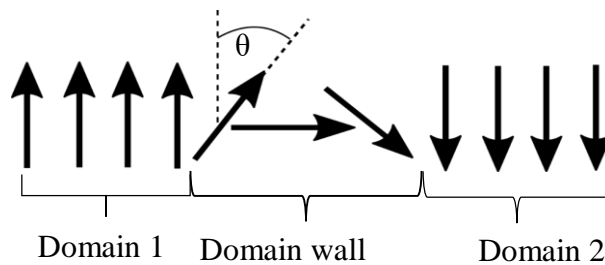


**Figure 2.5** The sketch of a  $180^\circ$  domain wall.

Two types of domain walls can be observed in ferromagnetic materials: Bloch walls and Neel walls. The most energetically favored domain walls are Bloch type of domain walls that can be observed in bulk magnetic materials. Here the magnetic moments rotate perpendicular to the sample plane as shown in Figure 2.6(a). In thin films, the magnetostatic energy related to the stray field from Bloch walls is comparatively larger than the exchange and anisotropy energies. Therefore, when the sample thickness is equivalent to the domain wall width, Neel type domain wall structure is dominant (Figure 2.6(b)) [27]. In Neel domain walls, magnetic moments rotate in the sample plane as shown in Figure 2.6 [28].

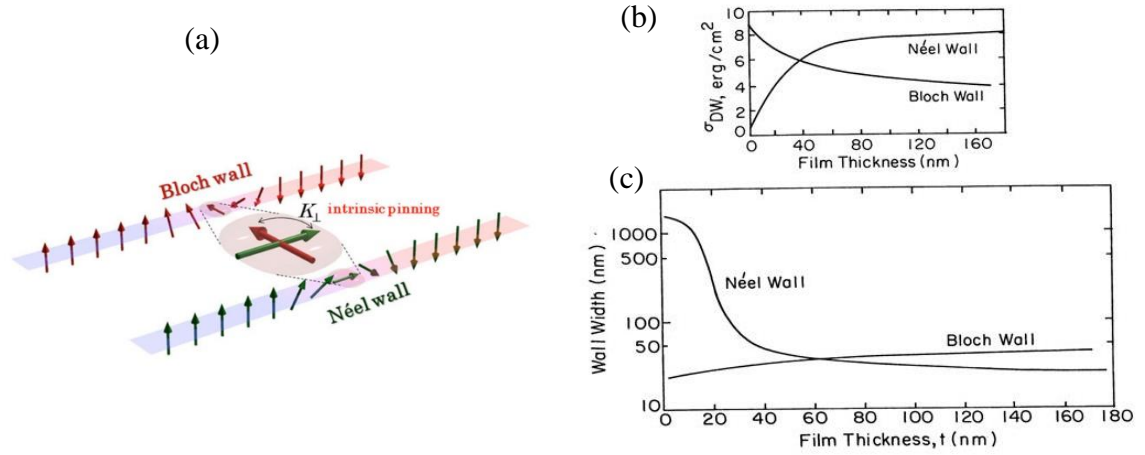


**Figure 2.6** (a) The schematic of magnetic moments rotation in Néel domain walls and Bloch domain walls. (b) domain wall energy density and (c) domain wall width as a function of the film thickness [27, 28].

The domain wall energy density of a  $180^\circ$  Bloch wall can be expressed as the sum of the magnetocrystalline anisotropy energy and the exchange energy as follows:

$$\sigma_{Anisotropy} + \sigma_{exchange} = K_u N a + J S^2 \frac{\pi^2}{N a^2} \quad (2.7)$$

where  $K_u$  is the uniaxial magnetocrystalline anisotropy,  $a$  is the lattice constant, and  $N$  is the number of atomic distances within the domain wall.

The minimized Bloch domain wall thickness  $\Delta_{Bloch}$  can be written as:

$$\Delta_{Bloch} = N_{min} a = \pi \left( \frac{A}{K_u} \right)^{1/2} \quad (2.8)$$

where the exchange stiffness constant  $A = J S^2 / a$ . The  $180^\circ$  Bloch domain wall energy density  $\sigma_{dw}$  at minimum domain wall thickness is:

$$\sigma_{Bloch\ dw} = 2\pi (A K_u)^{1/2} \quad (2.9)$$

The domain wall energy density of an  $180^\circ$  Neel domain wall can be written as a function of exchange energy, magnetocrystalline anisotropy energy, and the magnetostatic energy as follows;

$$\sigma_{magnetocrystalline} + \sigma_{exchange} + \sigma_{magnetostatic} = K_u \frac{Na}{2} + A \frac{\pi^2}{Na^2} + \left(\frac{2\mu_0 M^2}{\pi}\right) Na \arctan\left(\frac{t}{Na}\right) \quad (2.10)$$

where  $t$  is the film thickness. The Neel domain wall thickness  $\Delta_{Neel}$  at the minimum energy density is:

$$\Delta_{Neel} = N_{min} a = \pi \left(\frac{2A}{K_u}\right)^{1/2} ; \quad (t \ll \Delta_{Neel}) \quad (2.11)$$

The Neel domain wall energy density can be written as:

$$\sigma_{Neel dw} = \pi t M_S^2 \quad (2.12)$$

## 2.6 Domain wall Observation

The typical size of the domain is in the micron-scale. Microscopy techniques such as the Bitter method, Transmission electron microscopy, Magneto-optical effect and Magnetic force microscopy are used to observe domains and domain walls. In our experiments, we use Magneto-optical Kerr effect to observe domain structures and their evolution which is explained in greater detail in Chapter 3.

The Kerr technique has many advantages over the other methods. It is a non-destructive direct magnetization observation technique. The observation method does not affect the magnetization of the sample. It has the capability of observing fast dynamics such as fast domain growth. The same experimental set up can be used for domain imaging as well as for characterizing material (obtaining hysteresis loops) replacing and adding minimal other instruments (see Chapter 3).

The samples needed to be flat and smooth for the domain observation. Also, special techniques such as image processing have to be used to enhance the low contrast. Optical resolution is limited to 0.3  $\mu\text{m}$  [29].

## 2.7 Magnetic Field induced Domain wall motion

The process of changing the direction of the magnetization of the magnetic moments gradually without changing the position of the atoms is called domain wall motion. Domain walls can be moved either by applying an external magnetic field or electric current [30, 31]. Magnetic field-driven domain wall motion arises due to the torque applied to magnetic moments from the interaction of external magnetic field. The current induced domain wall motion results from the interaction between the spin of the conduction electron and the magnetic moments (spin torque).

Experimental implementation of current driven domain walls is critical as it requires lithographic techniques for injecting current [32]. Field-driven domain wall motion to extract DMI and manipulate domains is investigated in my studies.

The motion of magnetic moment with an external magnetic field can be described by the Landau-Lifshitz-Gilbert equation (Equation 2.15). As proposed by Landau and Lifshitz in 1935 [33], the magnetic moments experience a torque when the applied field is not parallel to the magnetization direction. That results in magnetic moment procession around the field axis. The torque of the magnetic moments can be written as:

$$\frac{\partial \vec{M}}{\partial t} = -\gamma \vec{M} \times \vec{H}_{eff} \quad (2.13)$$

where  $\gamma = \frac{g e \mu_0}{2 m_e}$  is the gyromagnetic ratio,  $g$  is the Lande factor, and  $\vec{H}_{eff}$  is the effective magnetic field. If the magnetic moments experience only this torque, they will process endlessly around the external field. Experimentally, magnetic moments are observed to experience damping and

relaxation along the effective field direction (Figure 2.7 [34]) [35]. The Landau-Lifshitz equation was modified by Gilbert adding the damping term [36]. The damping torque ( $T_d$ ) can be expressed as:

$$T_d = \alpha \vec{M} \times \frac{\partial \vec{M}}{\partial t} \quad (2.14)$$

where  $\alpha$  is the damping constant and  $\alpha > 0$ .

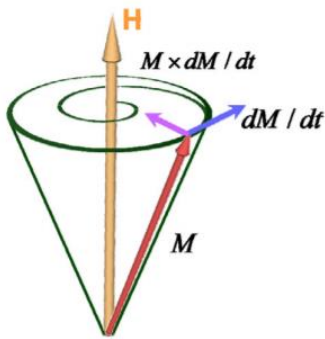


**Figure 2.7** The schematic of precession of magnetic moments rotation with an external magnetic field. The red arrow indicates the direction of torque that arises from the external magnetic field and the blue arrow shows the damping vectors [34, 35].

The Landau Lifshitz Gilbert (LLG) equation which describes the time and spatial evolution of a magnetic moment in the presence of the external magnetic field can be written as:

$$\frac{\partial \vec{M}}{\partial t} = -\gamma \vec{M} \times \vec{H}_{eff} + \alpha \vec{M} \times \frac{\partial \vec{M}}{\partial t} \quad (2.15)$$

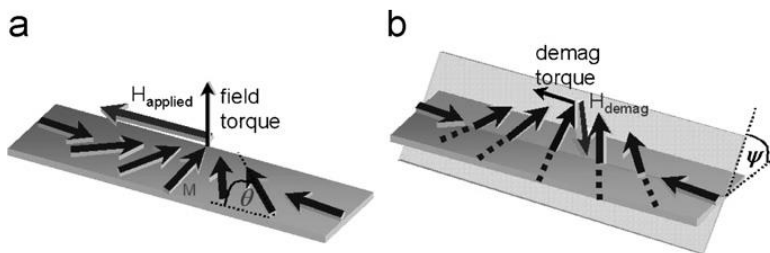


**Figure 2.8** The schematic of domain wall motion with an external magnetic field [36].

As shown in Figure 2.8(a), when an external magnetic field is applied across the Neel domain wall, magnetic moments experience a torque which is pointing out of the plane. This torque tilts the magnetization in the out-of-plane direction and hence produce a demagnetization field as shown in Figure 2.8(b). The interaction between the demagnetization field and the magnetic moments produces a torque along the external field direction which results in the domain wall motion along the external field direction [37].

Domains in a ferromagnetic material which are parallel to the external magnetic field tend to expand while antiparallel domains shrink due to the interaction between the field and magnetic moments. When the external field is larger than the  $M_s$ , the material becomes a single domain structure with all the magnetic moments aligned along the external field direction. If the external field strength decreases and slowly increases in the opposite direction, then the magnetic domains nucleate and expand along the reverse direction. The nucleation centers are usually the defects or impurities of the magnetic structure, and the nucleation process is a thermally activated process. When the reversed external field becomes larger than the saturation field ( $M_s$ ), a single domain can be observed along the reversed field direction. The hysteresis curve accompanied by the MOKE images demonstrates the different states of the magnetization switching process (Figure 2.9).

After the nucleation, the domain wall velocity responds to the magnetization switching over three main regimes [38], which are called the creep, depinning and flow regimes (Figure 2.10 [39]). At low magnetic fields (creep regime), the behavior of the domain wall motion is defined by the material disorders, defects, and the thermal energy. At zero temperature, domain walls are pinned to the impurities. Impurities are local energy minimum sites.

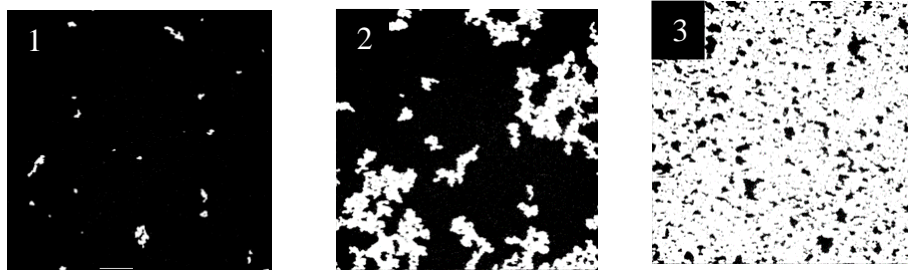
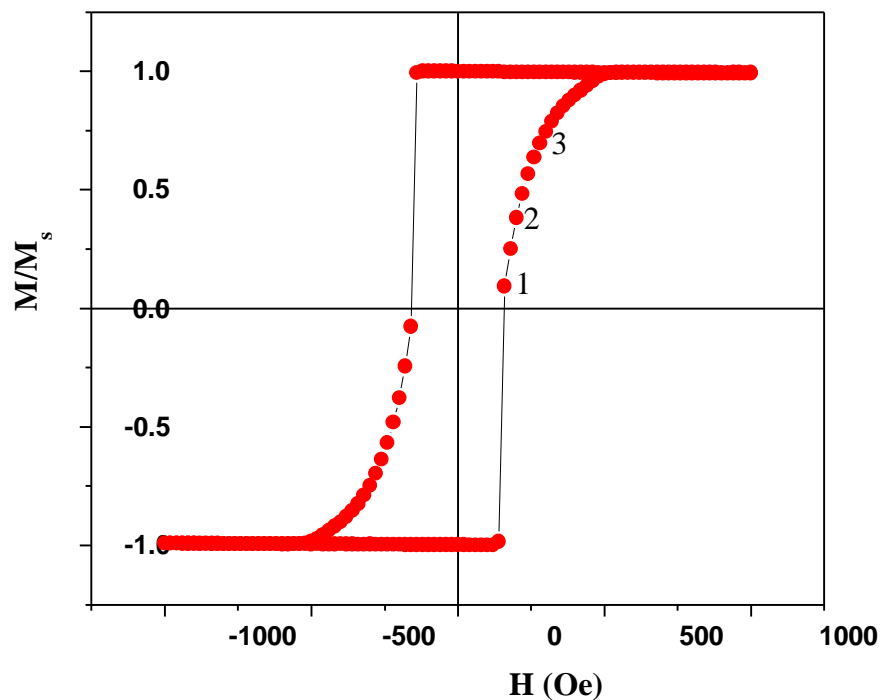


**Figure 2.9** Hysteresis measured on  $[\text{CoNi}]_6$  using MOKE microscopy. 1, 2, and 3 images show the domain nucleation and growth at the different external magnetic fields.

Therefore, domain walls prefer to stay pinned to impurities, and a low magnetic field which is below the depinning field is not sufficient to unpin the domain walls. However, at finite temperature, thermal energy overcomes the domain wall pinning, and slow domain wall motion can be observed with low magnetic fields [39-41]. When the magnetic field is greater than the

depinning field (in the flow regime), the domain wall motion is independent of the material disorder, and domain wall velocity increases linearly with increasing magnetic field.

In my experiments explained in chapters 4 and 5, the domain wall evolution is studied in the creep regime.

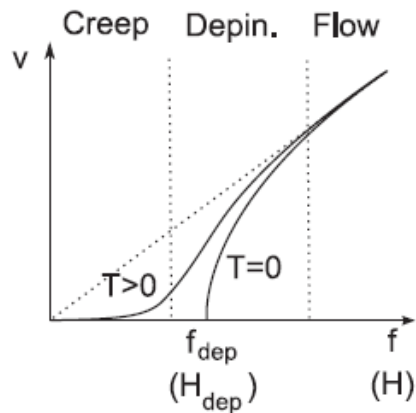


**Figure 2.10** The domain wall velocity as a function of external magnetic field, at three different regimes depending the strength of applied magnetic field [39].

## 2.8 Dzyaloshinskii –Moriya Interaction

Dzyaloshinskii Moriya interaction (DMI) is an asymmetric exchange interaction which was first predicted by Dzyaloshinskii [42] in 1958. Dzyaloshinskii proposed a phenomenological model to explain the weak ferromagnetic effect observed in antiferromagnetic crystals like  $\alpha$ - $\text{Fe}_2\text{O}_3$ . Later Moriya explained the antisymmetric exchange interaction theoretically with Spin-Orbit coupling in 1960 [43]. In 1980, A. Fert discovered large DMI between Mn spins in the presence of nonmagnetic impurities like Pt or Au [44]. In the presence of a heavy metal such as Pt, Ir, Ta, Ni, spin-orbit coupling between two neighboring ferromagnetic atomic spins ( $S_i$  and  $S_j$ ) with the heavy metal atoms causes interfacial DM interaction between the heavy metal and magnetic layer.

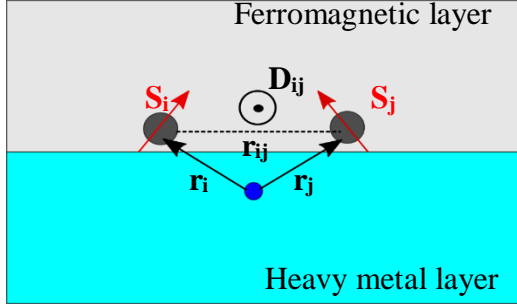


**Figure 2.11** The schematic representation of the Dzyaloshinskii-Moriya interaction in the Ferromagnetic(gray color)/ heavy metal (blue color) interface.  $S_i$  and  $S_j$  are the neighboring atomic spins in the ferromagnetic system which are coupled through a heavy metal atom due to the spin orbit interaction.

The interfacial DM field can be written as follows:

$$H_{DMI} = \vec{D}_{ij} \cdot (\vec{S}_i \times \vec{S}_j) \quad (2.16)$$

The DMI vector  $\vec{D}_{ij} = D(\vec{r}_{ij} \times \vec{z})$ ; where  $z$  is along the film normal.

The DMI energy is minimized if the angle between  $S_i$  and  $S_j$  is  $90^\circ$  and the cross product of the  $S_i$  and  $S_j$  is opposite to the direction of the  $\vec{D}_{ij}$ .

### 2.8.1 LLG Model of Domain Wall Motion in the presence of DMI

Domain wall motion equations derived from the LLG equation (Equation 2.15) in the presence of a DMI field, in-plane and out-of-plane magnetic fields, and PMA can be written as follows [45]:

$$\frac{\hbar}{\lambda}(1 + \alpha^2) \frac{\partial r_{DW}}{\partial t} = Qg\alpha H_z + \frac{\pi}{2} \left( \frac{H_{DMI}}{\lambda} - QgH_x \right) \sin\phi_0 \quad (2.17)$$

$$\hbar(1 + \alpha^2) \frac{\partial \phi_0}{\partial t} = -gH_z + \frac{\pi}{2} \alpha \left( Q \frac{H_{DMI}}{\lambda} - gH_x \right) \sin\phi_0 \quad (2.18)$$

where  $\alpha$  is the Gilbert damping constant,  $r_{DW}$  is the domain wall position,  $Q$  is the integration constant,  $\varnothing_0$  is the azimuthal domain wall angle,  $g$  is the Lande  $g$ -factor,  $H_z$  is the out-of-plane magnetic field,  $H_x$  is the in-plane field, and  $H_{DMI}$  is the DMI field.

Results of the numerical solutions of equation (2.17) and (2.18) in 2D systems show asymmetric domain wall expansion due to the DMI field and in-plane magnetic field (Figure 2.12).

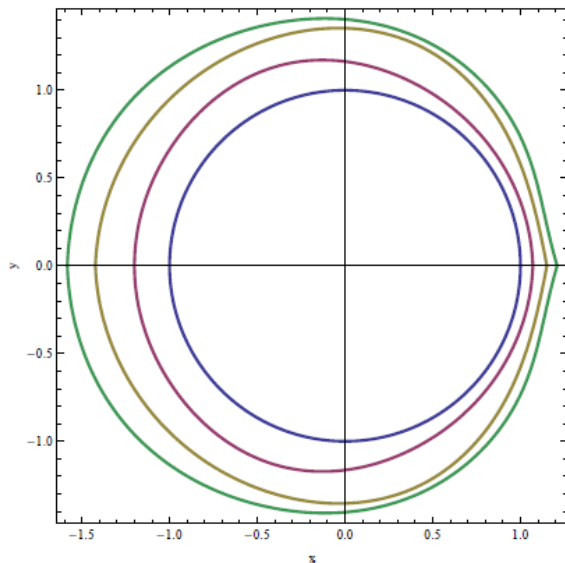


**Figure 2.12** LLG model of domain wall motion in the presence of DMI field, in-plane and out-of-plane magnetic fields in a ferromagnetic layer with PMA. The color lines indicate the position of the domain wall at different times [45].

### 2.8.2 Creep Theory of Domain Wall Motion in the presence of DMI

In-plane and DMI fields are included in the creep theory in terms of the energy density of the domain wall. Disorder of the material is not considered in the LLG model of domain wall motion. Therefore, creep theory is more appropriate than the LLG model to explain the experimental data. Creep theory is used in this thesis to investigate the DMI field in magnetic multilayers in the presence of in-plane and out-of-plane fields. A detailed description of creep theory with domain wall energy density can be found in Chapter 4.

## 2.9 Chiral Domain Walls and DMI

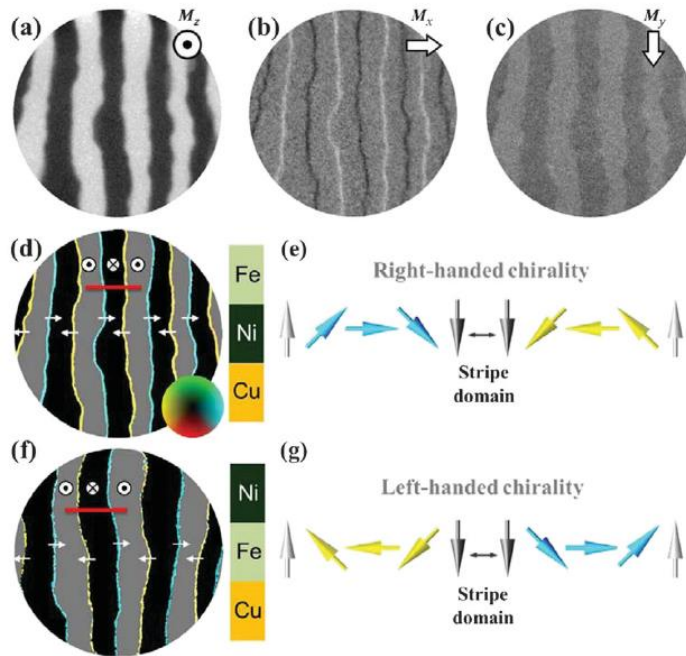


**Figure 2.13** The Spin Polarized Low Energy Electron Microscopic (SPLEEM) images of the Fe/Ni bilayers on Cu. (a), (b) and (c) indicates the magnetization components along Z, X, and Y directions respectively. (d) Compound SPLEEM image indicates right-handed, in-plane DW magnetization point from  $+M_z$  to  $-M_z$ . (e) magnetic moment configuration of the corresponding right-handed chiral DW structure. (f) reversing the bilayer growth order leads to left-handed chiral Neel walls observed. (g) left-handed chiral magnetic moment texture across the domain wall in (f) [48]

Bloch walls have lower magnetostatic energy than the Neel wall structure. Therefore, the lowest energy domain wall structure in the magnetic films with PMA is achiral Bloch walls. In the presence of DMI, the competition between DM energy and the exchange energy defines the minimum energy domain wall configuration. DMI leads to homochiral (right-handed chiral or left-handed chiral) Neel DWs throughout the structure, reported theoretically [46, 47] and experimentally (Figure 2.13) [48]. The sign of the DMI determines handedness of chirality. Right-handed chiral domains indicate positive DMI ( $D > 0$ ) and left-handed chirality represents negative

DMI ( $D < 0$ ). The chirality can be changed by altering the growth order of the ferromagnetic/heavy metal layers in the magnetic structure.

The effect of layer thicknesses on DMI has been studied. Chen et al. [48] reported that interfacial DMI gets weaker as the magnetic layer thickness increases above a threshold value by observing the transition of homochiral Neel walls to achiral Bloch walls (Figure 2.14). As the thickness increases, the spin-orbit interaction contribution on the magnetic structure decreases resulting in weaker DMI. Also as the thickness of the magnetic layer increases domain branching is observed due to a spin reorientation transition, but the domain wall chirality stays the same. This is an indication that the DMI is a short range local effect which does not depend on the distance between domain walls. Therefore, Heavy metal/ FM bulk structures have weaker DMI, and hence are not effective for the implementation in the domain wall based spintronic applications. Stacked multilayers can be used to overcome the thickness limitation for DMI based device applications.

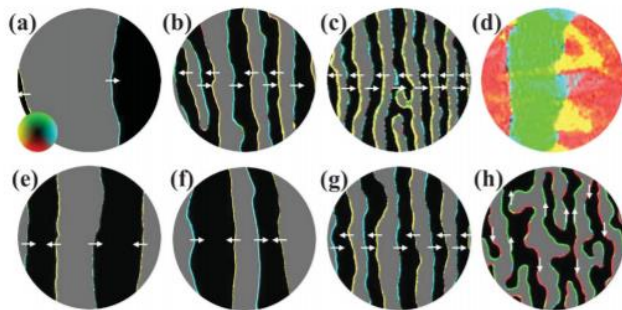


**Figure 2.14** The compound SPLEEM images of the Fe/Ni bilayers on Cu. Fe thickness increases while keeping Ni thickness fixed. (a), (b), (c), (d), (e), (f), (g), indicates domain width decreases as the Fe thickness is increased. Right-handed Neel DW configuration transform into Bloch walls at higher thickness. [48]

Chen et al.[49], demonstrated that contact of magnetic multilayers  $[\text{Co/Ni}]_n$  with Pt generates right-handed chiral Neel walls.  $[\text{Co/Ni}]_n$  grown on metallic Ir indicates the existence of

left-handed chiral Neel walls. Inserting different thicknesses of Ir in between  $[\text{Co/Ni}]_n$  magnetic multilayers and Pt layers can tune the domain wall chirality from right-handed Neel to left-handed Neel spin texture (Figure 2.15). At lower Ir thicknesses  $[\text{Co/Ni}]_n/\text{Ir}/\text{Pt}$  shows right-handed chiral DWs similar to the  $[\text{Co/Ni}]_n/\text{Pt}$ . The effect of thin Ir layer is not significant may be due to the fact that Pt surface is not fully covered with Ir or that the Pt electronic structure is hybridizing at the Ni/Co interface. At the higher Ir thicknesses, it overcomes the DMI effect from the Pt layer and shows the left-handed chiral spin texture similar to that of  $[\text{Co/Ni}]_n/\text{Ir}$ .

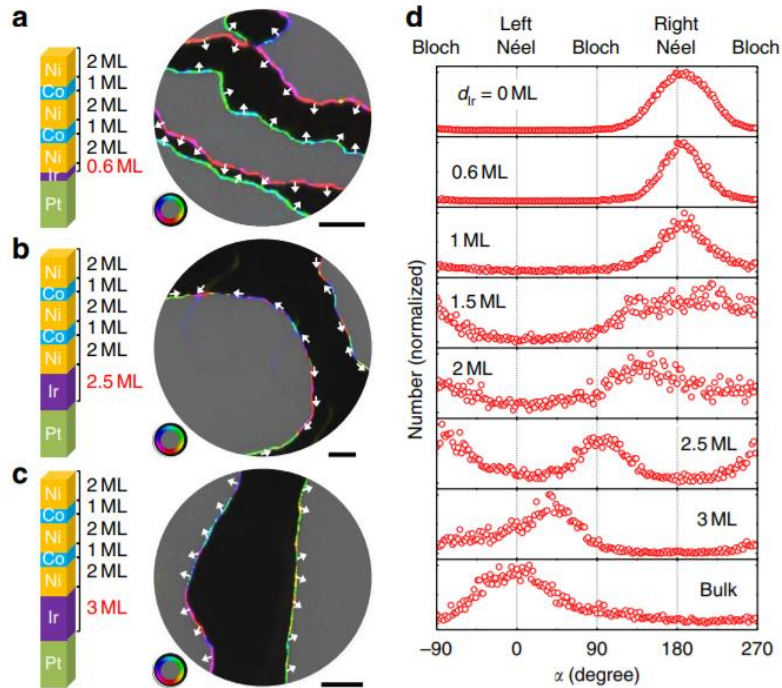


**Figure 2.15** The compound SPLEEM images of  $[\text{Co/Ni}]_n/\text{Pt}$ . (a) right-handed chiral Neel domain walls, (b) achiral Bloch domain walls, (c) left-handed chiral Neel domain walls, can be observed at different Ir thicknesses. (d) Ir thickness dependence on the angle  $\alpha$  ( $\alpha$  is the angle between the magnetization vector at the center of the DW and the normal vector of the DW) [49].

Studies on investigating DMI and the domain wall chirality can be found in many different types of ferromagnetic materials with PMA. Emory et al. [50] reported that the ultrathin ferromagnetic layer [CoFe] sandwiched between heavy metal and oxide exhibits chiral domain wall structures due to DMI. They experimentally observed left-handed chiral Neel DWs for Pt/CoFe/MgO and Ta/CoFe/MgO using the current driven domain wall dynamics. Torrejon et al. [51] reported that the sign and the DMI strength of X/CoFe/MgO could be changed by modifying the heavy metal underlayer X. Hf, Ta, TaN and W heavy metals were used as X. The current-driven domain wall motion technique was used to study the effect of the underlayer. They reported that Hf/CoFe/MgO has negative DMI corresponding to left-handed chiral DWs. Positive DMI was observed for TaN/CoFe/MgO and W/CoFe/MgO, indicating right-handed chiral DWs. They claimed that electronegativity of underlayer heavy metal material is the key parameter for the domain wall chirality change. Electronegativity increases from Hf to W in the periodic table; the DMI constant is also increased.

Pt is commonly used as the nonmagnetic heavy metal layer due to the high spin-orbit coupling which is essential for strong DMI. Co is often used as the ferromagnetic layer with the Pt heavy metal layer as Pt/Co exhibits a large PMA. Therefore, the Pt/Co system has obtained a great interest in DMI studies. Yang et al. [52] studied DMI behavior in Co/Pt bilayer films by varying the Co and Pt thicknesses from 1 to 3 monolayers (ML). Calculations based on first principals show that Co/Pt bilayers have positive DMI field which indicates left-handed chiral Neel DWs (Figure 2.16). The interfacial DMI effect weakens as the Co (magnetic layer) thickness increases. This result agrees with the weak DMI observation as the magnetic Fe layer thickness is increased [48].

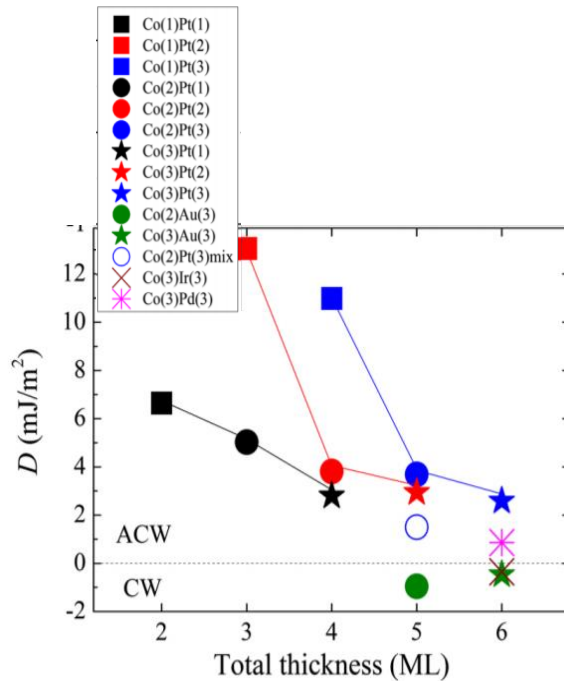


**Figure 2.16** DMI constant for the bilayers as a function of total thickness [52].

The field induced asymmetric bubble domain expansion method based on the creep theory to evaluate DMI and DW structure was proposed by Je et al. [53] in 2013 and Harbec et al. [54].

Experimental results of asymmetric bubble domain evolution in Pt/Co/Pt magnetic structures with DMI are shown in Figure 2.17 [53]. The Pt/Co interface and the Co/Pt interface have opposite DMI signs (due to the opposite growth order reported by Chen et al. [48]). To avoid cancellation of net DMI in Pt/Co/Pt, interfacial asymmetry is generated by the difference in the doping sequence of Co atoms into Pt layer and Pt atoms into Co layer. Je et al. reported that by analyzing the asymmetric domain wall motion in the presence of both in-plane and an out-of-plane fields DMI can be extracted in Pt/Co/Pt structure. The field induced domain wall motion was observed using MOKE microscopy. Symmetric DW expansion was observed with the out-of-plane field as shown in Figure 2.17 (a). Since the Pt/Co/Pt system has PMA, the applied out-of-plane magnetic field causes the DW motion to be isotropic. In the presence of both in-plane and out-of-

plane fields, asymmetric domain wall motion is observed (Figure 2.17 (b)). The two DWs (up/down and down/up) move in the opposite directions with different velocities parallel to the in-plane field  $H_x$ . It was explained that this asymmetry originates from the DMI field. Down/up and up/down domain walls have opposite DMI field direction. Therefore, parallel to the  $H_x$  axis, the two DWs experience two different effective fields ( $H_x + H_{DMI}$ ) and ( $H_x - H_{DMI}$ ). This results in DW motion with two different velocities. As indicated by the asymmetric domain growth along the X direction, the chirality of the Neel wall can be identified as right-handed, and the sign of DMI field is positive. The symmetry axis of the DW equi-speed contours shown in Figure 2.17 (c) indicates that the DMI field in Pt/Co/Pt is  $\mu_0 H_{DMI} \approx 26.5$  mT.

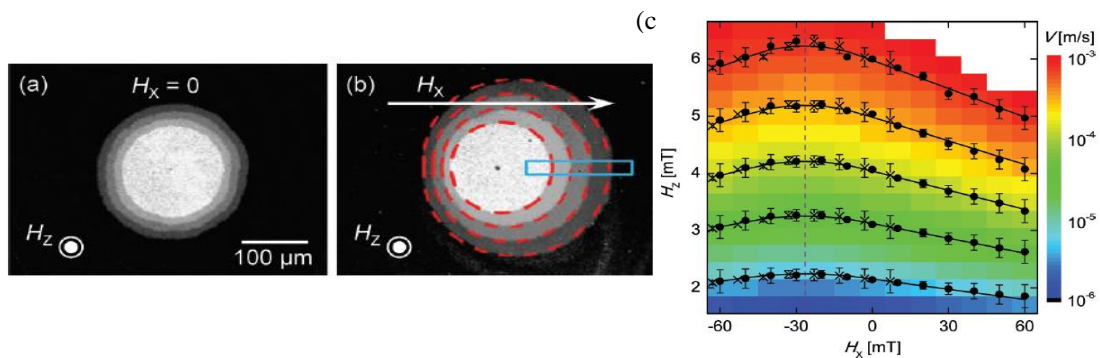


**Figure 2.17** (a) The MOKE image of symmetric bubble domain growth with out-of-plane magnetization. The magnetization inside the bubble domain is along the +Z direction. (b) The asymmetric bubble domain growth with both in-plane field ( $H_x$ ) and the out-of-plane field ( $H_z$ ). (c) The asymmetric velocity contour with the fields  $H_x$  and  $H_z$  [53].

Later, Hrabec et al. [54] reported that DMI in the Pt/Co/Pt ferromagnetic layer structure could be enhanced by introducing an Ir layer into the structure. As indicated previously, Pt/Ni and Ir/Ni interfaces have opposite DMI [49]. Therefore, Pt/Co, Co/Ir interfaces have the same sign of DMI and the effective DMI in the Co layer in Pt/Co/Ir/Pt structure is larger than that in the Pt/Co/Pt

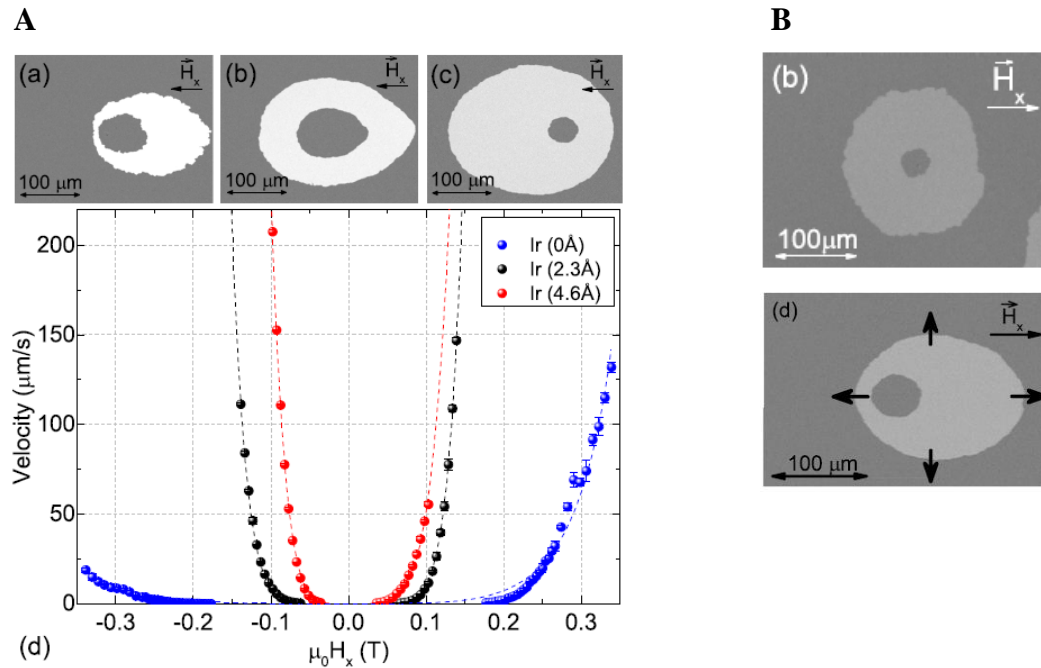


**Figure 2.18** (A) The differential MOKE images of DW motion of Pt/Co/Ir/Pt with in-plane and out-of-plane magnetic fields. (a) Structure with zero Ir (b) Ir thickness is 2.3 Å (c) Ir thickness is 4.6 Å. (d) The domain wall velocity as a function of in-plane field for different Ir thickness. (B) The bubble domain expansion for (b) epitaxial (d) for sputtered samples [54].

structure. They showed that the asymmetry of the domain wall motion could be changed by varying the thickness of the inserted Ir layer (Figure 2.18(a)). The sign of the DMI field and the chirality of the Neel domain wall changes with the Ir thickness. The extracted DMI field for the Pt/Co/Pt structure  $\mu_0 H_{\text{DMI}} \approx -100$  mT, which is opposite to the value reported by Je et al.[53]. The inserted Ir layer in Pt/Co/Pt structure enhances DMI field: Pt/Co/Ir/Pt  $\mu_0 H_{\text{DMI}} \approx 150$  mT. The thickness variation of the inserted Ir layer in Pt/Co/Ir/Pt tunes the chirality of the Neel domain wall from right-handed to left-handed. As Ir thickness increases, the DMI contribution from the Co/Ir interface overcomes the DMI effect from the bottom Pt/Co interface due to the higher spin-orbit coupling at the Co/Ir interface. However, it is reported that both Pt/Co and Co/Ir interfaces have the same signs of DMI. Therefore, the DMI sign change with increasing Ir layer thickness

contradicts the previous reports. It is claimed that the structural inversion symmetry can be obtained in the polycrystalline Pt/Co/Pt grown by sputtering technique due to the interfacial properties like roughness and degree of intermixing (Figure 2.18(b)). The epitaxial Pt/Co/Pt structures show symmetry in the bubble domain growth with the in-plane magnetic field due to the high level of crystallographic ordering (Figure 2.18(c)). Epitaxial structures have symmetric interfaces which cancel out the effective DMI field.

The effect of growth parameters on the DMI has been studied. Lavrijsen et al. reported asymmetric bubble domain expansion in Pt/Co/Pt films grown by sputtering technique at different the Ar pressure during the top Pt layer growth [55]. Asymmetric domain wall motion is explained using the domain wall energy profile along the in-plane field. Magnetic bubble domains in PMA materials favor achiral Bloch domain wall structure where the magnetization inside the DW rotates either clockwise or counterclockwise as indicated by double white arrows in Figure 2.19 (a). In the presence of the DMI field, DWs experience an intrinsic in-plane magnetization. Bloch DWs become Neel DWs when the intrinsic DMI field exceeds a critical value. If the DMI field is positive ( $D > 0$ ), right-handed chiral DWs can be observed as shown in Figure 2.19(b). Left-handed chiral DWs are observed for a negative DMI field ( $D < 0$ ). In the presence of a strong in-plane field  $H_x$ , Neel DW magnetization rotates along the external field direction. The Neel DWs in the top and bottom of bubble become Bloch DWs with the in-plane field. The Neel DW having the intrinsic DMI field against the  $H_x$  field (left of the bubble in Figure 2.19(c)) changes the chirality along the  $H_x$  direction, and gains a large DW energy density (Figure 2.19 (c), and (d)). The thickness of the arrows indicates the DW energy strength profile resulting from the in-plane ( $H_x$ ) field. The in-plane field creates the domain wall energy profile, and the out-of-plane field moves the DWs

asymmetrically according to the DW energy profile. Therefore, the asymmetric DW motion in the magnetic structures with PMA can be used as a direct measurement of DMI.

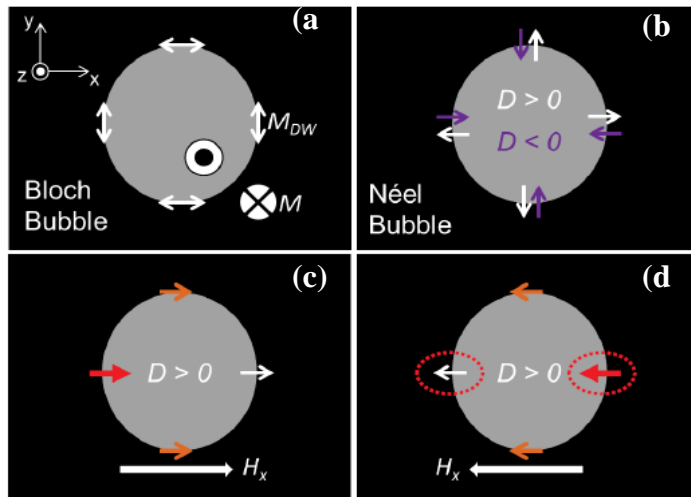


**Figure 2.19** Bubble DW motion with magnetic fields. (a) Bloch DWs have same energy density which expands the bubble domain symmetrically with the out-of-plane magnetic field. (b) positive DMI has Neel DWs pointing outward (white arrows), and negative DMI has Neel DWs pointing inward (purple arrow). (c) and (d) DW energy density profile for  $H_x$  in-plane magnetic field [55].

For all the Ar pressure variations the asymmetric DW velocity profile is observed with in-plane and out-of-plane fields and found to create a DMI field of  $\mu_0 H_{DMI} \approx 60 \pm 10$  mT (Figure 2.20). However, with the Ar pressure variation, a rapid change in PMA in Pt/Co/Pt tri-layer structures is observed. This is attributed to the interfacial quality of the Pt/Co/Pt structure, which causes asymmetric Co/Pt and Pt/Co interfaces. Therefore, extracting the same DMI value for different Ar pressure is contradictory to observing a structural property variation with the Ar pressure variation. Positive DMI indicates the existence of right-handed chiral DW structures in Pt/Co/Pt. The DMI sign and the domain wall chirality is similar to the results reported by Je et al. [53].

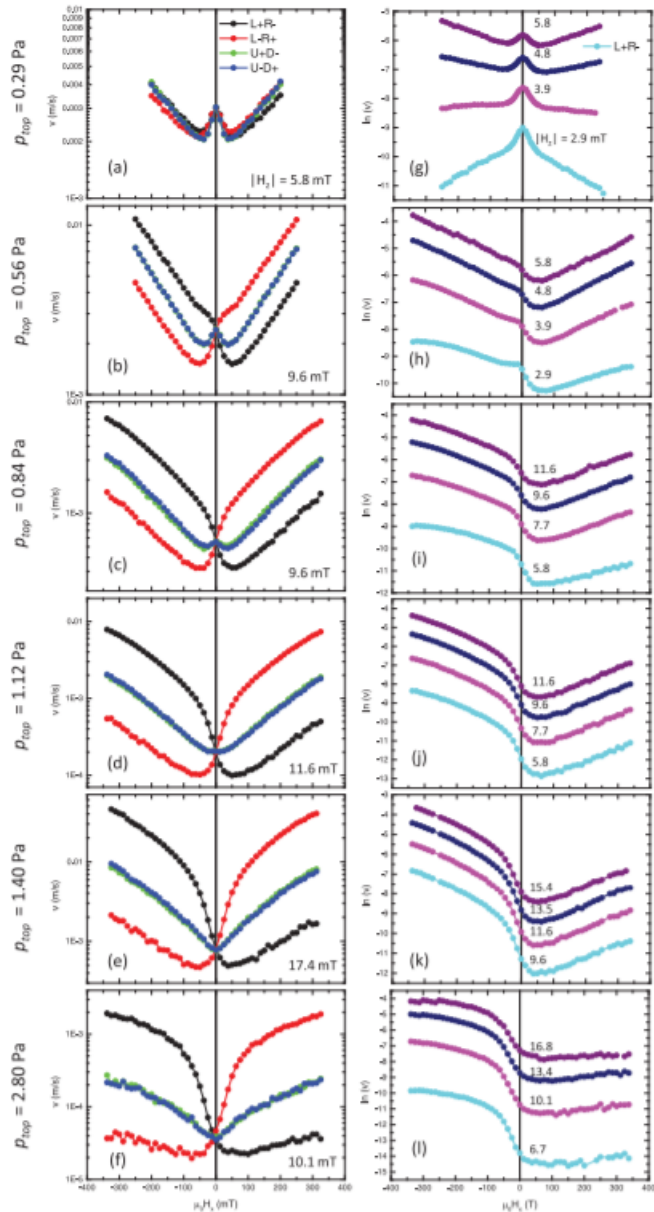


**Figure 2.20** (a) - (f) Domain Wall velocity as a function of in-plane magnetic field for different Ar pressure. Velocity variation increases as Ar pressure increases, but DW velocity asymmetry is the same. (g)-(l) DW velocity profile in logarithmic scale as a function of the in-plane field [55].

Wells et al. [56] studied the effect of the sputter deposition temperature ( $T_{dep}$ ) and the base pressure ( $P_{base}$ ) on the Co interface quality and DMI of Pt/Co/Pt thin films with PMA. The growth temperature of the top Pt and Co layers was varied from  $100$  °C to  $300$  °C while keeping the lower

Pt layer deposition temperature fixed at 550°C. Interface roughness decreases as  $T_{\text{dep}}$  increases were observed and may be due to the increase of mobility of atoms. Also the interface quality of the structure, which is the sum of the quadrature of roughness and the Pt/Co intermixing, increases with the increase of  $T_{\text{dep}}$ . The DMI field was calculated using the domain wall velocity obtained from the differential MOKE images. The DMI field increases from zero to  $400 \pm 100$  Oe as the interface quality of the top Co interface decreases relative to the bottom interface. If the interface quality of the bottom Co interface decreases relative to the top Co interface, the DMI field decreases from zero to around -100 Oe. The DMI field increases as deposition pressure increases (Figure 2.21). However, at higher base pressures, temperature does not affect the strength and the sign of the DMI field. Therefore, it is claimed that the upper and lower interface quality of Co can be changed by changing the deposition temperature. The interface quality asymmetry of Co layer introduces the structural inversion asymmetry which causes an effective DMI field in Pt/Co/Pt structures.

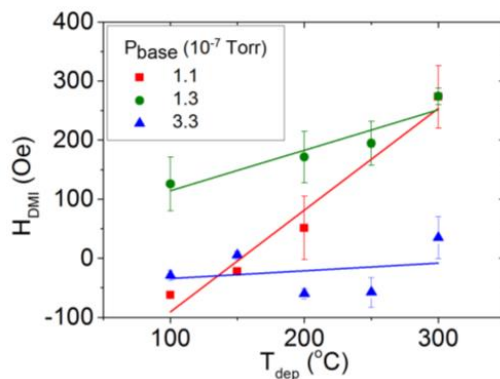


**Figure 2.21** The DMI field as a function of the deposition temperature for different base pressures [56].

Yu et al. reported DMI in dual interfaced CoNi multilayers with PMA [57]. The effect of two heavy metal/FM interfaces, which are bottom Pt/ Co-Ni, and top Co-Ni/X; X= Pt, MgO, Ta and Cu on DMI was studied using MOKE microscopy. Two heavy metal/ FM interfaces are used to generate high spin-orbit coupling interfaces with inversion symmetry which result in strong DMI. The observed asymmetric DW motion for all structures indicates the existence of DMI (Figure 2.22).

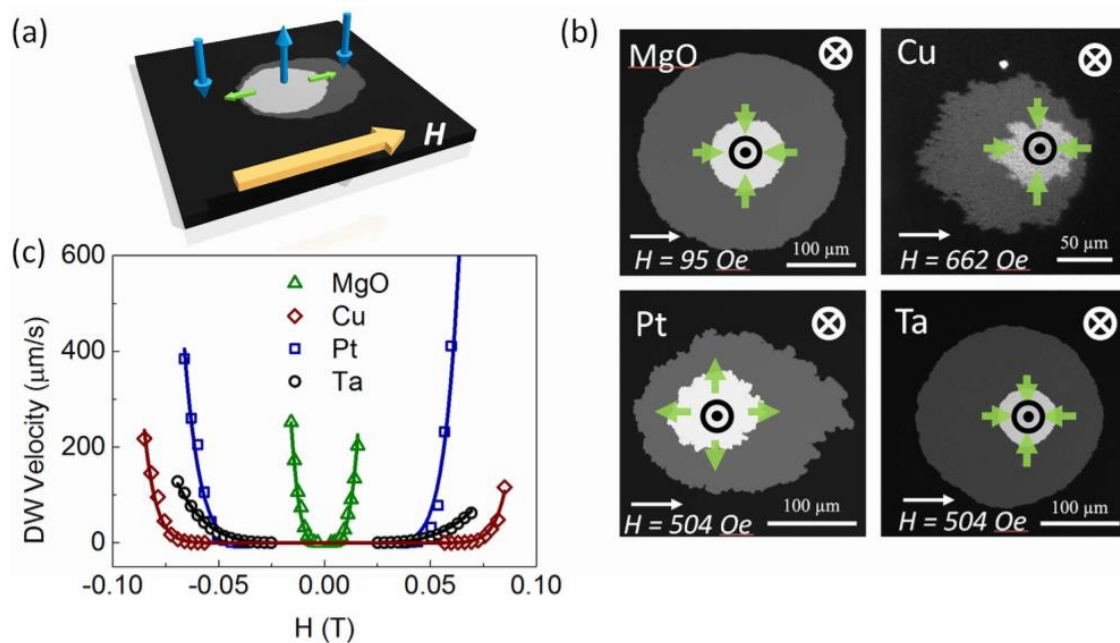


**Figure 2.22** The field driven DW motion observation for Pt/[CoNi]<sub>4</sub>/X multilayer structures, where X is MgO, Cu, Pt, and Ta. (a) The schematic of the magnetization directions of the structure. (b) MOKE images of asymmetric DW motion with in-plane and out of plane magnetic fields. (c) The dependency of DW motion on in-plane magnetic field [57]

Structures with a Pt capping layer show DW motion along the in-plane field direction indicating right-handed chiral Neel DW. Asymmetric domain growth against the in-plane field was observed for MgO, Ta and Cu capping layers. Domain growth against the in-plane field indicates the

existence of negative DMI and left-handed chiral Neel DW textures. The calculated DMI fields using the DW creep law for Pt/Co-Ni with MgO, Cu, Pt, and Ta capping layer structures are -155.9 Oe, -192.3 Oe, 348.8 Oe and -1038.6 Oe, respectively. Also, the DMI constant for the bottom Pt/Co-Ni interface was extracted from the structure with MgO capping layer as MgO has weak spin-orbit coupling. The DMI constant for the top Co-Ni/Pt interface was deduced from the total DMI constant of Pt/Co-Ni/Pt and the bottom Pt/Co-Ni interface DMI constant. Here the thickness of the bottom Pt is 4 nm, and that of top Pt is 2 nm. The DMI constant for top Co-Ni/Pt is 0.248 mJ/m<sup>2</sup>, and it is about 5 times larger than the DMI of bottom Pt/Co-Ni, which is -0.053 mJ/m<sup>2</sup>. This indicates that top Co-Ni/Pt interface governs the DMI in the Pt/FM/Pt structure even though the top Pt is thinner than the bottom Pt.

Contradictions have been found on the reported DMI field strength and sign of the heavy Metal/ FM magnetic structures for the same material systems. Different growth parameters and structural properties like layer thickness, interfacial roughness, and degree of intermixing might lead to the contradictions. Therefore, understanding the effect of growth parameters and structural properties on the heavy metal/FM interface is important while investigating new material combinations which enhance the DMI field.

The DMI effect from [Pt/Co/Ni]<sub>n</sub> multilayer structures have not been studied yet. In this thesis, our investigation on PtCoNi multilayer structures using the field-driven DW motion observed by polar MOKE microscopy is explained in Chapter 4.

## 3 EXPERIMENTAL METHODS

### 3.1 Introduction

Magnetic multilayer structure fabrication techniques and experimental methods used to characterize the magnetic structures are discussed in this chapter. Magneto-Optical Kerr magnetometry and microscopy were main characterization techniques used to measure magnetic properties of samples. In this chapter MOKE theory and the detailed measurement setup description are discussed. Depending on the required magnetic measurement several types of MOKE magnetometry, MOKE microscopy are described. The non-optical magnetometry technique (vibrating sample magnetometry (VSM)) used as a sample growth feedback is also discussed.

### 3.2 Samples and structures

Samples were grown at Emory University in the laboratory of Dr. S. Urazhdin. Pt/Co/Ni heterostructures with PMA are used to study Dzyaloshinskii-Moriya interaction (see Chapter 4 for the details) and a series of Co/Ni multilayers are investigated for magnetization reversal dynamics (Chapter 5) and stripe domain manipulation (Chapter 6). All samples were grown using a magnetron RF sputtering technique.

### 3.3 Magneto-Optical Kerr Effect (MOKE)

#### 3.3.1 MOKE Theory

The Magneto-Optical effect arises from the interaction of linearly polarized light with the optical anisotropy of the material that is associated with the magnetization of the domains. The optical anisotropy due to the magnetization asymmetry of the sample changes the polarization

direction of the incident light as it is reflected off the magnetic material. It was first reported by John Kerr in 1887 [58]. This technique is called as Kerr effect. Michael Faraday observed a similar effect, when light is transmitted through transparent magnetic material (Faraday Effect) [59] in 1845. Samples used in our work are thin metallic films with a mirror-like surface. Reflection of light is used to study their magnetic properties (Kerr effect). The Kerr effect can be expressed in terms of Kerr rotation and Kerr ellipticity which are described in the next section. Kerr rotation is proportional to the magnetization. Therefore, it can be used to investigate magnetic properties of materials.

The Kerr effect can be used to characterize the materials in the form of hysteresis loops or domain images. MOKE magnetometer results provide the characteristic data in the form of hysteresis loops. MOKE microscopy allows direct domain observation. This direct, simple, non-destructive observation technique can probe typically around 20 nm depth in metals [60].

The p-polarized wave has an electric field vector oscillating parallel to the plane of incidence. The electric field component perpendicular to the plane of incidence defines s-polarization. When this p- or s-polarized light is reflected off a nonmagnetic metallic surface which is an optically symmetric plane (plane with symmetric dielectric tensor), its linear polarization state stays unchanged. However, if the reflecting surface is made of a magnetic material the polarization of the reflected light rotates thus obtaining a small s-polarization (or p-polarization) component in addition to the initial p-polarization (s-polarization) component coming from the incident light. Since the newly added polarization component is out of phase with the original linear polarization component, the polarization axis of the reflected light rotates from the original axis and leads to an elliptical polarization state. This polarization change  $\Theta_k$  is measured in terms of Kerr rotation angle  $\theta_k$ : rotation of the polarization plane, and Kerr ellipticity  $\varepsilon_k$ .

$$\Theta_k = \theta_k + i\varepsilon_k \quad (3.1)$$

The physical origin of the MOKE can be explained by macroscopic dielectric theory using the antisymmetric off-diagonal elements of the dielectric tensor. A general overview of magneto-optical effect is given below. In the macroscopic theory, linearly polarized light is considered as the superposition of left- and right- circularly polarized electromagnetic waves. Optical properties of materials are determined by the motion of electrons and can be expressed through the elements of the  $3 \times 3$  dielectric tensor. Electromagnetic waves propagating through material generate motion of electrons by the electric field of the incident light wave. Left-circularly polarized light generates the motion of free electrons in a left-circular path while the right-circularly polarized light creates right circular motion of electrons. Unless there is an external magnetic field, radii of both left and right circular paths are the same. The material medium is isotropic, and the three eigenvalues of the dielectric tensor are the same. It follows that the dielectric tensor is reduced to the dielectric constant. The symmetric part of the dielectric tensor is related to the isotropy and can be represented by the diagonal terms of the dielectric tensor (see equation 3.2). With an external magnetic field in the system, the electrons experience a Lorentz force which drives electrons away or towards the center of the left or right circular motion. Since the radius of the electron path is different for the left and right circularly polarized light in the presence of an external magnetic field, the dielectric constants are also different accordingly. The antisymmetric part of the dielectric tensor related to the anisotropy is represented by the off-diagonal elements of the following dielectric tensor  $\tilde{\epsilon}$  [61-64];

$$\tilde{\epsilon} = \epsilon_{xx} \begin{pmatrix} 1 & -iQm_z & iQm_y \\ iQm_z & 1 & -iQm_x \\ -iQm_y & iQm_x & 1 \end{pmatrix} \quad (3.2)$$

The magneto-optical constant  $Q$  can be written as  $Q = i \frac{\epsilon_{xy}}{\epsilon_{xx}}$ .  $m_x, m_y$ , and  $m_z$  are the directional cosines of the magnetization which lays in an arbitrary direction.

Solving the Maxwell's equations for the magnetic medium with the dielectric tensor (3.2), the reflected light from the magnetized multilayer structure can be written in the following matrix form:

$$\begin{pmatrix} E_s^i \\ E_p^i \\ E_s^r \\ E_p^r \end{pmatrix} = \begin{pmatrix} E_s^i \\ E_p^i \\ r_{ss} E_s^i + r_{sp} E_p^i \\ r_{ps} E_s^i + r_{pp} E_p^i \end{pmatrix} \quad (3.3)$$

Here, subscripts s and p are indicating the s-polarization and p-polarization of the light. Superscripts i and r represents the incident and reflected electric field components. The Fresnel reflection coefficients can be written as:

$$S = \begin{pmatrix} \tilde{r}_{ss} & \tilde{r}_{sp} \\ \tilde{r}_{ps} & \tilde{r}_{pp} \end{pmatrix} = \begin{pmatrix} r_{ss} e^{i\delta_{ss}} & r_{sp} e^{i\delta_{sp}} \\ r_{ps} e^{i\delta_{ps}} & r_{pp} e^{i\delta_{pp}} \end{pmatrix} \quad (3.4)$$

where,  $r_{pp} = \frac{E_p^r}{E_p^i}$ ,  $r_{ps} = \frac{E_p^r}{E_s^i}$ ,  $r_{sp} = \frac{E_s^r}{E_p^i}$ ,  $r_{ss} = \frac{E_s^r}{E_s^i}$ , and  $\delta$  is the phase angle between s and p polarization components. The diagonal elements of the matrix represent the amplitude and the phase change of the same type of polarization as it reflects from the sample, while the off-diagonal elements reflect the conversion between the two types of polarization due to light interaction with magnetic material interaction.

$$\tilde{r}_{pp} = \frac{n_1 \cos \theta_0 - n_0 \cos \theta_1}{n_1 \cos \theta_0 + n_0 \cos \theta_1} - i \frac{2n_0 n_1 \cos \theta_0 \sin \theta_1 m_x Q}{n_1 \cos \theta_0 + n_0 \cos \theta_1} \quad (3.5)$$

$$\tilde{r}_{sp} = \frac{i n_0 n_1 \cos \theta_0 (m_y \sin \theta_1 + m_z \cos \theta_1)}{(n_1 \cos \theta_0 + n_0 \cos \theta_1)(n_0 \cos \theta_0 + n_1 \cos \theta_1) \cos \theta_1} \quad (3.6)$$

$$\tilde{r}_{ss} = \frac{n_0 \cos \theta_0 - n_1 \cos \theta_1}{n_0 \cos \theta_0 + n_1 \cos \theta_1} \quad (3.7)$$

$$\tilde{r}_{ps} = \frac{i n_0 n_1 \cos \theta_0 (m_y \sin \theta_1 - m_z \cos \theta_1)}{(n_1 \cos \theta_0 + n_0 \cos \theta_1)(n_0 \cos \theta_0 + n_1 \cos \theta_1) \cos \theta_1} \quad (3.8)$$

where,  $n_0$  and  $n_1$  are the refractive indices of the non-magnetic medium and the magnetic medium while  $\theta_0$  and  $\theta_1$  are the angle of incidence and the refractive angle in the magnetic medium, respectively.

The complex Kerr angle  $\Theta_K$  for the p- and s- polarized light can be expressed via Kerr rotation ( $\theta_K$ ) and the Kerr ellipticity ( $\varepsilon_K$ ) as follows,

$$\Theta_K^p = \theta_K^p + i\varepsilon_K^p \quad \text{and} \quad \Theta_K^s = \theta_K^s + i\varepsilon_K^s \quad (3.9)$$

where

$$\begin{aligned} \theta_K^p &= \frac{\tilde{r}_{sp}}{\tilde{r}_{pp}} & \varepsilon_K^p &= \frac{\tilde{r}_{sp}}{\tilde{r}_{pp}} \\ \theta_K^s &= \frac{\tilde{r}_{ps}}{\tilde{r}_{ss}} & \varepsilon_K^s &= \frac{\tilde{r}_{ps}}{\tilde{r}_{ss}} \end{aligned} \quad (3.10)$$

### 3.3.2 MOKE Geometries

MOKE can be observed in three different geometries (Figure 3.1). Depending on the plane of incidence of the light and the magnetization direction of the sample polar, longitudinal and transverse MOKE orientations are distinguished. Polar MOKE is sensitive to the out-of-plane magnetization component of the sample while the longitudinal and transverse MOKE configurations are sensitive to the in-plane magnetization component. In the polar Kerr geometry, the direction of magnetization is perpendicular to the sample and parallel to the plane of incidence. In the longitudinal Kerr geometry, sample magnetization direction lays in the plane of sample and parallel to the plane of incidence. Magnetization lays in the sample plane in the transverse Kerr geometry, but perpendicular to the plane of incidence. Polarization changes of the incident light as

it interacts with the magnetic sample can be explained using the Lorentz force. When the s- or p-polarized light is incident on the magnetized material, the electrons of the material oscillate parallel to the polarization direction and forms electric field component ( $E_0$ ). That produces a Lorentz force, hence an electric field component ( $E_k$ ) perpendicular to the magnetization direction and the direction of electron oscillation in the reflected beam. The resultant of  $E_p$  and  $E_k$  give rise to the

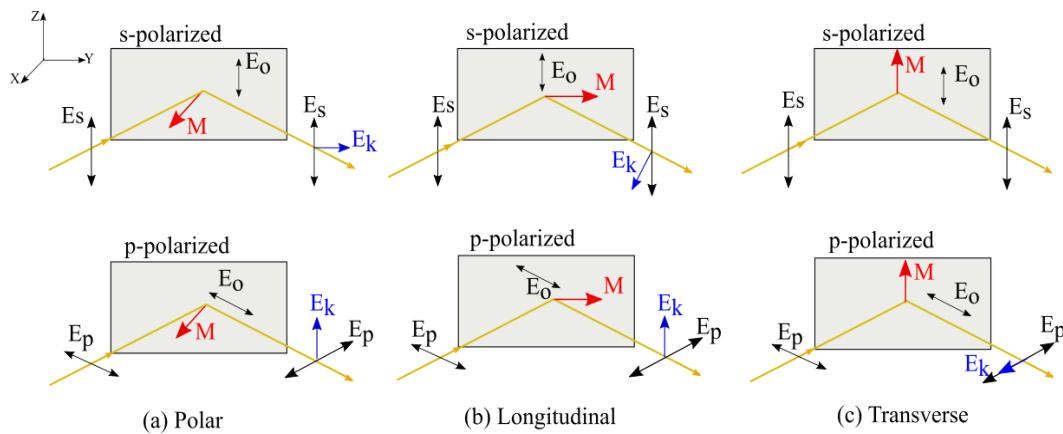


**Figure 3.1** The schematic representation of three different MOKE geometries. (a) Polar MOKE (b) Longitudinal MOKE and (c) Transverse MOKE configurations for both s and p-polarized incident light.

Kerr rotation. As shown in Figure 3.1, Kerr rotation can be observed in the polar and longitudinal geometries for both s and p-polarization. However, if the angle of incidence approaches zero in the longitudinal geometry with the p-polarized light, the Kerr rotation gets weaker as  $E_0$ , and  $M$  tends to align parallel to each other. Kerr rotation is not observable in the transverse configuration, but light intensity changes can be observed with the p-polarized light.

Samples described in this thesis are magnetized out-of-plane. Therefore, the polar MOKE configuration is used to characterize the magnetic properties of the samples using magnetometers and microscopy.

### 3.4 MOKE magnetometer with Phase Modulation

Since the Kerr rotation is proportional to the magnetization of the material, hysteresis curves can be obtained by measuring the Kerr angle as a function of the external magnetic field. A HeNe laser with 635 nm light wavelength and 10 mW output power was used as a light source (Figure 3.2). The electric field vector matrix for the laser light can be written in the form of

$$E = \begin{pmatrix} E_p \\ E_s \end{pmatrix}^i = \begin{pmatrix} 1 \\ 1 \end{pmatrix} \quad (3.11)$$

where,  $E_p$ ,  $E_s$  are the p-polarized, and s-polarized light components, respectively. The superscript  $i$  denotes incident light. The light is linearly polarized using Glan-Thompson polarizer with  $10^5:1$  extinction ratio and incident on the sample located at the center of the electromagnet pole gap. The Jones matrix for the polarizer (P) with the transmission angle  $\beta$  (the angle between the plane of incidence and the plane of polarization) can be written as :

$$P = \begin{bmatrix} \cos^2 \beta & \sin \beta \cos \beta \\ \sin \beta \cos \beta & \sin^2 \beta \end{bmatrix} \quad (3.12)$$

In our experiment the polarizer is set to  $\beta = 0$ ; therefore the matrix (3.12) can be simplified into,

$$P = \begin{bmatrix} 1 & 0 \\ 0 & 0 \end{bmatrix} \quad (3.13)$$

The reflected light from the sample is directed to the diode detector using a broadband non-polarizing cube beamsplitter. Another Glan-Thompson polarizer (commonly named as the analyzer) is used to cross polarize the original polarization component of the light. The analyzer

converts the polarization rotation into the light intensity variation. Its rotation was adjusted by a precise rotation stage to get the maximum Kerr sensitivity at the Si diode detector.

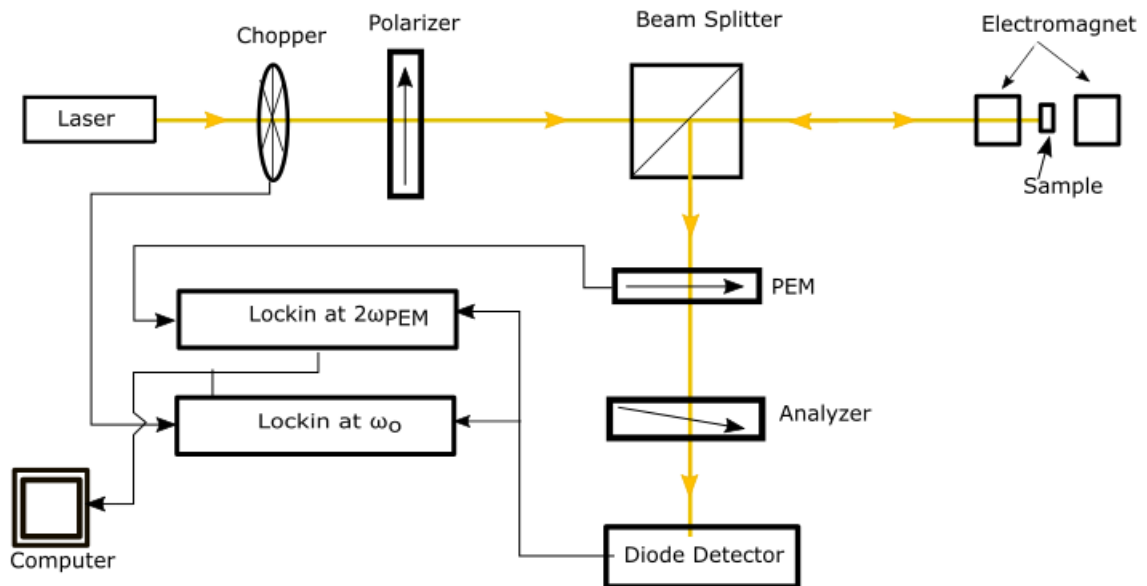


**Figure 3.2** The experimental set up of MOKE magnetometer with phase modulation.

“HINDS instruments” Photoelastic Modulator (PEM) was used between the beamsplitter and the analyzer to increase the sensitivity of the measurement. Due to the birefringence effect introduced by strain oscillations at  $\omega_{PEM} = 50 \text{ kHz}$ , the time-dependent refractive index difference permits the PEM to retard the phase of the one polarization component from the other perpendicular polarization component periodically. This phase modulation ( $\varphi$ ) can be expressed as follows in terms of phase modulation amplitude or retardance ( $\varphi_0$ ) and PEM resonant frequency  $\omega_{PEM}$  :

$$\varphi = \varphi_0 \sin(\omega_{PEM} t) \quad (3.14)$$

The general transfer function for PEM with modulator angle  $\theta_m$  can be represented by [65];

$$PEM = \begin{bmatrix} \cos\frac{\varphi}{2} - i \sin\frac{\varphi}{2} \cos(2\theta_m) & -i \sin\frac{\varphi}{2} \sin(2\theta_m) \\ -i \sin\frac{\varphi}{2} \sin(2\theta_m) & \cos\frac{\varphi}{2} + i \sin\frac{\varphi}{2} \cos(2\theta_m) \end{bmatrix} \quad (3.15)$$

Since the  $\theta_m = 0$ , the above expression can be reduced as follows:

$$PEM = \begin{bmatrix} e^{i\varphi/2} & 0 \\ 0 & e^{-i\varphi/2} \end{bmatrix} \quad (3.16)$$

When the retardance of the PEM is set to 0.5 wavelength and analyzer is tilted at  $45^\circ$  from the PEM axis, the diode gets the maximum light intensity. Therefore, the Jones matrix for the analyzer (A) from the equation (3.12) can be simplified as follows with  $\beta = \pi/4$ :

$$A = \begin{bmatrix} 1/2 & 1/2 \\ 1/2 & 1/2 \end{bmatrix} \quad (3.17)$$

The  $\cos(\varphi_0 \sin(\omega_{PEM}t))$  and  $\sin(\varphi_0 \sin(\omega_{PEM}t))$  terms of equation (3.16) can be written using the Fourier expansion and the Bessel functions:

$$\cos(\varphi_0 \sin(\omega_{PEM}t)) = J_0(\varphi_0) + 2 \sum_{m=1}^{\infty} J_{2m}(\varphi_0) \cos(2m\omega_{PEM}t) \quad (3.18)$$

$$\sin(\varphi_0 \sin(\omega_{PEM}t)) = 2 \sum_{m=0}^{\infty} J_{2m+1}(\varphi_0) \sin[(2m+1)\omega_{PEM}t] \quad (3.19)$$

The light intensity incident on the detector can be written as a product of above matrices (3.11, 3.13, 3.16 and 3.17) as it passes through the polarizer, dielectric sample, PEM and the analyzer:

$$\begin{aligned} E_{detector} &= A \cdot PEM \cdot S \cdot P \cdot E \\ &= \begin{bmatrix} 1/2 & 1/2 \\ 1/2 & 1/2 \end{bmatrix} \begin{bmatrix} e^{i\varphi/2} & 0 \\ 0 & e^{-i\varphi/2} \end{bmatrix} \begin{pmatrix} \tilde{r}_{pp} & \tilde{r}_{ps} \\ \tilde{r}_{sp} & \tilde{r}_{ss} \end{pmatrix} \begin{bmatrix} 1 & 0 \\ 0 & 0 \end{bmatrix} \begin{pmatrix} 1 \\ 1 \end{pmatrix} \end{aligned}$$

$$I \propto \frac{1}{2} (\tilde{r}_{pp} e^{i\varphi/2} + \tilde{r}_{sp} e^{-i\varphi/2}) \quad (3.20)$$

The equation (3.20) can be simplified using equations (3.4), (3.18), and (3.19) as follows:

$$I = \frac{1}{2} r_{pp}^2 \left[ \left( \frac{r_{sp}}{r_{pp}} \right)^2 + 1 + 2J_0(\varphi_0) + 4J_2(\varphi_0) \cos(2\omega_{PEM}t) + 4J_1(\varphi_0) \sin(\omega_{PEM}t) \right] \quad (3.21)$$

In the above equation, the even harmonics are related to the Kerr rotation, and the odd harmonics are related to the Kerr ellipticity. The intensities  $I_\omega$  and  $I_{2\omega}$  corresponding to the Kerr ellipticity and the Kerr rotation are measured by a lock-in technique at the fundamental PEM frequency (1<sup>st</sup> harmonic) and the 2<sup>nd</sup> harmonic:

$$I_\omega = 2r_{pp}^2 J_1(\varphi_0) \sin(\omega_{PEM}t) \quad (3.22)$$

$$I_{2\omega} = 2r_{pp}^2 J_2(\varphi_0) \cos(\omega t) \quad (3.23)$$

The Kerr rotation ( $\theta_K$ ) and the Kerr ellipticity ( $\varepsilon_K$ ) can be determined using following equations:

$$\theta_K = \frac{\sqrt{2}I_{2\omega}}{4J_2I_0} \quad (3.24)$$

$$\varepsilon_K = \frac{\sqrt{2}I_\omega}{4J_1I_0} \quad (3.25)$$

Here  $I_0$  is the intensity of the incident light, modulated by an optical chopper at frequency  $\omega_0$  and measured by the SR830 lock-in amplifier. The Kerr rotation corresponding to the magnetization of the sample can be obtained by dividing the Intensity of the 2<sup>nd</sup> harmonic of the MOKE signal measured by the Si detector with reference to the PEM frequency (50 kHz), from the intensity of the 1<sup>st</sup> harmonic signal frequency at the chopper frequency.

PMA samples are magnetized in the out-of-plane direction using the custom-built electromagnet which generates a maximum of 1000 Oe, and it is controlled by Agilent E3645A DC power supply. The magnetic field at the sample surface is measured using an axial Hall sensor HGA-2010. Lock-in voltages corresponding to the intensities are acquired by a LabVIEW program using GPIB interface.

### 3.5 MOKE magnetometer without phase modulation

The MOKE magnetometer utilizing phase modulation requires a Lock-In technique to detect the modulated signal. Typically, the integration time is from 300ms to 1s. The magnetic field should be kept stable during the measurements. Typical hysteresis loop sets contain about 100-1000 measured data points. For some experiments, it is critical to perform fast hysteresis measurements not allowing for magnetic field stabilization. We used the MOKE magnetometer without PEM, directly measuring light intensity by the detector with no polarization modulation. This technique is faster and allows measuring hysteresis curves as fast as 10ms per curve. The fast MOKE system (Figure 3.3) is used to study the effect of measurement time on the shape of hysteresis graphs, and those are compared with the hysteresis data obtained from the MOKE magnetometer with phase modulation.

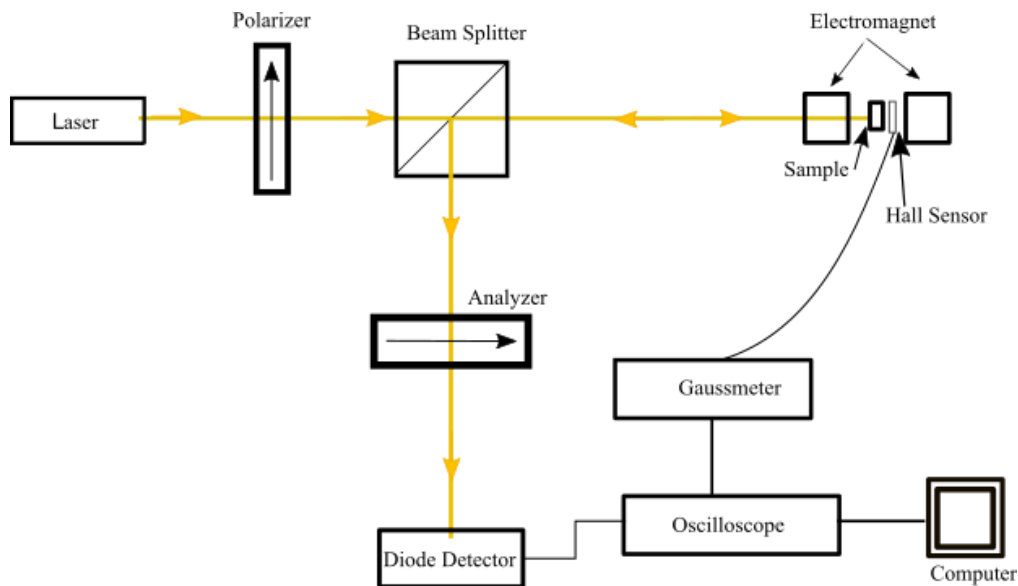


**Figure 3.3** The experimental set up of fast MOKE magnetometer without phase modulation.

In this case, an Agilent 33500B series waveform generator is used to drive the electromagnet by applying a triangular wave with a given amplitude and frequency. The advantage in this fast MOKE over the MOKE with PEM is that measurement time is very low.

Light from the HeNe, 10 mW laser source is passed through the Glan-Thompson polarizer. The linearly polarized light is then reflected from the magnetized sample and aligned to the Si detector using a broadband non-polarizing cube beam splitter. Another Glan-Thompson polarizer (analyzer) is cross-polarized with the first polarizer, so that the polarization rotation corresponding to the sample magnetization is converted to the light intensity at the detector. A Hall sensor placed right next to the sample was used to measure the magnetic field, and the Agilent Digital Storage oscilloscope DSO-X 2024A was used to read the signal from the diode detector and Hall sensor. The magnetization corresponding to the Kerr rotation was plotted as a function of the magnetic field in Origin software to obtain the hysteresis graph.

### **3.6 MOKE Microscopy**

The Magneto-Optical Kerr effect was used to observe the domain structures of magnetic materials. We use the polar MOKE configuration (Figure 3.4) to study the domain manipulation, demagnetization effects and domain motion associated with the DMI interaction. However, since the domain observation related to the Kerr rotation is a weak effect, a high-intensity Mercury arc light source is used to illuminate the sample. Light from the arc lamp to the optical table is transmitted through a Multimode optical fiber. Then the light is focused to the rear aperture of the objective lens using a convex lens (88.9 mm focal length). A Glan-Thompson polarizer polarizes the incident light either into the p-polarized light or into s-polarized light. The reflected light from

the magnetic sample is aligned to a convex lens ( $f = 750 \text{ nm}$ ) using a Broadband Dielectric beam splitter. The slight wedge shape of the beam splitter reduces the unwanted interference effects.

Then the light is focused on the Point Grey Research Grass Grasshopper 3 camera using the convex lens. The analyzer is cross-polarized with the polarizer to convert the polarization change introduced by the magnetic sample to light intensity. The Kerr rotation corresponding to the domain information is obtained at the detector. An intensity stabilizer is used to stabilize the intensity of the Hg lamp light incident on the sample. A beam sampler located between the convex lens and the polarizer reflects part of the light to the detector to stabilize the light intensity.

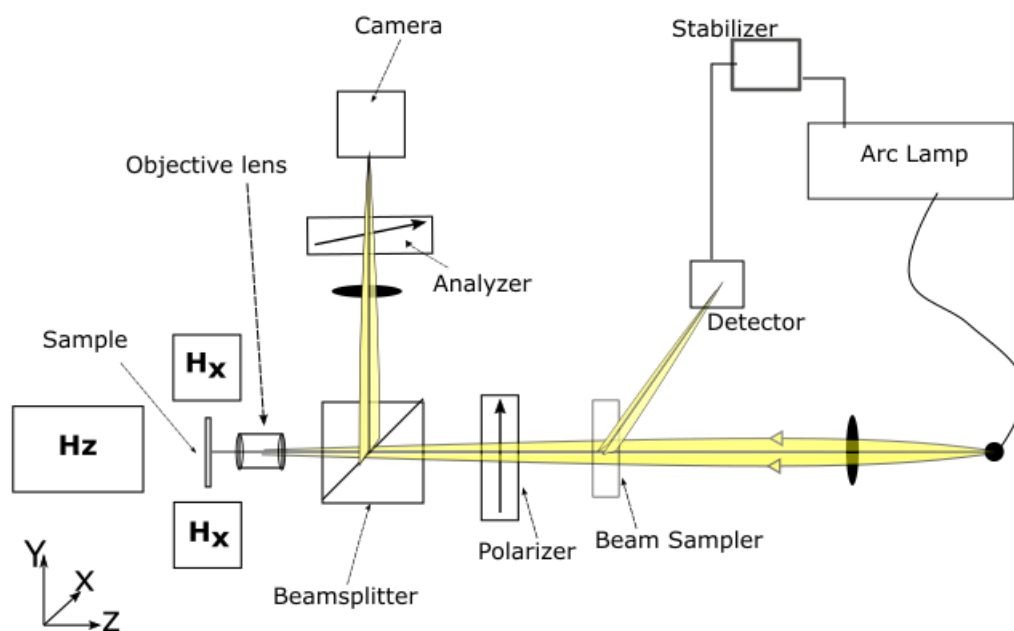


**Figure 3.4** The experimental set up of MOKE microscope.

A GMW 3740 electromagnet is used to generate the in-plane field. It is controlled by a Kepco bipolar operational power supply. A water cooling system is implemented to prevent the electromagnet from over-heating at high magnetic fields. A home-built 0.1 T electromagnet

controlled by the Kepco bipolar power supply is used to generate the out-of-plane magnetic field ( $H_z$ ). The sample is mounted vertically on a  $360^\circ$  rotatable sample holder.

Direct domain observation on the sample is not possible as the Kerr rotation due to domains is very weak. Therefore, several image processing techniques were implemented with the use of the LabVIEW program. The sample is saturated, and the image is saved as the reference.

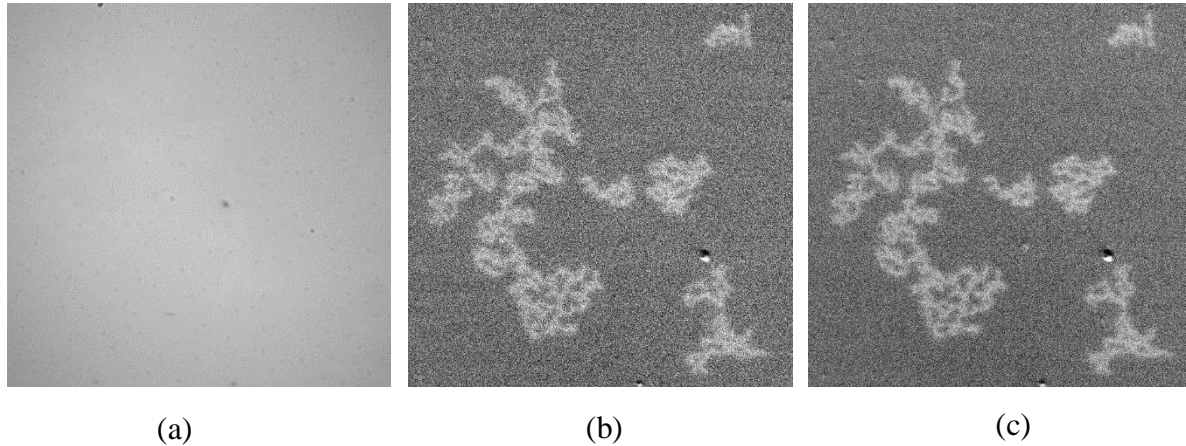


**Figure 3.5** The MOKE microscopy domain images of CoNi heterostructure. **(a)** Direct domain image from the camera before image processing. **(b)** The same domain image after subtraction the saturated reference image. (Differential MOKE image). **(c)** The image after averaging 200 Differential MOKE images.

Then the reference image is subtracted from all the images which contain magnetic data. The resultant image has high contrast magnetic information by removing the background data. Also, 200 snapshots of the differential image are averaged to optimize the contrast of the domain structure. The images before and after the image processing are shown in Figure 3.5.

The FEMM and CAD designs of the designed electromagnet which was used in the experiments can be found in the Appendix.

### 3.7 Vibrating Sample Magnetometer (VSM)

VSM is a technique used to provide a fast feedback to measure the hysteresis curves of the samples. A schematic of the VSM is shown in Figure 3.6. The sample is aligned in the electromagnet plane to the center between the two magnet poles.

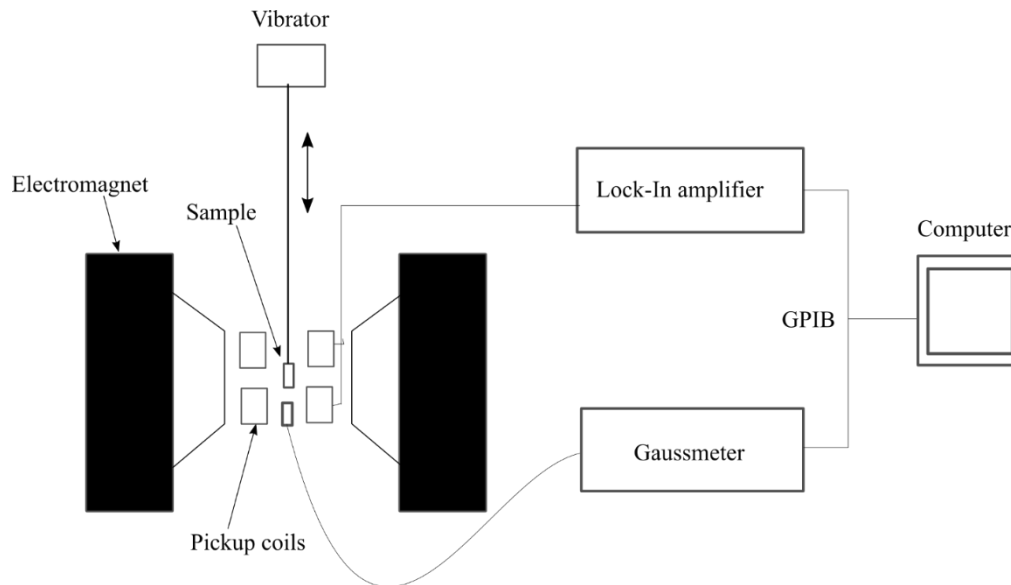


**Figure 3.6** The experimental set up Vibrating Sample Magnetometer.

The electromagnet controlled by a bipolar power supply sweeps the magnetic field on the aligned sample. The vibrator oscillates the sample in the vertical direction with a given frequency and amplitude. Vertical movement of the sample changes the magnetic flux and generates an electromotive force on the pickup coils mounted on the magnet poles. The generated electromotive force is proportional to the magnetization of the sample. This induced voltage associated with the magnetization of the sample is detected by a Lock-In amplifier. Magnetization is measured as a function of the magnetic field. The collected data are recorded by the LabVIEW program.

## 4 DMI IN PT/CO/NI HETEROSTRUCTURES

### 4.1 Introduction

Magnetic domain wall logic is an architecture which uses magnetization of DWs instead of the electron charge transistors used in conventional semiconductor logic devices. Heat loss is one of the main energy efficiency limiting factors in conventional semiconductor based logic devices. Domain wall logic devices exhibit negligibly low heating that happens only at a magnetization switching phase. It is observed that the domain walls can propagate when an external magnetic field is applied. The two binary states (logical “0” and “1”) are represented by magnetization orientation within the ferromagnetic domains. The domain wall propagation driven by the applied magnetic field results in switching between the logic states. Manipulating domains in ferromagnetic films patterned into complex geometries with junctions and magnetic “wire” shape variations allows us to perform various logic operations. The NOT gate, AND gate, fan-out junction, cross-over junction which are necessary for magnetic logic circuits are demonstrated by driving the domain wall in nanowires[10, 66, 67]. Therefore, investigating domain wall manipulation with an external magnetic field is important for future domain wall logic applications.

The magnetic materials with PMA have great potential in high-density information storage applications as higher bit densities with large thermal stability may be achieved. Formation of achiral Bloch domain walls is favored during magnetization reversal in PMA materials. Magnetic/non-magnetic heavy metal systems like Pt/Co exhibit PMA. However, due to strong spin-orbit coupling in these materials, the anti-symmetric exchange interaction at the inter-layer interface (DMI) results in Neel rather than Bloch domain wall formation [43, 46, 68]. DMI is responsible for the atomic scale topologically protected chiral magnetic textures such as skyrmions

[69]. Skyrmions have typical dimensions of 2-10nm which is about one order of magnitude smaller than the stable domain size in ferromagnetic materials with PMA. This opens possibilities of significantly increasing information storage density and novel logic device applications [70-73].

Interfacial DMI material systems with opposite growth order exhibit the opposite sign of DMI [74, 75]. Therefore, to obtain a non-vanishing DMI effect, it is essential to form an asymmetric layer structure. At the same time, it was reported that even with symmetric layer structures like Pt/Co/Pt, DMI exists, because the two interfaces are not symmetric in terms of different growth sequence, roughness, the degree of layer intermixing during growth as well as different growth parameters [76-78]. The DMI in symmetric layered structures does not provide good control over the DMI as too many growth-dependent parameters are involved. In this thesis, PMA films with broken inversion symmetry are formed by introducing a different magnetic layer for one of the interfaces [54].

Interfacial DMI leads to the asymmetric domain wall motion by breaking the rotational symmetry with an application of in-plane magnetic field [53, 54, 77, 79, 80]. Current-driven domain wall motion in the DMI systems has been studied. A lithographic technique is needed to drive the current in the sample. Therefore, current driven domain wall motion implementation in spintronic devices is critical. Also, the complexity of the interpretation arises from the interplay of effects like Rashba and spin Hall effect [81-85]. The direct magnetic field-driven domain wall motion is used in this work to study the DMI in magnetic structures with broken inversion symmetry and PMA.

The interfacial DMI observed in thin layer structures decreases with the increase of the magnetic layer thickness. That limits the DMI based device application. Multilayer structures with inversion asymmetry can be used to increase the thickness of the sample without decreasing DMI.

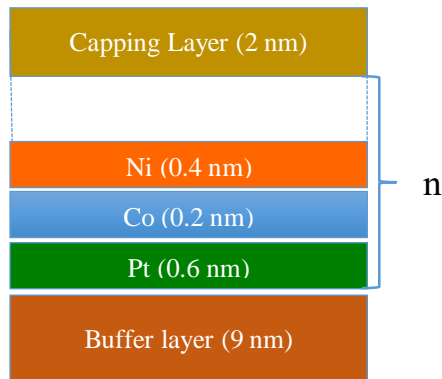
Multilayer structures overcome the thickness limitation by sustaining the interfacial DMI in bulk systems.

In this chapter, interfacial DMI in Co/Ni/Pt systems with broken inversion symmetry is studied. MOKE is used to measure domain wall velocities to extract the DMI values. An analysis is presented of the effective DMI field in heterostructures with PMA and inversion symmetry for varying numbers of PtCoNi tri-layers.

## 4.2 Sample description

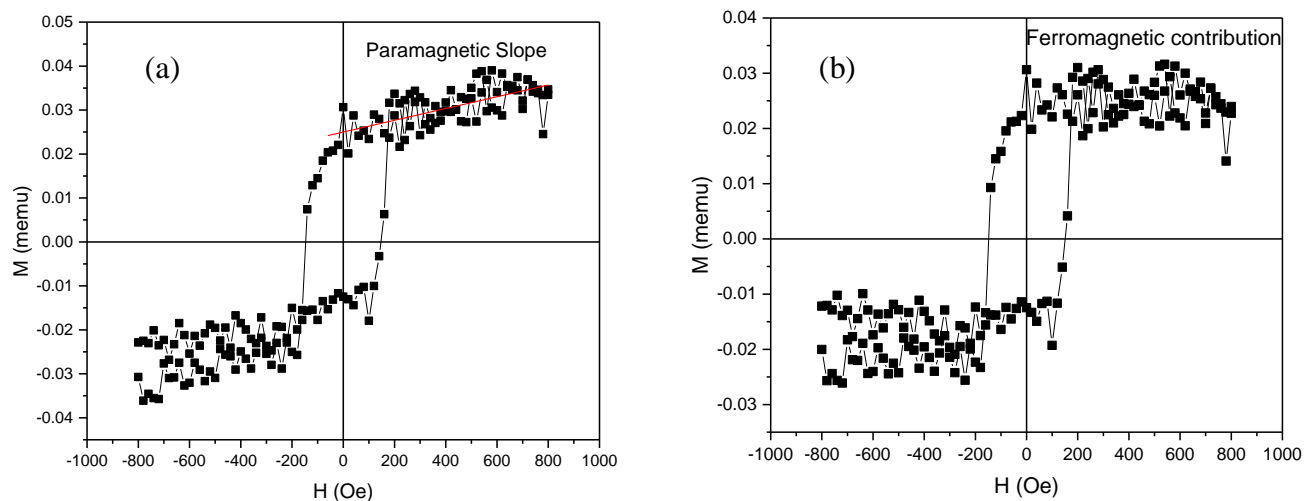
Magnetic multilayer structures of  $Ta(4)Cu(5)\{[Pt(0.6)Co(0.2)Ni(0.4)]_n\}Ta(2)$  were grown using DC magnetron sputtering technique as mentioned in Chapter 3 (Figure 4.1). (The numbers within brackets indicate the thickness of the layer in nm.) A Ta/Cu buffer layer is grown on a Si substrate to minimize the lattice mismatch, and then Pt, Co and Ni layers are deposited as indicated in Figure 4.1. Pt/Co and Co/Pt interfaces have opposite signs of DMI, which results in low effective DMI in the Pt/Co/Pt structure. Therefore, Ni is introduced to the system to break the inversion symmetry of Pt/Co/Pt to obtain a strong DMI. A Ta capping layer is used to prevent the structure from oxidization. The MOKE setup measures about 20 nm deep into the material surface in most metals. Therefore, a 2 nm thick Ta capping layer does not affect the measurement of underlying magnetic material. Light transparent materials like SiO<sub>2</sub> and Si<sub>3</sub>N<sub>2</sub> also could be used as the capping layers. But their deposition utilizes oxygen or nitrogen gasses which may lead to oxidization or nitrogen introduction to the film that can significantly alter the magnetic properties of the ferromagnetic layers. The number of PtCoNi tri-layers ( $n$ ) was varied in the range of  $n = 1$  to 10 to investigate the DMI effect in bulk structures. The evolution of the DMI was studied as a

function of the tri-layer repetition number. The Co thickness was chosen to be around 0.2 nm, to involve all the atoms of the Co layer for the interfacial DMI.



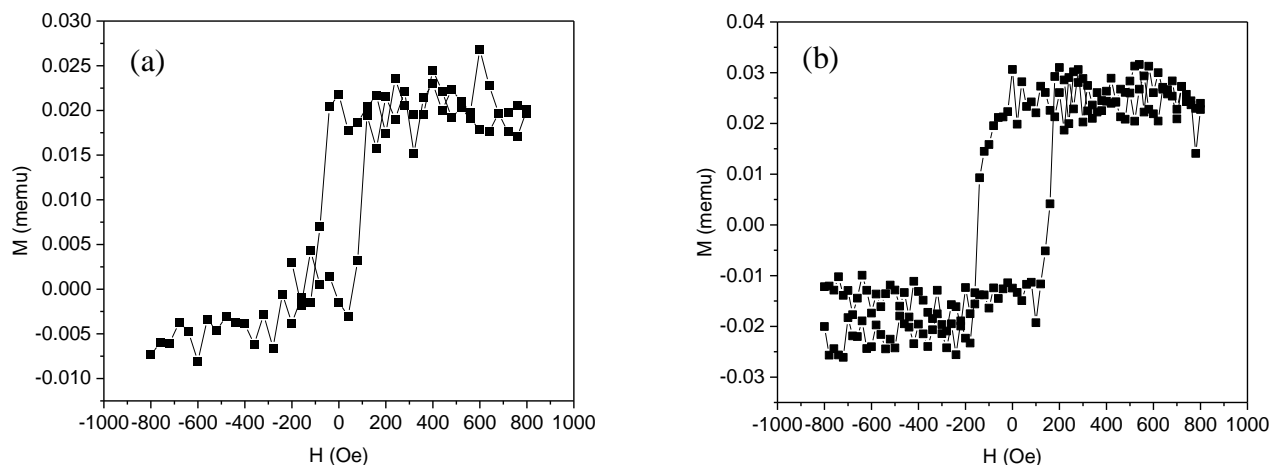
**Figure 4.1** The sketch of the ferromagnetic structure of Pt/Co/Ni tri-layer repetition.  $n$  is the number of Pt/Co/Ni tri layer repetitions. The numbers in the brackets indicate the layer thickness in nm.

The out-of-plane VSM hysteresis curves measured on PtCoNi tri-layers are shown in Figure 4.2. Hysteresis curves demonstrate an abrupt switching with the out-of-plane magnetic field (square shape) which indicates the existence of PMA on the growth samples. The positive slope in the curves originates from the paramagnetic effect of the Si substrate and the sample holder [86], and the hysteresis curve does not saturate but rather exhibits a non-zero positive slope at high magnetic fields. This slope was used to calculate the paramagnetic contribution for each measured hysteresis curve. Subtracting the paramagnetic contribution exposed the pure ferromagnetic contribution of the PtCoNi tri-layer heterostructures (Figure 4.3).



**Figure 4.2** The out-of-plane hysteresis graphs of  $[Pt/Co/Ni]_n$  heterostructures obtained from Vibrating Sample Magnetometer. (a) the hysteresis loop before the correction (b) the hysteresis loop after the correction.

After subtracting the paramagnetic contribution, the hysteresis loops corresponding to the ferromagnetic multilayer structures of Pt/Co/Ni tri-layer repetitions are shown in Figure 4.3 for different level repetitions.



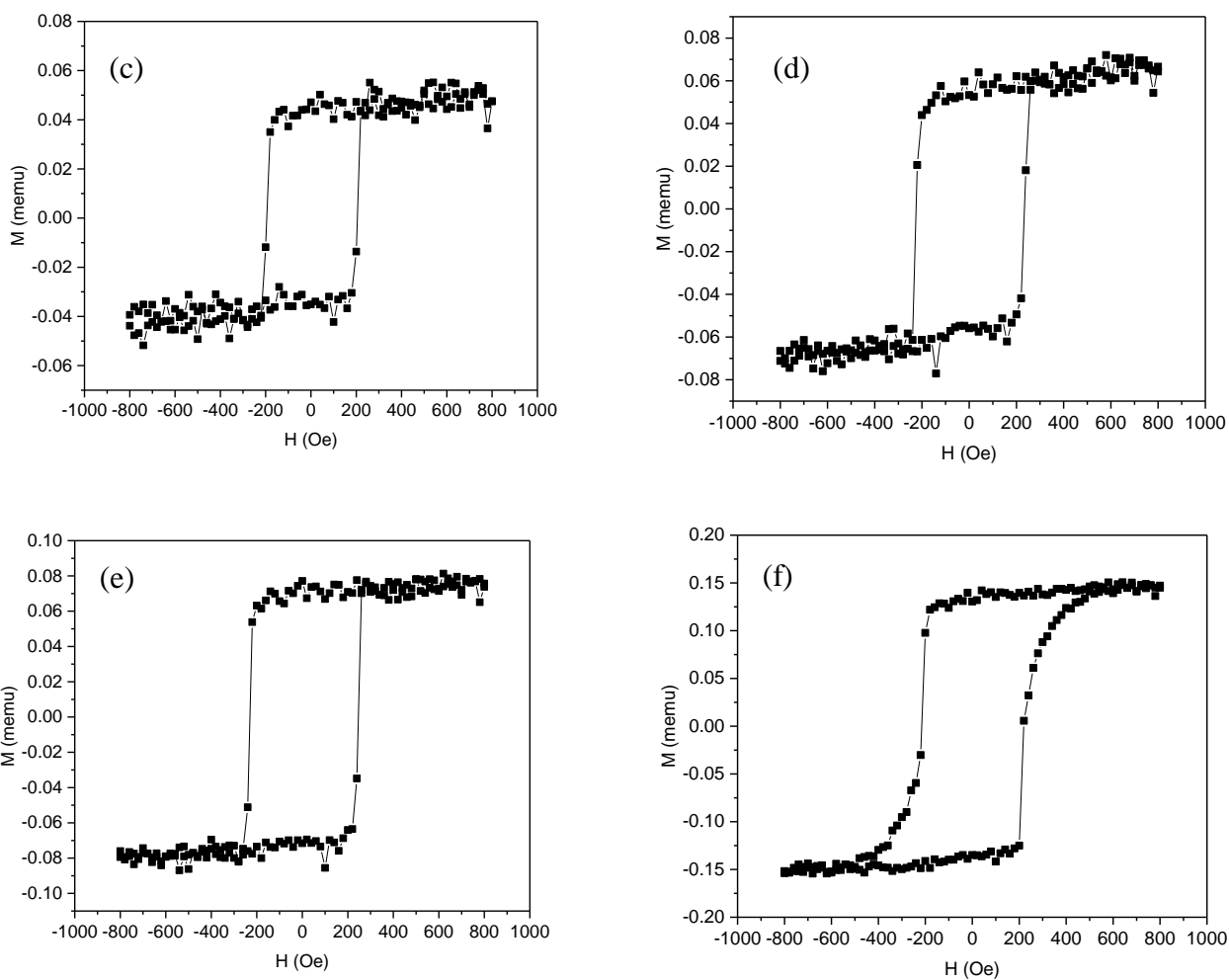


**Figure 4.3** The modified hysteresis loops (after subtracting the paramagnetic effect from the substrate) of  $[\text{Pt}/\text{Co}/\text{Ni}]_n$  heterostructures obtained from VSM. (a), (b), (c), (d), (e), and (f) indicates the hysteresis loops corresponding to the 1, 2, 3, 4, 5, and 10 tri-layer repetitions respectively.

**Table 4-1** The coercive fields of  $[\text{PtCoNi}]_n$  extracted from the hysteresis loops.

PtCoNi structure	Coercive field, $H_c$ (Oe)	$M_s$ (A/m) $\times 10^5$
$[\text{PtCoNi}]_1$	36	5.77
$[\text{PtCoNi}]_2$	101	4.71
$[\text{PtCoNi}]_3$	187	4.72
$[\text{PtCoNi}]_4$	200	4.58
$[\text{PtCoNi}]_5$	195	4.57
$[\text{PtCoNi}]_{10}$	195	3.89

### 4.3 MOKE measurements and Domain wall motion

The field-induced domain wall evolution of  $[\text{Pt}/\text{Co}/\text{Ni}]_n$  heterostructures was investigated using MOKE microscopy. See Chapter 3 for a detailed measurement setup description. The samples were first saturated in the (-z) direction (Figure 4.4). Once the samples are saturated, a reverse field slightly larger than the coercive field (Table 4.1) of the sample is applied in the form of the field pulses in the +z direction to nucleate the magnetic domains.

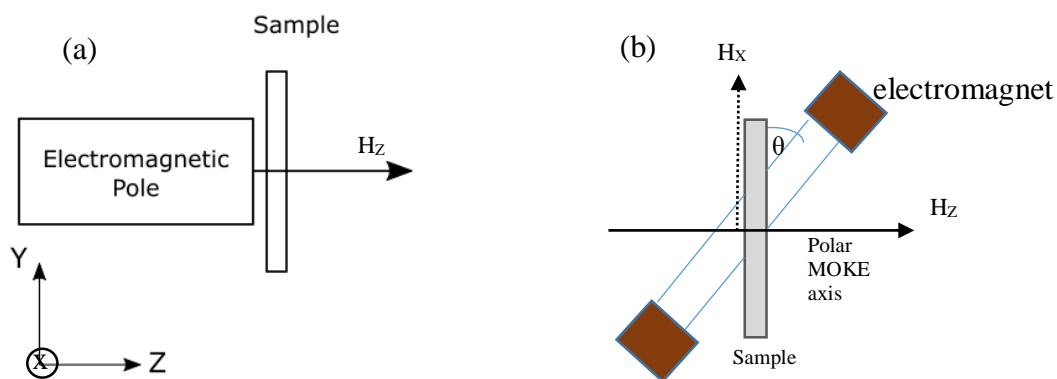


**Figure 4.4** Schematic of sample and electromagnet alignment used in polar MOKE measurements. (a) MOKE geometry for the out-of-plane field measurements. (b) MOKE geometry for the combination of out-of-plan and in-plane magnetic field pulse application.

Thermally activated nucleation centers grew into bubble domains with the reverse field. Smooth domain wall boundaries for the 1 and 2 repetitions of tri-layers and rough domain wall boundaries for the higher order of repetitions were observed (Figure 4.7). As can be seen in Figure 4.5, the nucleated bubble domains expand symmetrically with the reverse field. The bubble domain expands faster as the amplitude of the magnetic field pulse is increased. Once the reversed field is turned off, the domain stays the same without expanding or shrinking. Thermally activated domain

wall motion in the low reverse field ( $H_z$ ) in the creep regime can be explained using the creep law as follows [87]:

$$v = v_0 \exp[-\zeta(\mu_0 H_z)^{-\mu}] \quad (4.1)$$

where  $v$  is the domain wall velocity,  $v_0$  is the characteristic speed,  $\mu = 1/4$  [88] is the universal creep exponent,  $\zeta$  is the scaling exponent, and  $\zeta = U_c H_{crit}^\mu / k_B T$ ,  $U_c$  is the energy scaling constant,  $k_B T$  is the thermal energy. The Critical magnetic field  $H_{crit} = \sigma_{DW} \xi / M_s L_c^2$ ,  $\sigma_{DW}$  is the domain wall energy,  $\xi$  is the correlation length of the disorder potential,  $M_s$  is the saturation magnetization, The Larkin length  $L_c = (\sigma_{DW}^2 t_f^2 \xi^2 / \gamma)^{1/3}$ ,  $\gamma$  is the pinning strength of the disorder.  $U_c = \frac{[\mu u_c / 2(\mu+1)\xi]^\mu \sigma_{DW} t_f u_c^2}{(1+\mu)L_c}$ ,  $t_f$  is the film thickness, and  $u_c$  is the roughness of the DW segment with length  $L_c$ .

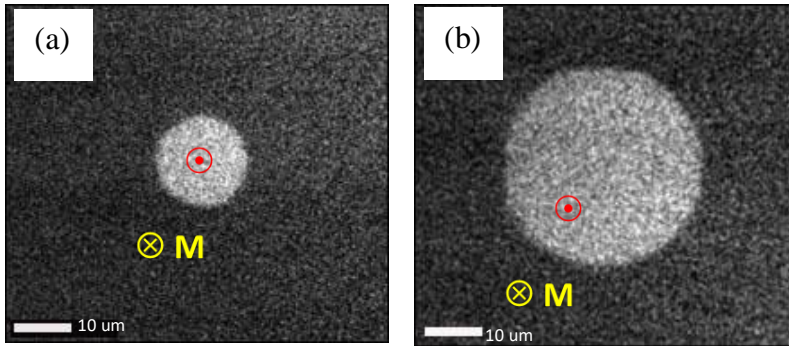


**Figure 4.5** The MOKE images of symmetrical bubble domain expansion with two consecutive reverse magnetic field pulses with same pulse amplitude and duration (315 Oe, 400ms pulse). (a) bubble growth after the 1<sup>st</sup> field pulse. (b) bubble growth after the 2<sup>nd</sup> field pulse.

In order to find the domain wall displacement within the 400 ms field pulse duration, the image of the domain structure before applying the 315 Oe, 400ms, +Z field pulse was recorded and saved as the reference image (Figure 4.6 (a)). Then the domain structure image after the 315

Oe, 400ms, +Z field pulse is recorded (Figure 4.6 (b)), and then the previously saved reference image (Figure 4.6 (a)) was subtracted from the later image (Figure 4.6 (b)). The obtained, ring-shaped, difference image represents a bubble domain growth during the 315 Oe, 400ms, +Z field pulse. The described technique is usually referenced as differential MOKE imaging (Figure 4.6). The differential image shows the domain wall propagation corresponding to the 315 Oe, 400ms, +Z field pulse.

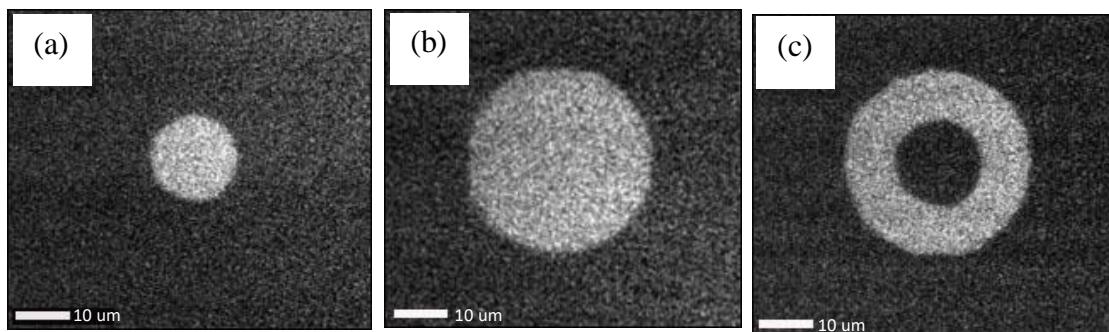


**Figure 4.6** The differential MOKE image domain wall expansion during 315 Oe, 400ms, +Z magnetic field pulse. (a) The image of the domain structure before applying the 315 Oe, 400ms, +Z field pulse (reference image). (b) The image of the domain structure after applying the 315 Oe, 400ms, +Z field pulse. (c) The differential MOKE image which represents the domain wall displacement during the 315 Oe, 400ms, +Z field pulse.

The in-plane magnetic field effect on the nucleated domain structures is investigated. The in-plane magnetic field breaks the rotational symmetry and leads to the asymmetric DW motion due to the DMI-induced homochiral Neel DWs. Similar to the previous reports, applying an in-plane field itself without any out-of-field component does not produce domain wall motion. The in-plane field is used to create asymmetry, while out-of-plane field causes DW motion. Therefore, the application of both in-plane and out-of-plane magnetic fields is required. The out-of-plane field component, in this case, defines the bubble domain expansion rate. Simultaneous

application of two field components is achieved by tilting the electromagnet with respect to the sample plane. The tilt angle defines both x and z magnetic field components. In our experiments a randomly formed small angle  $\alpha = 8.6^\circ$  was used. The magnetic field rotation angle was measured by measuring the magnetic field components and comparing those to magnetic field measured along the electromagnet pole axis. The magnetic field is applied in the form of pulses. The amplitude of the field pulse was selected slightly above the coercive field and the pulse duration was chosen to obtain domain wall motion length of around  $10\mu\text{m}$ . A typical result of differential MOKE measurements on  $[\text{Pt}/\text{Co}/\text{Ni}]_n$  heterostructures is shown in Figure 4.7. Anisotropic domain wall motion parallel to the magnetic field direction was observed. The right side of the DW moves along the in-plane field direction, and the left side of the DW moves against the field direction. The DW moves along the magnetic field faster than against the field. Faster domain wall motion along the in-plane field direction for all the heterostructures indicates positive DMI, and right-handed chiral Neel DWs. For the 1, 2, and 3 try-layer repetitions the domain wall motion asymmetry increases, which is evidence for the increasing DMI field strength. However, for the 4, 5, and 10 repetitions, the asymmetry decreases indicating the decrease of the DMI field.

With the existence of both in-plane ( $H_x$ ) and the out-of-plane magnetic field ( $H_z$ ), the domain wall velocity can be rewritten as:

$$v = v_0 \exp[-\zeta^* (\mu_0 H_z)^{-\mu}] \quad (4.2)$$

where

$$\zeta^* = \zeta(H_x) = \zeta f^\mu(H_x) = \zeta_0 [\sigma_{DW}(H_x) / \sigma_0] \quad (4.3)$$

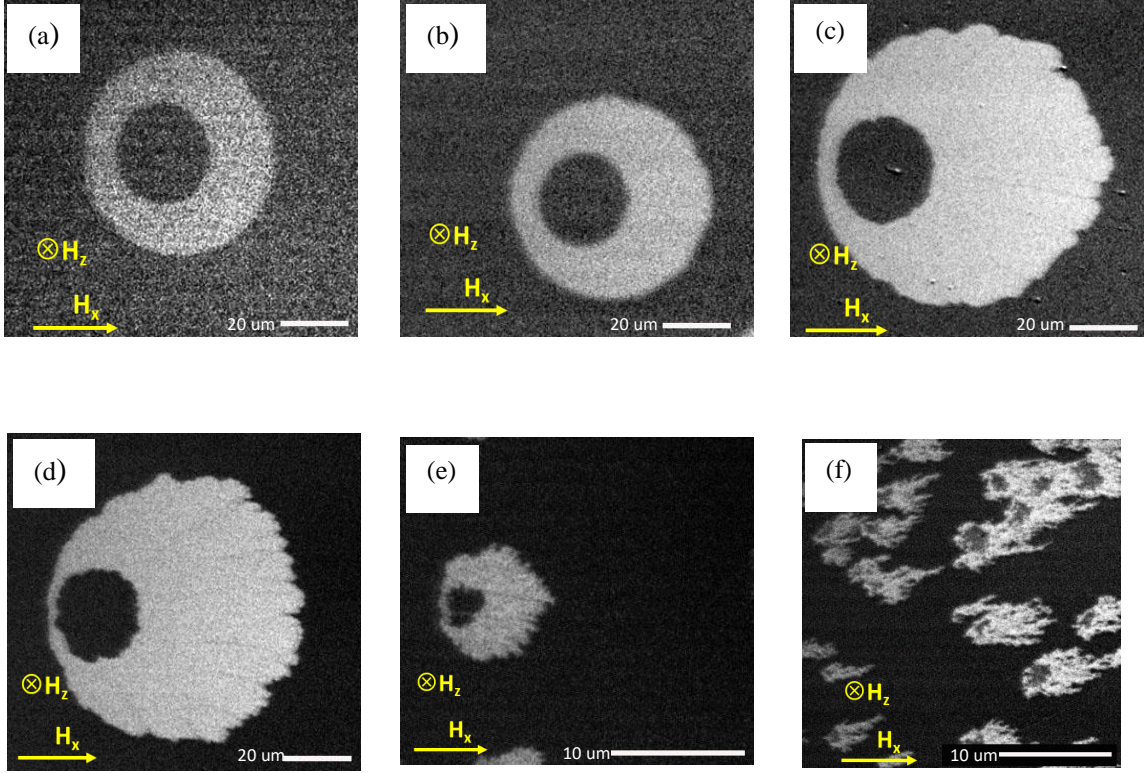


**Figure 4.7** The differential MOKE images of the  $[\text{Pt}/\text{Co}/\text{Ni}]_n$  heterostructures show the anisotropic domain wall displacement parallel to the in-plane field direction. (a) 315 Oe, 400ms pulse (b) 582 Oe, 1000ms pulse (c) 790 Oe, 20000ms pulse (d) 1000 Oe, 6000ms pulse (e) 66800 Oe, 4000ms pulse (f) 60000 Oe, 4000 ms indicate 1, 2, 3, 4, 5, and 10 repetitions of the tri-layer, respectively. The domain wall shape changes from a smooth bubble domain to rough bubble type domain as the number of repetitions increases. The highest DW asymmetry is observed for the 3-layer repetition, which indicates the strongest DMI.

The domain wall energy density due to the DMI can be written in the form of:

$$\sigma_{DW}(H_x, \psi) = \sigma_0 + 2k_D \Delta \cos^2 \psi - \pi \Delta M_s (H_x + H_{DMI}) \cos \psi \quad (4.4)$$

Where the DW anisotropy energy density is  $k_D = N_x \mu_0 M_s^2 / 2$ , the demagnetizing coefficient is  $N_x = t / (t + \Delta)$ ,  $t$  is the total thickness of the magnetic layers, the DW width is  $\Delta = \sqrt{A/k_0}$ ,  $A = 16 \text{ pJ/m}$  is the exchange constant,  $k_0 = \mu_0 (H_k M_s - M_s^2 / 2)$ ,  $H_k$  is the anisotropy field, Bloch DW energy density  $\sigma_0 = 2\pi \sqrt{A/k_0}$ , and  $\psi$  is the angle of the magnetization direction inside the domain wall measured from  $+x$  axis.

The equilibrium angle  $\cos\psi_{eq} = \pi M_s(H_x + H_{DMI})/4k_D$  can be found from the minimization condition  $\partial\sigma_{DW}/\partial\psi = 0$ . Then the domain wall energy in a DMI system with the equilibrium angle can be written as follows:

$$\sigma_{DW}(H_x) = \sigma_0 + \frac{\pi^2 M_s^2 \Delta \mu_0^2 (H_x + H_{DMI})^2}{8k_D} - \frac{\pi^2 M_s^2 \Delta \mu_0^2 (H_x + H_{DMI})^2}{4k_D} \quad (4.5)$$

The DW energy in a DMI system having a mixture of both Bloch-Neel domain walls can be expressed as:

$$\sigma_{DW}(H_x) = \sigma_0 - \frac{\pi^2 M_s^2 \Delta \mu_0^2 (H_x + H_{DMI})^2}{8k_D} ; \text{ when } |H_x + H_{DMI}| < \frac{4k_D}{\pi M_s} \quad (4.6)$$

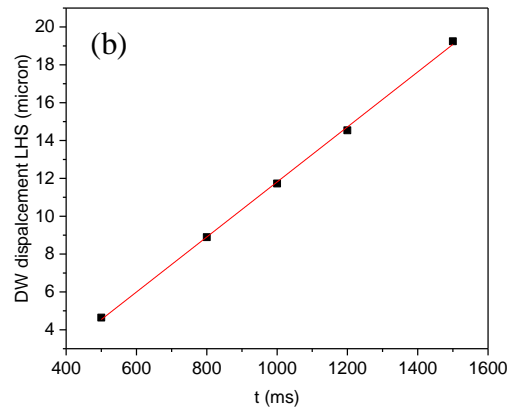
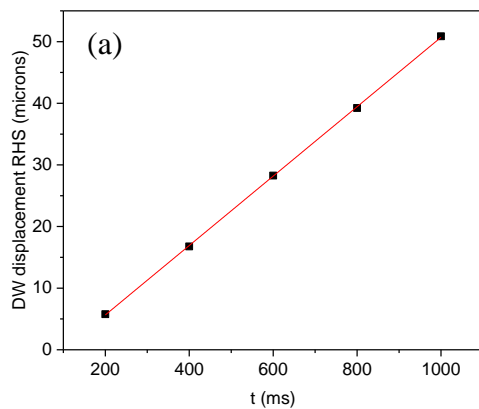
And the DW energy density when the system has pure Neel walls is

$$\sigma_{DW}(H_x) = \sigma_0 + 2k_D \Delta - \pi \Delta \mu_0 M_s |H_x + H_{DMI}| \quad (4.7)$$

The above-discussed creep theory is used to fit the experimental data considering the existence of pure Neel domain walls and Bloch-Neel domain walls, which will be discussed in the next section.

#### 4.4 Extracting DMI in $[\text{Pt}/\text{Co}/\text{Ni}]_n$ heterostructures.

The domain wall displacement for the same magnetic field amplitude but different pulse durations were recorded for samples with  $n = 1$  to 5 tri-layer repetitions. Results of these measurements are shown in Figure 4.8. The linear fit of the displacement versus magnetic pulse duration curves was used to extract the slope representing the DW velocity (Figure 4.8). Several factors defined the measurement error. Firstly, the MOKE signal contrast is proportional to the number of magnetic moments in the sample. That the defined low contrast of the single tri-layer sample. The camera resolution was high enough so that several pixels would fit within the domain wall. Secondly, with a growing number of tri-layer repetitions, dipolar effects play a more significant role and cross-tie like domain walls are observed. This is seen as a rough bubble domain boundary. For the 5 tri-layer repetition, the error of the velocity is larger than that of 1, 2, 3, and 4 repetitions, especially for the DW velocity against the in-plane field direction (Figure 4.8 (d)). The DW displacement for the 10 tri-layer repetition cannot be measured as it has labyrinth type domain growth.



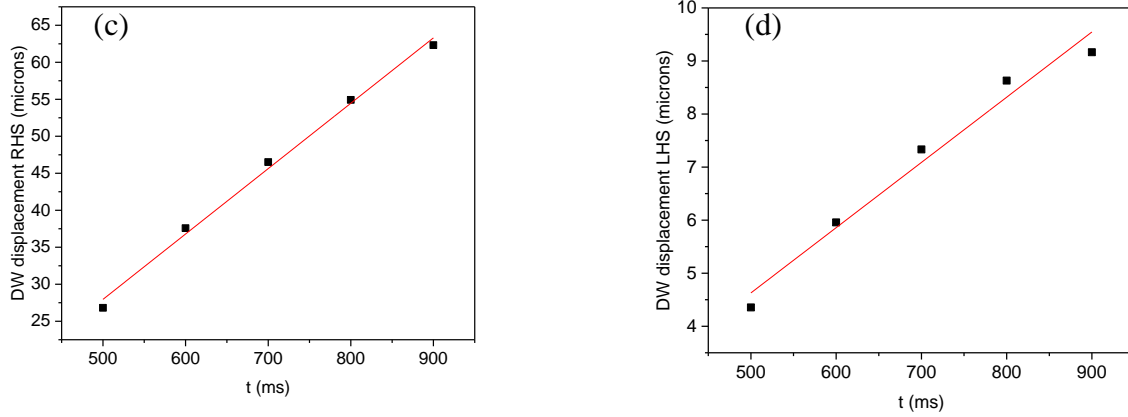


**Figure 4.8** Dependence of DW displacement on the magnetic field pulse duration. Black dots indicate the experimental data and the red line represents the linear best fit. (a) along (b) against the in-plane field for the 1 tri-layer repetition. (c) along (d) against the in-plane field for the 5 repetitions of tri-layers.

For all the PtCoNi heterostructures, domain wall velocities were obtained from the graph of DW displacement versus pulse duration, for several magnetic field amplitudes. The domain wall velocity has an exponential behavior with the in-plane magnetic field. Therefore, the logarithmic DW velocity is plotted as a function of in-plane ( $H_x$ ) magnetic field. The experimental data are fitted using the creep theory for both Bloch-Neel domain wall and pure Neel domain wall conditions.

The Bloch-Neel domain wall velocity equation as a function of in-plane magnetic field is obtained using equations 4.2, 4.3 and 4.6 as follows:

$$\ln(v) = \ln v_0 - \xi_0 \left[ \frac{\mu_0 |H_x| \tan \theta}{1 - C |H_x + H_{DMI}|^2} \right]^{-0.25} \quad (4.8)$$

where the fixed fitting constant is  $C = \pi^2 \Delta \mu_0^2 M_s^2 / 8 K_D \sigma_0$ .

The pure Neel DW velocity as a function of the in-plane field is obtained using equations 4.1, 4.2 and 4.7 and can be written as:

$$\ln(v) = \ln v_0 - \xi_0 \left[ \frac{\mu_0 |H_x| \tan \theta}{F - Q |H_x + H_{DMI}|^2} \right]^{-0.25} \quad (4.9)$$

where, the fitting constants are  $F = \sigma_0 + 2K_D\Delta$  and  $Q = \pi\Delta\mu_0M_s$ .

$\ln v_0$ ,  $\xi_0$ , and  $H_{DMI}$  are the three variable fitting parameters in equations (4.8), and (4.9). In order to calculate the fixed fitting constants  $C$ ,  $F$ , and  $Q$ , saturation magnetization  $M_s$  and effective anisotropy field  $H_k$  were extracted from hysteresis data shown in Figure 4.3.  $K_0$ ,  $\Delta$ ,  $\sigma_0$ ,  $Nx$ ,  $K_D$  were calculated using equations listed above. The effective DMI field region ( $H_{N-B}$ ) in which the Bloch-Neel DW transforms into the pure Neel DW was calculated using the inequality 4.6. The calculated values of the parameters used in fitting constants  $C$ ,  $F$ , and  $Q$  for all PtCoNi heterostructures are listed in Table 4.2. Nonlinear curve fitting with the Levenberg-Marquardt algorithm in the OriginPro software package was used to fit the experimental data. This method adjusts the parameter values in an iterative process based on the Gauss-Newton method and is a steepest descent method.

**Table 4-2** The calculated parameters for the DW velocity fitting

# of repetitions	$H_k$ (A/m)	$t$ (nm)	$M_s$ (A/m) $\times 10^{-5}$	$K_0$ (J/m <sup>3</sup> ) $\times 10^{-5}$	$\Delta$ (m) $\times 10^{-8}$	$\sigma_0$ (J/m <sup>2</sup> ) $\times 10^{-3}$	$Nx$	$K_D$ , J/m <sup>3</sup> $\times 10^{-4}$	$H_{N-B}$ (mT)
1	6366.2	0.6	5.77	2.04	0.88	11.4	0.08	1.73	38.24
2	10350.3	1.8	4.71	1.33	1.09	9.17	0.14	1.97	53.21
3	13702.2	3	4.72	1.32	1.10	9.12	0.21	3.00	80.84
4	15469.7	4.2	4.58	1.23	1.14	8.81	0.27	3.55	98.67
5	18302.8	5.4	4.57	1.21	1.15	8.72	0.32	4.19	116.7
$A = 1.60 \times 10^{-11}$ J/m, Sample width = $6.35 \times 10^{-1}$ cm, $\theta = 8.6^\circ$									

The fixed fitting constants were calculated for the Bloch-Neel DW condition  $C = 7.88 \times 10^{-11} T^2 m^6 / J^2$ , and for the pure Neel DW condition,  $F = 1.0161 J/m^2$  and  $Q = 2.28 \times 10^{-6} mT$ .

The experimental data were fitted with equation (4.8) for all the heterostructures considering the existence of mixed Bloch-Neel DW texture (Figure 4.9).  $H_{DMI}$  was extracted along with the other two variable fitting parameters  $\ln(v_0)$ , and  $\xi_0$  and listed in Table 4.3.

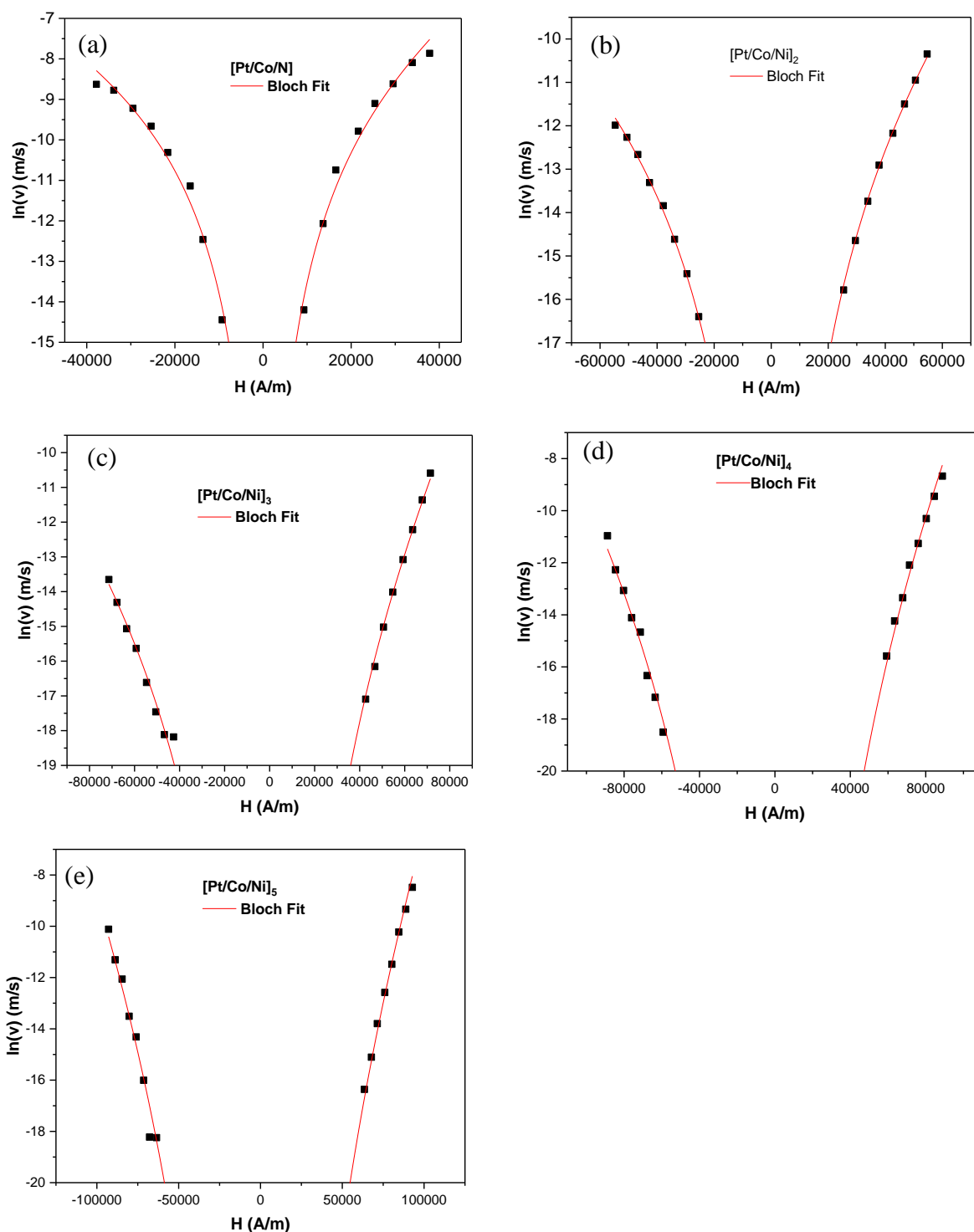


**Figure 4.9** Bloch-Neel DW fit on the graphs of logarithmic DW velocity as a function of in-plane magnetic field for  $[\text{PtCoNi}]_n$ . Black dots indicate experimental data and red curves indicate the best fits of the creep model. (a)  $[\text{PtCoNi}]_1$ , (b)  $[\text{PtCoNi}]_2$ , (c)  $[\text{PtCoNi}]_3$ , (d)  $[\text{PtCoNi}]_4$ , and (e)  $[\text{PtCoNi}]_5$ .

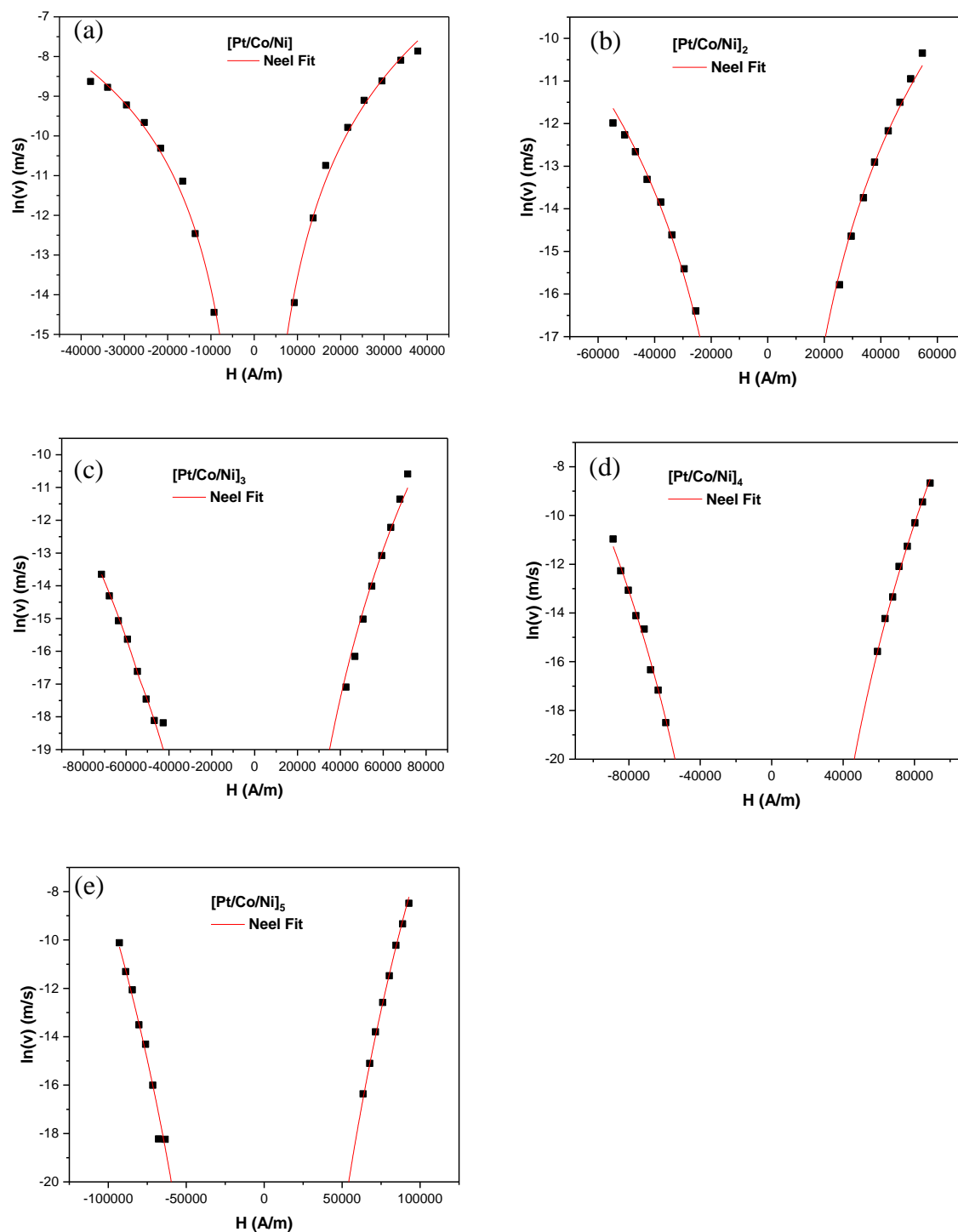


**Figure 4.10** Pure Neel DW fit of experimental data of DW velocity as a function of in-plane magnetic field for  $[PtCoNi]_n$ . (a)  $n=1$ , (b)  $n=2$ , (c)  $n=3$ , (d)  $n=4$ , and (e)  $n=5$ . Black dots indicate the experimental data and red curves indicate the best fits of the creep model.

The creep model was applied assuming pure Neel DW condition based equation (4.9), and fit were made to the experimental DW velocity data as a function of in-plane field (Figure 4.10). For all the PtCoNi heterostructures,  $\ln(v_0)$ ,  $\xi_0$ , and  $H_{DMI}$  values were extracted from the best-fit curves and listed in Table 4.3.

**Table 4-3** The variable fitting parameters obtained from the creep model fits with Bloch-Neel DW, and pure Neel DW conditions on experimental DW velocity vs. in-plane field graphs.

# of repetitions	Bloch-Neel Fitting			Pure Neel Fitting		
	$H_{DMI}$ (mT)	$\xi_0$	$\ln(v_0)$ (m/s)	$H_{DMI}$ (mT)	$\xi_0$	$\ln(v_0)$ (m/s)
1	21±5	3.90±0.10	5.2±0.5	101±93	4.3±0.2	6.5±0.5
2	41±4	6.82±0.08	9.5±0.3	60±5	6.6±0.2	8.7±0.7
3	51±6	12.20±0.40	22.0±1.0	67±7	12.1±0.6	21.0±2.0
4	42±9	16.00±0.70	30.0±2.0	44±2	19.3±0.4	40.0±1.0
5	22±6	25.10±0.90	56.0±3.0	26±2	24.2±0.8	51.0±2.0

The extracted DMI field values for all the tri-layer repetitions are positive, and that indicates the existence of right-handed chiral DWs in all the PtCoNi heterostructures. DMI values obtained from the Bloch-Neel and pure Neel conditions for all the heterostructures are shown in Figure 4.11. The region above the green dashed line is the right-handed Neel DW region and below the blue dashed line is the left-handed Neel DW region. The calculated Bloch-Neel mixed DW region  $|H_{N-B}|$  stays in between the two dashed lines. For both [Pt/Co/Ni]<sub>1</sub>, and [Pt/Co/Ni]<sub>2</sub> structures, the extracted DMI value from the pure Neel DW fit lay in the right-handed Neel DW region while the DMI value obtained from the Bloch-Neel DW fit was located inside the Bloch-Neel DW region. Therefore, the DWs in the 1 and 2 repetitions of PtCoNi could be either pure Neel or mixed Bloch-Neel DWs as the extracted DMI satisfies both DW conditions. The 3, 4 and 5 layer repetitions with the pure Neel wall condition extracted DMI values lay in the Bloch-Neel DW region which do not satisfy the condition requirement. However, for those higher order

repetitions, the DMI obtained from the Bloch-Neel fit agree with the Bloch-Neel DW condition as the values are located in the relevant region. Therefore, the DWs in the 3-5 layer repetitions are identified as mixed Bloch-Neel DWs.

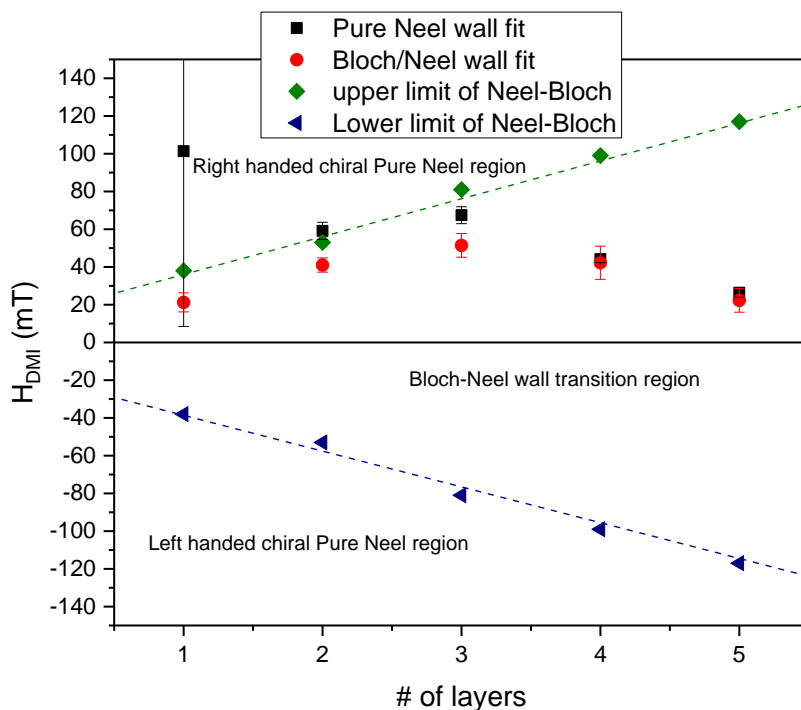


**Figure 4.11** The graph of calculated DMI field with pure Neel condition and the Bloch-Neel condition for 1-5 repetitions of Pt/Co/Ni.

The observed DW motion asymmetry for 1 tri-layer repetition in Figure 4.7 is weaker than the asymmetry of 2 and 3 tri-layer repetitions possibly due to the weaker DM field in the 1 tri-layer. A pure Neel DW structure is not possible in a system with a weaker DM field. Therefore, the 1 tri-layer PtCoNi heterostructure could have mixed Bloch-Neel DW texture. The same explanation is valid for the 2 tri-layer repetitions. The DM field extracted from the creep theory fit is highest for the 3 tri-layer repetition and it analogous to the highest DW motion asymmetry observed in Figure 4.7 (c). The extracted DMI field decreases for the 3 to 5 tri-layer repetitions

due to the large dipolar energy contribution in bulk structures. The magnetic structures with large dipolar energy prefer achiral Bloch DW texture, which reduces the DMI effect in the structure. The rough domain boundaries observed in DW images in Figure 4.7 verify the existence of high dipolar energy in the 3 to 5 tri-layer repetitions.

#### 4.5 Conclusion

The DW motion asymmetry observed from the MOKE images and the extracted DMI values from the creep model verify the right-handed chiral DW texture in our Pt/Co/Ni multilayer structures. However, the extracted DMI values lay in the Bloch-Neel region. Therefore, there may be a mixture of both Bloch and Neel DWs. The observed DW asymmetry demonstrates that the inversion symmetry of the Pt/Co/Pt system has been broken by introducing the Ni layer. Therefore, the asymmetric Pt/Co and Co/Ni interfaces govern the effective DMI in the multilayer structure. The DMI value extracted from the creep theory tends to decrease from 3 to 5 repetitions of Pt/Co/Ni. This indicates that the dipolar energy of the structure increases as the number of repetitions growth, and it favors the Bloch DWs rather Neel DWs. DW motion observations from the MOKE images show rough bubble DWs at the higher number of tri-layer repetitions. Rough DW boundaries arise from the cross-tie DWs which exists in the systems with large dipolar energy. However, optimization of the material thickness and the growth parameters is needed to understand the behavior of interfacial DMI and to enhance the DMI field to obtain pure homochiral Neel DW structures.

## 5 STRIPE DOMAIN MANIPULATION IN MAGNETIC MULTILAYER STRUCTURES WITH PMA

### 5.1 Introduction

In spin wave based logic devices, complex spin wave waveguide geometries like cross junctions, T junctions other than the stripe structures are essential to perform logic operations [89]. Spin wave propagation in complex geometries has been studied [90, 91]. Magnetostatic spin waves propagate in complex structured ferromagnetic films that are typically magnetized in the in-plane direction. Spin wave scattering and reflections occur due to the waveguide shape variation, change in orientation of the spin wave, wave vector and in-plane magnetization direction resulting in mode mismatching. Recently spin wave channeling [90, 92] in Neel domain wall structures was reported. The ability to channel spin waves through controlled domain structures would open new possibilities for reconfigurable spin wave logic devices.

In Chapter 4 of this thesis, we demonstrated labyrinth-like domain formation in ferromagnetic films with PMA. At the same time, PMA films with DMI allow for asymmetric domain growth, which was demonstrated for bubble domains (Chapter 4). In this chapter, we investigate magnetic field control of labyrinth-like domain structures to form stripe domains and manipulate those to form complex domain structures in a controllable manner. Using PMA materials for spin wave logic devices adds another very significant benefit. Ferromagnetic materials with PMA support Forward Volume Magnetostatic spin wave modes (FVMSW). FVMSW dispersion does not depend on the in-plane dimensions of the ferromagnetic film and is defined by the film saturation magnetization and thickness [93]. Patterning ferromagnetic films into structures should not alter the dispersion and thus solve the spin wave mode-mismatching problem in future magnonic logic devices.

## 5.2 Sample Description

Ferromagnetic multilayer structures of  $Ta(4)Cu(5)\{[Co(0.2)Ni(0.8)]_n\}Ta(2)$  with  $n = 8, 9, 10$  are used to study the domain evolution with external magnetic field as the number of bilayer repetitions is increased (Figure 5.1). CoNi ferromagnetic bilayer repetitions were grown on Ta/Cu buffer layer using the DC sputtering technique, and Ta is used as the capping layer. The numbers within the brackets indicate the layer thickness in nanometers. Homochiral Neel DW structure, which is an indication of DMI, is reported for FeNi interface grown on Cu [48]. Therefore, we can expect weak DMI in our CoNi bilayer system grown on a Cu substrate, below a critical thickness where Neel walls transform into Bloch walls. For convenience, I will refer to the above multilayer structures as CoNi structures hereafter.

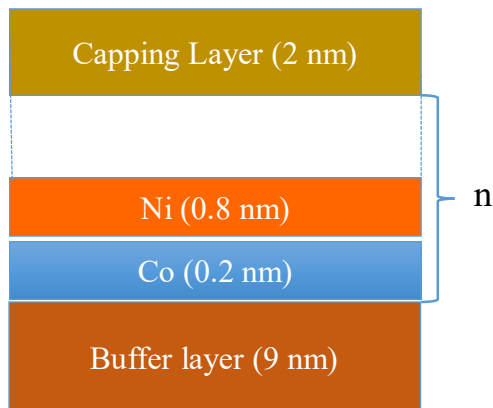


**Figure 5.1** The sketch of the ferromagnetic  $[CoNi]_n$  structure.  $n$  is the number of CoNi bilayer repetitions. The numbers in the brackets indicate the layer thickness in nm.

The out-of-plane hysteresis loops measured by VSM for CoNi multilayer structures are shown in Figure 5.2. The abrupt switching observed in the hysteresis loops indicates that CoNi structures have PMA.

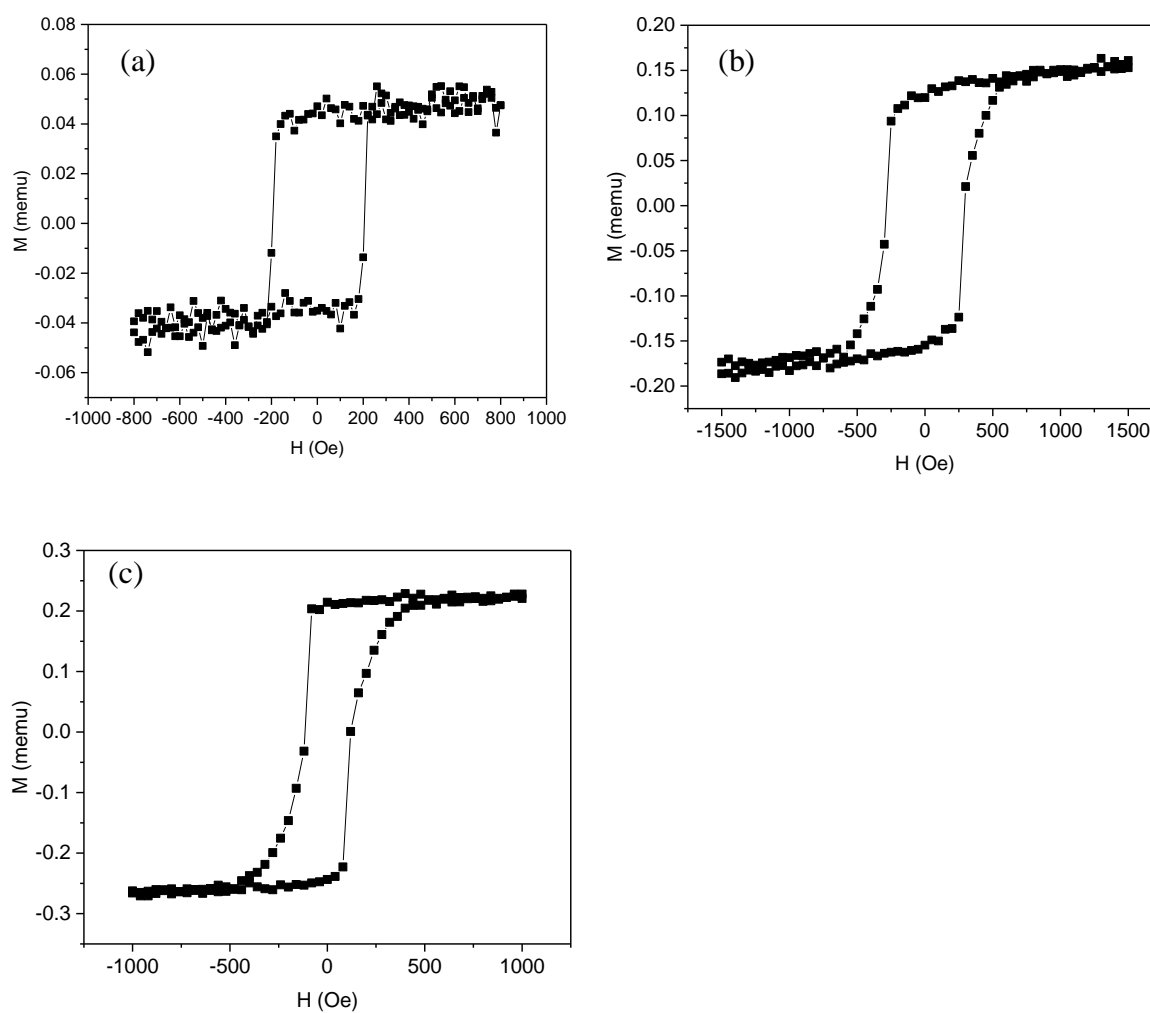


**Figure 5.2** The hysteresis loops of  $[\text{CoNi}]_n$  heterostructures obtained from Vibrating Sample Magnetometer. (a)  $n=8$ , (b)  $n=9$ , (c)  $n=10$ .

**Table 5-1** The coercive fields of  $[\text{CoNi}]_n$  extracted from hysteresis loops

CoNi structure	Coercive field, $H_c$ (Oe)
$[\text{CoNi}]_8$	170
$[\text{CoNi}]_9$	190
$[\text{CoNi}]_{10}$	78

### 5.3 MOKE measurements and domain evolution

DW evolution in CoNi multilayer structures was imaged using polar MOKE microscopy. See Chapter 3 for detailed description of the experimental setup. Magnetic multilayers were saturated using a ( $-H_z$ ) magnetic field (1000 Oe). Then a small reverse field ( $+H_z$  field) which is slightly above the coercive field (see Table 5-1) is applied to nucleate the domains in the creep regime. Typically domains nucleate at a defect or an impurity (Figure 5.3 (a)) and then grow rapidly in the labyrinth form defined by the random energy profile as shown in Figure 5.3 (b) and (c).

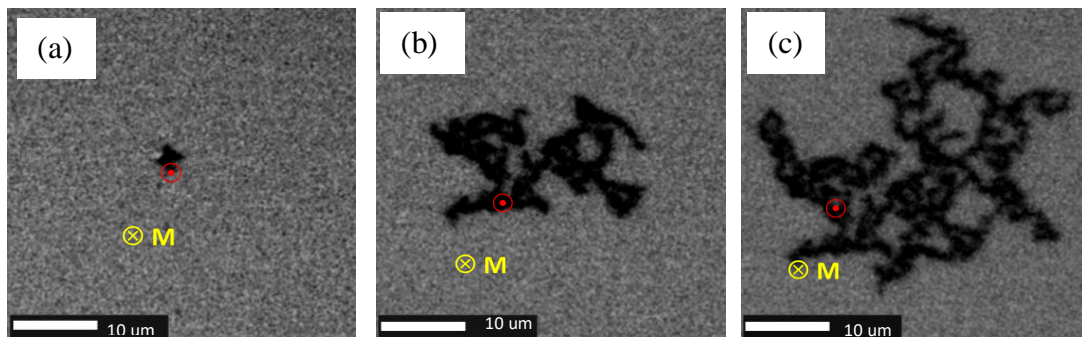


**Figure 5.3** MOKE images of domain evolution of  $[\text{CoNi}]_9$  with out-of-plane magnetic field. (a)-(c) The nucleated domain grows isotropically in the form of a dendritic type domain with continuous field pulses. (a) 200Oe, 100ms first field pulse (b) 200Oe, 100ms second field pulse (c) 200Oe, 100ms third field pulse.

The above procedure was repeated for all the three CoNi multilayer structures. Labyrinth type domain growth was observed in the presence of the reversed field ( $H_z$ ) (Figure 5.4). The two-step magnetization reversal process comprising domain nucleation and consequent growth with the out-of-plane field is observed. For some field amplitudes, the formation of new nucleation centers is observed while the existent domains are growing (Figure 5.4 (d)). This observation indicates that for the higher number of repetitions of CoNi, either the concentration of intrinsic defect and impurities is higher or the spatial energy profile variation originating from

these defects is much larger than that in thin structures with 1-4 bi-layer repetition. The domain nucleates at the defect similar to the domain nucleation in thin structures. With the out-of-plane field, it grows in labyrinth form rather bubble domains due to the large dipolar fields. The dipolar field contribution in the structure increases as the number of bilayer repetitions grows. The strong dipolar fields arising from the neighboring magnetic moments aligned in the (-z) direction stabilize the domain boundaries in z direction. This prevents domain wall from expanding symmetrically, and the domain tends to grow in a path where the dipolar field is minimum.

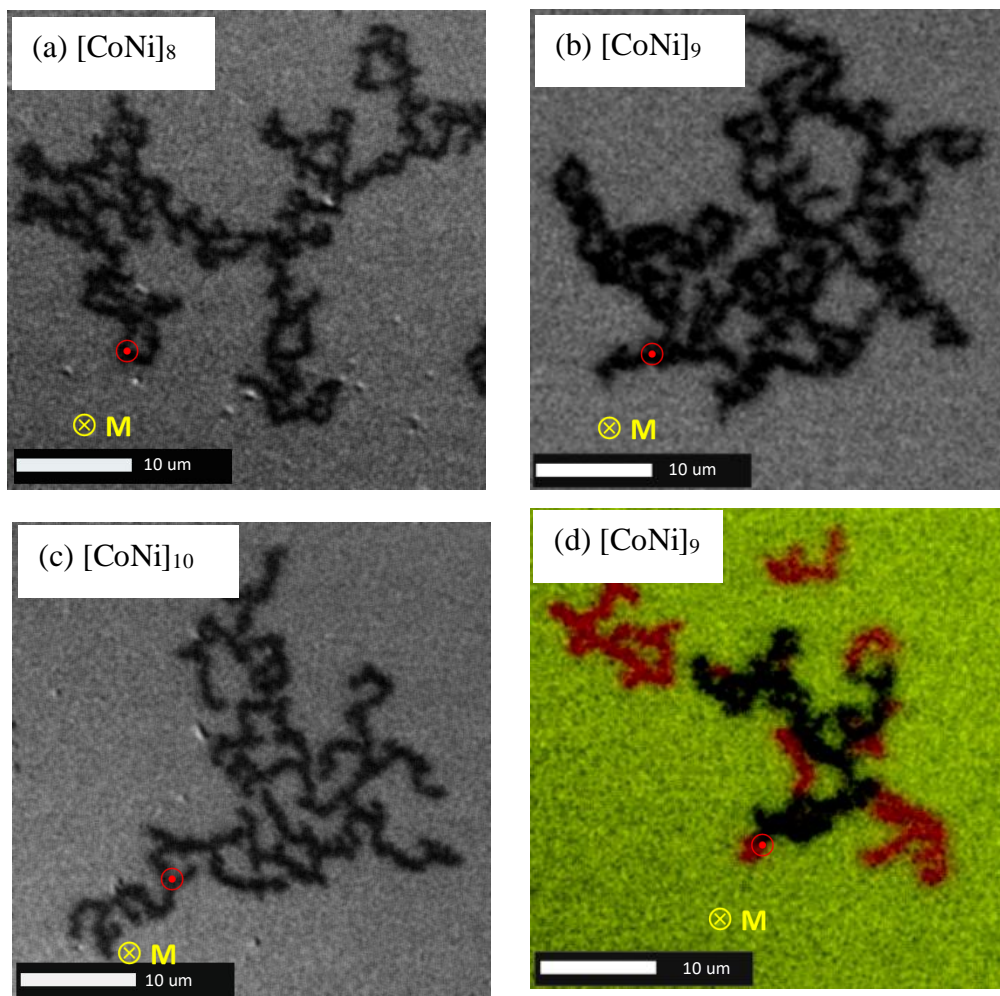


**Figure 5.4** MOKE images of domain evolution with out-of-plane magnetic field. (a)  $H_z = 220\text{Oe}$ , 150ms (b)  $H_z = 200\text{Oe}$ , 300ms (c)  $H_z = 78\text{Oe}$ , 200ms (d) formation of new nucleation centers while the existing centers are growing. The black color indicates the grown domain with the previous field pulse and red color indicates growth of new domains.

field in CoNi multilayer structures. In the first step, domains were nucleated by applying a short field pulse slightly larger than the coercive field ( $H_{ZN}$ ) (see Table 5-1) of the structure along the +Z direction as shown in Figure 5.3. In the second step, an in-plane magnetic field is applied in combination with the out-of-plane magnetic field component. The effect of the in-plane field on the nucleated domain is similar to that found using the approach used in Chapter 4 to study bubble domain evolution. An experimental approach of magnet rotation similar to the one described in chapter 4 was used to generate a combination of in-plane and out-of-plane field pulses. The electromagnet was rotated to form angle  $\alpha = 6.2^\circ$  between the field direction and the sample plane as shown in Figure 4.4 (b). That resulted in a small out-of-plane field component and a symmetry-breaking in-plane field component ( $H_x$ ). The Hall sensor was used to measure the precise magnet rotation angle by measuring its magnetic field components. The effect of the in-plane magnetic field ( $H_x$ ) with a small out of field component ( $H_z$ ) on the size of nucleated domain structures was investigated. The results from an in-plane  $H_x$  field and reversed out-of-plane  $H_z$  field both applied simultaneously to the nucleated domain centers are shown in Figure 5.3 (a). For all three magnetic multilayer structures, domain growth is observed along the in-plane direction as shown in Figure 5.5. Labyrinth type domain growth is observed for the 8 repetitions of CoNi bilayers (Figure 5.5 (a)) while stripe type domains are observed for the higher number of bilayer repetitions (Figure 5.5 (b) and (c)). With the increase of the thickness of the magnetic structures, dipolar energy increases while the exchange energy, magnetostatic and magnetocrystalline anisotropy energies stay the same. Large dipolar energy makes the stripe domain structures more stable than dendritic or bubble domain types. Domain walls grow asymmetrically along the in-plane field direction. Therefore, the domain wall type cannot be Bloch walls as it favors symmetrical domain wall motion as Bloch walls have uniform energy density parallel to the in-plane field. Asymmetric

domain wall motion can derive from the creep theory assuming a given asymmetric domain wall energy density. As discussed in Chapter 4, the intrinsic field that arises due to DMI generates domain wall energy density variations which lead to asymmetric domain wall motion. If so, Neel DWs with right-handed chirality could exist in CoNi heterostructures. However, above a certain critical thickness of the magnetic structure, the DMI effect decreases and Neel walls are transformed into Bloch walls. Therefore, it is not certain that existence of Neel domain walls exist at this high thickness with 8 and 9 repetitions of the CoNi bilayer. Further investigation is needed to understand the domain wall type and to verify the existence of DMI.

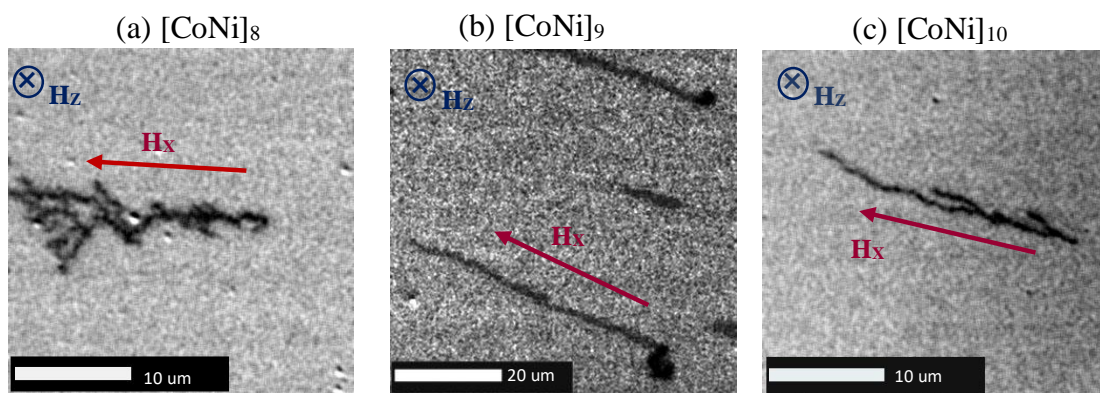


**Figure 5.5** The MOKE images of domain evolution of a nucleation center for  $[\text{CoNi}]_n$ , with the in-plane field plus a small out-of-plane field component. (a)  $H_{ZN} = 180\text{Oe}$ , 100ms;  $H = 1050\text{Oe}$ , 300ms (b)  $H_{ZN} = 200\text{Oe}$ , 100ms;  $H = 1980\text{Oe}$ , 100ms (c)  $H_{ZN} = 110\text{Oe}$ , 100ms;  $H = 950\text{Oe}$ , 200ms

Single stripe domain growth or stripe domains with less branching are favorable for domain wall manipulation studies as well as for domain wall logic applications. Therefore, we further investigated domain wall evolution in the higher number of bilayer repetitions of CoNi structures ( $n=9$  and 10).

The in-plane field effect on the domain structures of various sizes was investigated. The in-plane field with a small out-of-plane field component was applied to the samples with different sizes of domains formed by the out-of-plane field. Stripe domains, grew from the nucleated domains and also from the places where no domains can be observed (Figure 5.6(a)). As shown in Figure 5.6(b) stripe domain grew from at least two different points of the middle sized domain, and also from an impurity where no initial domains formed. Also, in the large-sized domain, stripes grew from multiple domain points (Figure 5.6(c)). The grown stripe domains, especially domains growing from the medium and large size domains, have branching and wavy shape. This result indicates that stripe domains grow along the in-plane field direction irrespective of the size of the nucleated domain structure.

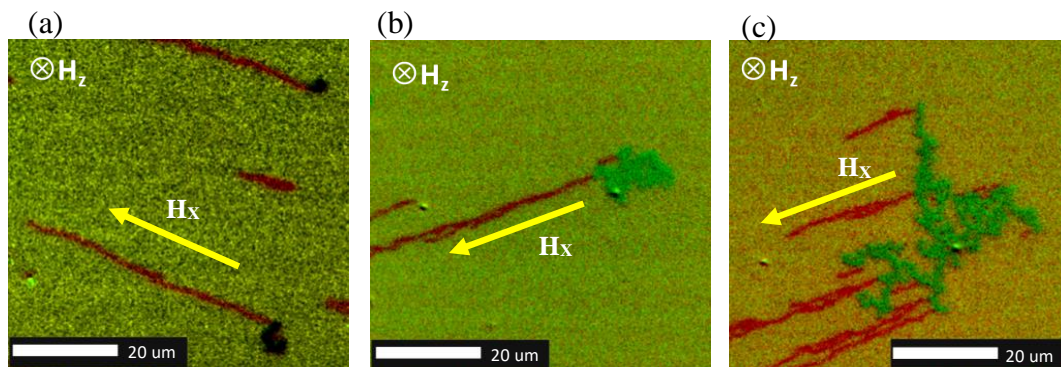


**Figure 5.6** MOKE images of domain evolution in  $[\text{CoNi}]_9$  from (a) nucleated domain;  $H_{ZN}= 200\text{Oe}$ ,  $100\text{ms}$ ;  $H= 1980\text{Oe}$ ,  $100\text{ms}$  (b) middle sized domain;  $H_{ZN}= 200\text{Oe}$ ,  $140\text{ms}$ ;  $H= 1900\text{Oe}$ ,  $100\text{ms}$ , (c) Large sized domain;  $H_{ZN}= 200\text{Oe}$ ,  $180\text{ms}$ ;  $H=1850\text{Oe}$ ,  $100\text{ms}$ . The domain structure formed with reverse field is shown by the solid green color. The stripe domains growth along the in-plane field are shown by red color.  $H_{ZN}$  is the reverse field which formed the domains.

In order to demonstrate the field-defined domain growth direction, a set of experiments with the in-plane magnetic field applied at different angles was carried out. A two-cycle study was

performed applying an in-plane field in two different directions  $H_1$  and  $H_2$ . Each cycle was independent of the other as the domains from the first cycle were erased completely before starting the second cycle. The in-plane field was applied with the small out-of-plane field component ( $H$ ) that enabled the domain growth. First, a small domain was nucleated by applying a reversed out-of-plane magnetic field ( $H_{ZN}=200\text{Oe}$ , 100ms) to the saturated magnetic structure. Then, the in-plane magnetic field pulse is applied with a small out-of-plane field component to the nucleated domain ( $H_1$ ). Typical results of this experiment are shown in Figure 5.7. The stripe domain growth was observed along the  $H_1$  in-plane magnetic field direction. Dark MOKE contrast (switching magnetization from grey to black) was used. The MOKE image obtained was saved and used as a reference frame for subsequent experiment steps. Then all domain textures were erased completely by saturating the film via applying the ( $-H_z$ ) field. The domain nucleation and growth was repeated with the  $H_2$  field, using the saved domain image as a reference. That resulted in image revealing domain structures in the first and second formation cycles. The first cycle domains are shown as black areas while the second cycle domains are revealed as white areas of the images. Some of the second-cycle domains nucleated at same positions while the formation of new domains at positions different from the first-cycle was observed. Domain nucleation and stripe domain growth along the new field direction is independent of the previous growth cycle. These results indicate that it is the magnetic field that defines the growth direction of the stripe domains. Crystallographic sample orientation does not have any effect on the domain growth in these samples.

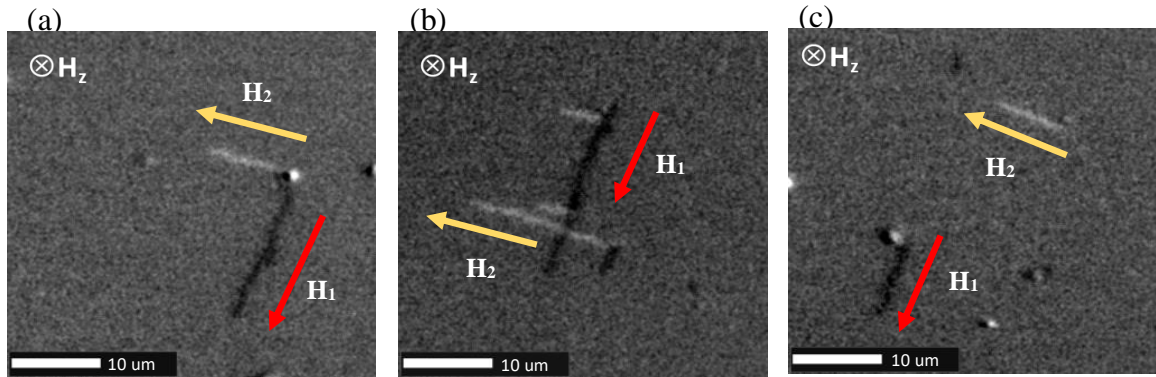


**Figure 5.7** Kerr images of possible independent domain growth along two different in-plane magnetic field directions  $H_1=1900\text{Oe}$ , 100ms and  $H_2=1900\text{Oe}$ , 100ms on  $[\text{Co/Ni}]_9$ . (a) domains grow starting from the same nucleation center in both directions. (b), (c) domains start to grow from different nucleation centers for the two different growth directions.

The length of the stripe domain segments grown on the CoNi bilayer structures is different for pulses with the same magnetic field amplitude and pulse duration. A set of experiments revealing stripe domain growth statistics was carried out. Stripe domain segment length was measured for the  $[\text{CoNi}]_9$  sample. A 100 ms long magnetic field pulse with 1980 Oe magnitude pointed at  $6.2^\circ$  angle was applied. An image typically containing several stripe domains was recorded. Domain lengths were measured. This procedure was repeated 10 times. Results of these measurements are summarized in Figure 5.8. The graph in Fig.5.8 reveals a Gaussian-type distribution with the highest count of 10 – 25  $\mu\text{m}$  long domains. Domains were nucleated and grown at the creep regime. The material disorder impurities and pinning sites define the domain wall motion in this regime, resulting in random stripe length for the same field pulse. The randomly distributed impurities over the structure generate domain wall jumps from one pinning site to another located at different distances. The randomness of the stripe domain length could be attributed to the above reasons. In order to implement stripe domain dynamics in logic applications, all the domains belonging to same functionality need to be controlled with a single

global magnetic field. It is difficult to have such controllability over the domain growth in a magnetic structure, but forming artificial impurity centers in patterned structures using lithography should give good control of stripe domain manipulation with an external magnetic field.

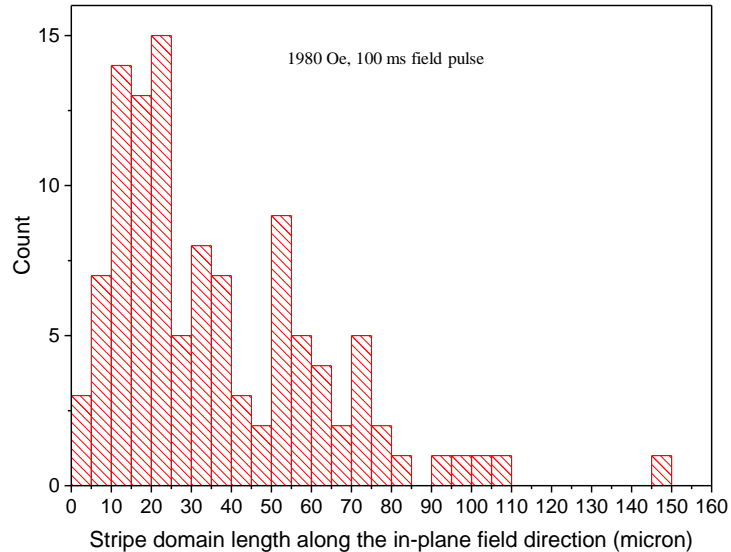


**Figure 5.8** Probability distribution of stripe domain length measured at 1980 Oe, 100 ms field pulse.

Stripe domain manipulation with varying in-plane magnetic field was studied. Similarly, to the experiments described above a combination of in-plane and out-of-plane magnetic field pulses were used to control the growth of stripe domains. First, the 100ms field pulse was applied along  $H_1$  direction (as defined in Figure 5.9). Stripe domain growth along the field was observed. Then, without erasing the formed domain, another 100ms magnetic field pulse  $H_2$  was applied at  $90^\circ$  with respect to the first  $H_1$ . The second field pulse resulted in stripe domain growth along  $H_2$  direction originating from the stripe domain formed by  $H_1$ . As a result, a  $90^\circ$  angled domain structure formed (Figure 5.9 (a)). The same procedure was repeated for different in-plane field

turning angles for both  $[\text{CoNi}]_9$  and  $[\text{CoNi}]_{10}$ . For all the angles the second field pulse defined the growth direction of the stripe domain. MOKE images of stripe domain manipulation at different directions of the second field pulse are shown in Figure 5.9. The  $H_2$  field pulse stripe domains appear to grow from the end point of the  $H_1$  field pulse stripe domains. Small length stripe domains grown along the  $H_2$  field direction from the local energy minimum points of the  $H_1$  stripe domains can be observed. New nucleation centers form (Figure 5.9 (b)) and their growth along the  $H_2$  field pulse direction until it meets the  $H_1$  field pulse stripe domain (Figure 5.9 (c)) is observed. Some of the stripe domains formed by the  $H_1$  field pulse are likely to stay without growing along the  $H_2$  field pulse as the film does not have activated low energy defects along  $H_2$  field direction.

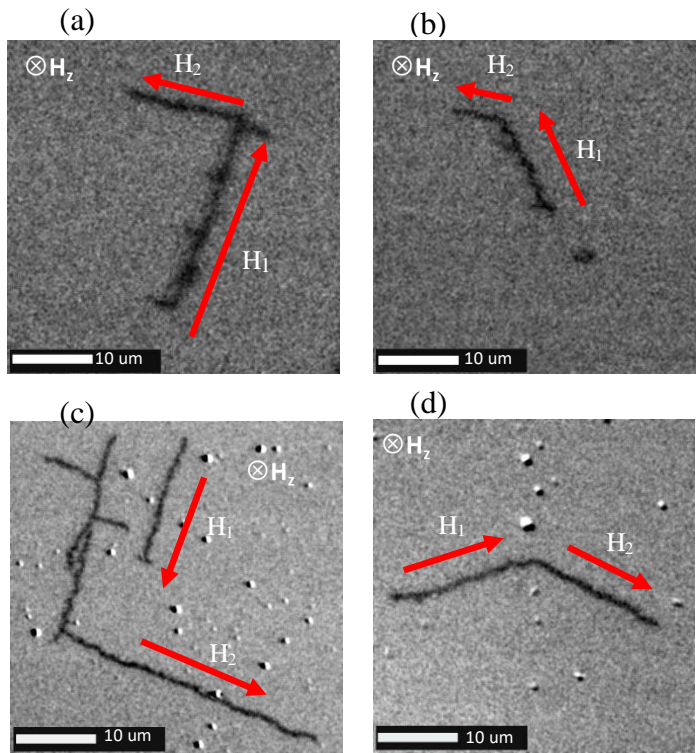


**Figure 5.9** MOKE images of stripe domain manipulation by varying the in-plane magnetic field direction. Stripe domain turns by (a)  $90^\circ$  and (b)  $130^\circ$  in  $[\text{CoNi}]_9$  structure.  $H_{ZN}= 200\text{Oe}$ ,  $100\text{ms}$ ;  $H=1900\text{Oe}$ ,  $100\text{ms}$ . Stripe domain turns by (c)  $90^\circ$  and (d)  $130^\circ$  in  $[\text{CoNi}]_{10}$  structure.  $H_{ZN}= 110\text{Oe}$ ,  $100\text{ms}$ ;  $H=950\text{Oe}$ ,  $200\text{ms}$ . The  $H_1$  is the first field pulse direction and  $H_2$  is the second field pulse direction.

Stripe domain manipulation can be used to form complex magnetic textures like variable angle intersections, circle segments by varying the direction of the in-plane field (Figure 5.10). Stripe domains were grown by a similar procedure as discussed in the previous section. Figure 5.10 (a, b, c) shows stripe domain growth with  $90^\circ$  and  $45^\circ$  turning angles of in-plane field. Circle segments as shown in Figure 5.10 (d) can be formed by turning the in-plane field direction in small angle increments. However, at a critical magnetic field angle, domain growth is observed not only from the end point of the previous domain but also from the local energy minimum points on the arc domain.

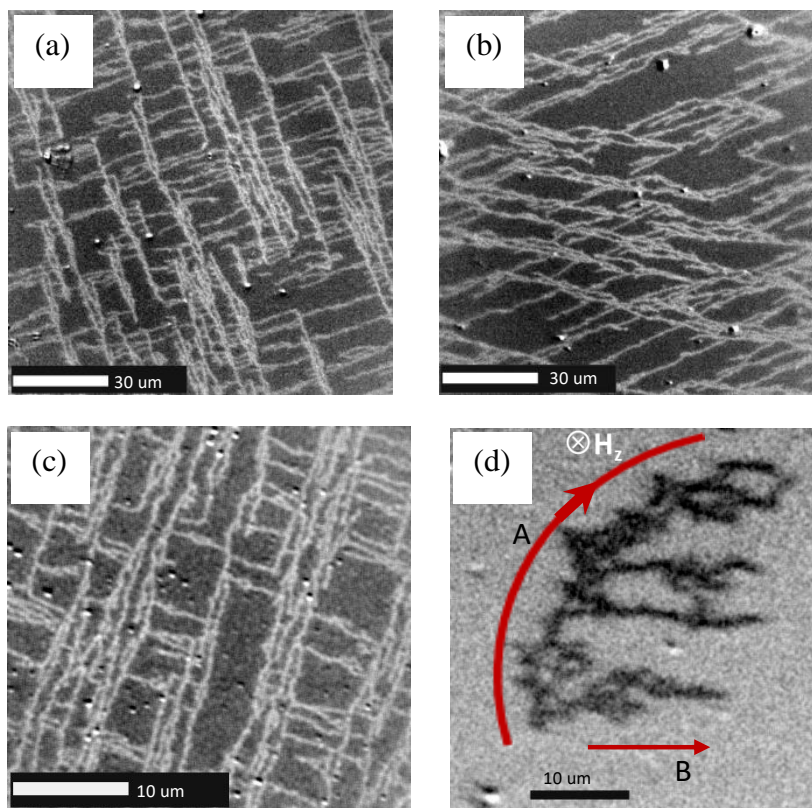


**Figure 5.10** Kerr images of complex geometry of stripe domain manipulation with in-plane magnetic field as field turns by  $90^\circ$  in (a),  $45^\circ$  in (b), and in a circle segment in (d), for  $[Co/Ni]_9$  structure and by  $90^\circ$  for  $[Co/Ni]_{10}$  structure in (c). The direction A indicates the primary field direction of magnetic field rotation and direction B is the field direction at the critical angle.

## 5.4 Conclusion

Higher concentration of impurities and defects define the random energy profile in the CoNi structure, at a higher number of bilayer repetitions. The random energy profile defines a labyrinth type domain growth rather than the bubble domain growth, originating from the nucleation centers. Domain growth along the in-plane field direction could be due to the existence of weak DMI in CoNi magnetic layers. Larger dipolar energy in the bulk structures favors wavy-shaped stripe domain growth rather dendritic domain growth along the in-plane field. Wavy-shaped stripe domains grow along the in-plane field direction irrespective of the size of the nucleated domain. A non-uniform distribution of impurity centers and defects defines the random length distribution of stripe domains for the same field amplitude and pulse duration. Stripe domains can be manipulated with the in-plane magnetic field to form complex magnetic structures with variable angle intersections and circle segments. Those components are essential for domain wall logic, and also in spin wave logic, to overcome mode mismatch in complex geometries. More control over the structure is needed to address the randomness of the stripe domain length, and to have a uniform distribution of nucleation centers. Patterned magnetic structures with artificial impurity centers could overcome issues arising from the random energy profile of the structure and would be a good platform to investigate stripe domain manipulation with an external magnetic field with better controllability.

## 6 SUMMARY

In summary, domain wall dynamics in ferromagnetic CoNi and CoNiPt multilayer structures were observed and studied using polar MOKE. The magnetic field-driven domain wall motion technique was used to study magnetic interactions in these materials. Domain wall creep theory was used to fit the experimental data.

DMI interaction in PtCoNi multilayer structures was studied for 1 to 10 tri-layer repetitions. A Ni layer was introduced to the PtCoPt system to break the inversion symmetry. Hysteresis data was obtained to confirm the presence of PMA in the studied heterostructures. Asymmetric domain wall motion indicating non-zero interfacial DMI in presence of both in-plane and out-of-plane magnetic fields was observed. Experimental data on the DW velocity dependence on the in-plane field was fitted using creep theory for both Bloch-Neel domain wall and pure Neel domain wall conditions to extract the DMI effective field. For all the studied CoNiPt heterostructures, the obtained positive DMI values in the Bloch-Neel domain wall transition region indicate that the DWs in PtCoNi heterostructures are mixed Bloch-Neel domain walls. DMI values tend to decrease from 3 to 5 repetitions of CoNiPt tri-layers due to the increase in dipolar energy. As the number of tri-layer repetitions increases, rough DW boundaries were observed, and this indicates the existence of a large dipolar energy in the system. In order to enhance the DMI in PtCoNi heterostructures to be strong enough to transform Bloch-Neel DWs into Pure Neel DWs, further optimization of structural and growth parameters is needed.

Stripe domain manipulation with an external magnetic field in  $[\text{CoNi}]_n$  heterostructures for  $n = 8,9,10$  was studied. Similar to the PtCoNi heterostructures, domains were nucleated from local minimum energy impurities or defects. Labyrinth type domain growth with the out-of-plane field was observed due to the large dipolar energy at a higher number of repetitions. Wavy-shaped stripe

domain growth along the in-field direction was observed irrespective of the domain size. Asymmetric domain growth along the in-plane direction could be due to the existence of DMI in the magnetic structure. Stripe domain manipulation with magnetic field leads to formation of complex magnetic textures. We experimentally demonstrated formation of variable angle stripe domain bends, circle segments, as well as variable angle stripe domain grids. A random energy profile arises from high concentrations of defects in structures with a large number of CoNi bilayer repetitions. That reduces our ability to control the stripe domain growth, in particular, nucleation location and growth length. Future work will be aimed at developing structures with better control over the stripe domain growth. This can be achieved using artificially introduced defects such as lithographically formed nano-scale dots. Such defects will have lower domain nucleation energies. Therefore, domain nucleation and propagation will not be a random process but rather controlled by the investigator.

## REFERENCES

1. Hilbert, M. and P. López, *The world's technological capacity to store, communicate, and compute information*. science, 2011. **332**(6025): p. 60-65.
2. Dieny, B., et al., *Magnetoresistive sensor based on the spin valve effect*. 1993, Google Patents.
3. Heim, D.E. and S.S. Parkin, *Magnetoresistive spin valve sensor with improved pinned ferromagnetic layer and magnetic recording system using the sensor*. 1995, Google Patents.
4. Dieny, B., et al., *Magnetoresistive sensor based on the spin valve effect*. 1992, Google Patents.
5. Dill, F.H., et al., *Shielded magnetic tunnel junction magnetoresistive read head*. 1999, Google Patents.
6. Parkin, S.S.P., et al., *Exchange-biased magnetic tunnel junctions and application to nonvolatile magnetic random access memory (invited)*. Journal of Applied Physics, 1999. **85**(8): p. 5828-5833.
7. Sin, K. and Y. Chen, *Spin-dependent tunneling read/write sensor for hard disk drives*. 2006, Google Patents.
8. Skyrme, T.H.R., *A unified field theory of mesons and baryons*. Nuclear Physics, 1962. **31**: p. 556-569.
9. Fert, A., V. Cros, and J. Sampaio, *Skyrmions on the track*. Nature nanotechnology, 2013. **8**(3): p. 152.
10. Allwood, D.A., et al., *Magnetic domain-wall logic*. Science, 2005. **309**(5741): p. 1688-1692.
11. Moskowitz, B.M., *Hitchhiker's Guide to Magnetism*. 1991, Institute for Rock Magnetism.
12. B. D. Cullity, C.D.G., *Introduction to Magnetic Materials*. 2nd Edition ed. Dec 2008: Wiley-IEEE Press.
13. Spaldin, N.A., *Magnetic Materials: Fundamentals and Applications*. 2010: Cambridge University Press.
14. CW, C., *Magnetism and metallurgy of soft magnetic Materials*. . 1986, New York: Dover Publications.
15. Néel, L., *Anisotropie magnétique superficielle et surstructures d'orientation*. J. Phys. Radium, 1954. **15**: p. 225-239.
16. U Gradmann, J.M., *Flat ferromagnetic, epitaxial 48Ni/52Fe (111) films of few atomic layers*. physica status solidi (b), 1968. **27**(1): p. 313.
17. Carcia, P.F., A.D. Meinhaldt, and A. Suna, *Perpendicular magnetic anisotropy in Pd/Co thin film layered structures*. Applied Physics Letters, 1985. **47**(2): p. 178-180.
18. Carcia, P.F., *Perpendicular magnetic anisotropy in Pd/Co and Pt/Co thin-film layered structures*. Journal of Applied Physics, 1988. **63**(10): p. 5066-5073.
19. den Broeder, F.J.A., et al., *Perpendicular Magnetic Anisotropy of Co-Au Multilayers Induced by Interface Sharpening*. Physical Review Letters, 1988. **60**(26): p. 2769-2772.
20. Sakurai, M., T. Takahata, and I. Moritani, *Magnetic and Magneto-Optical Properties of Co/Ru Multilayers*. IEEE Translation Journal on Magnetism in Japan, 1992. **7**(2): p. 176-182.
21. den Broeder, F.J.A., W. Hoving, and P.J.H. Bloemen, *Magnetic anisotropy of multilayers*. Journal of Magnetism and Magnetic Materials, 1991. **93**: p. 562-570.

22. Johnson, M.T., et al., *Magnetic anisotropy in metallic multilayers*. Reports on Progress in Physics, 1996. **59**(11): p. 1409.
23. Stöhr, J., *Exploring the microscopic origin of magnetic anisotropies with X-ray magnetic circular dichroism (XMCD) spectroscopy*. Journal of Magnetism and Magnetic Materials, 1999. **200**(1): p. 470-497.
24. Krishnan, R., M. Porte, and M. Tessier, *Bulk and surface anisotropy in ultrahigh vacuum deposited Co / Ag and Fe / Ag multilayers*. Journal of Magnetism and Magnetic Materials, 1992. **103**(1): p. 47-49.
25. Smardz, L., et al., *Structure and magnetic anisotropy of Pd/Ni and Cu/M (M = Fe, Co, Ni) superlattices*. Journal of Magnetism and Magnetic Materials, 1992. **104-107**: p. 1885-1886.
26. Bruno, P., *Dipolar magnetic surface anisotropy in ferromagnetic thin films with interfacial roughness*. Journal of Applied Physics, 1988. **64**(6): p. 3153-3156.
27. O'Handley, R.C., *Modern Magnetic Materials Principles and Applications*. 2003: Wiley-Interscience Publication
28. Koyama, T., et al., *Observation of the intrinsic pinning of a magnetic domain wall in a ferromagnetic nanowire*. Nature materials, 2011. **10**(3): p. 194.
29. Hubert, A. and R. Schäfer, *Magnetic Domains: The Analysis of Magnetic Microstructures*. 2008: Springer Berlin Heidelberg.
30. Szabolcs, H., et al., *Domain wall motion in ferromagnetic systems with perpendicular magnetization*. Journal of Magnetism and Magnetic Materials, 2009. **321**(13): p. 1912-1918.
31. Schellekens, A., et al., *Electric-field control of domain wall motion in perpendicularly magnetized materials*. Nature communications, 2012. **3**: p. 847.
32. Miron, I.M., et al., *Fast current-induced domain-wall motion controlled by the Rashba effect*. Nature materials, 2011. **10**(6): p. 419.
33. L.D.Landau, E.M.L., *On the theory of the dispersion of magnetic permeability in ferromagnetic bodies*. Physikalische zeitschrift der Sowjetunion, 1935. **8**: p. 153.
34. Sang-Koog, K., *Micromagnetic computer simulations of spin waves in nanometre-scale patterned magnetic elements*. Journal of Physics D: Applied Physics, 2010. **43**(26): p. 264004.
35. Prabhakar, D.D.S.A., *Spin Waves, Theory and Applications*. 2009: Springer.
36. Gilbert, T.L., *A phenomenological theory of damping in ferromagnetic materials*. IEEE Transactions on Magnetics, 2004. **40**(6): p. 3443-3449.
37. Beach, G.S.D., M. Tsoi, and J.L. Erskine, *Current-induced domain wall motion*. Journal of Magnetism and Magnetic Materials, 2008. **320**(7): p. 1272-1281.
38. Mougin, A., et al., *Domain wall mobility, stability and Walker breakdown in magnetic nanowires*. EPL (Europhysics Letters), 2007. **78**(5): p. 57007.
39. Metaxas, P., et al., *Creep and flow regimes of magnetic domain-wall motion in ultrathin Pt/Co/Pt films with perpendicular anisotropy*. Physical review letters, 2007. **99**(21): p. 217208.
40. Lemerle, S., et al., *Domain wall creep in an Ising ultrathin magnetic film*. Physical review letters, 1998. **80**(4): p. 849.
41. Metaxas, P.J., et al., *Creep and Flow Regimes of Magnetic Domain-Wall Motion in Ultrathin  $\text{Pt}/\text{Co}/\text{Pt}$  Films with Perpendicular Anisotropy*. Physical Review Letters, 2007. **99**(21): p. 217208.

42. Dzyaloshinsky, I., *A thermodynamic theory of "weak" ferromagnetism of antiferromagnetics*. Journal of Physics and Chemistry of Solids, 1958. **4**(4): p. 241-255.
43. Moriya, T., *Anisotropic Superexchange Interaction and Weak Ferromagnetism*. Physical Review, 1960. **120**(1): p. 91-98.
44. Fert, A. and P.M. Levy, *Role of Anisotropic Exchange Interactions in Determining the Properties of Spin-Glasses*. Physical Review Letters, 1980. **44**(23): p. 1538-1541.
45. D.M.F.Hartmann, *Domain-Wall Motion in Materials with Perpendicular Magnetic Anisotropy*, in *Institute for Theoretical Physics*. 2014, Utrecht University
46. André, T., et al., *Dynamics of Dzyaloshinskii domain walls in ultrathin magnetic films*. EPL (Europhysics Letters), 2012. **100**(5): p. 57002.
47. Thiaville, A., et al., *Dynamics of Dzyaloshinskii domain walls in ultrathin magnetic films*. EPL (Europhysics Letters), 2012. **100**(5): p. 57002.
48. Chen, G., et al., *Novel chiral magnetic domain wall structure in Fe/Ni/Cu (001) films*. Physical review letters, 2013. **110**(17): p. 177204.
49. Chen, G., et al., *Tailoring the chirality of magnetic domain walls by interface engineering*. Nature Communications, 2013. **4**: p. 2671.
50. Emori, S., et al., *Current-driven dynamics of chiral ferromagnetic domain walls*. Nature materials, 2013. **12**(7): p. 611.
51. Torrejon, J., et al., *Interface control of the magnetic chirality in CoFeB/MgO heterostructures with heavy-metal underlayers*. Nature Communications, 2014. **5**: p. 4655.
52. Yang, H., et al., *Anatomy of Dzyaloshinskii-Moriya Interaction at  $\text{Co/Pt}$  Interfaces*. Physical Review Letters, 2015. **115**(26): p. 267210.
53. Je, S.-G., et al., *Asymmetric magnetic domain-wall motion by the Dzyaloshinskii-Moriya interaction*. Physical Review B, 2013. **88**(21): p. 214401.
54. Hrabec, A., et al., *Measuring and tailoring the Dzyaloshinskii-Moriya interaction in perpendicularly magnetized thin films*. Physical Review B, 2014. **90**(2): p. 020402.
55. Lavrijsen, R., et al., *Asymmetric magnetic bubble expansion under in-plane field in Pt/Co/Pt: Effect of interface engineering*. Physical Review B, 2015. **91**(10): p. 104414.
56. Wells, A.W.J., et al., *Effect of interfacial intermixing on the Dzyaloshinskii-Moriya interaction in Pt/Co/Pt*. Physical Review B, 2017. **95**(5): p. 054428.
57. Yu, J., et al., *Spin orbit torques and Dzyaloshinskii-Moriya interaction in dual-interfaced Co-Ni multilayers*. Scientific Reports, 2016. **6**: p. 32629.
58. Kerr, J., *XLIII. On rotation of the plane of polarization by reflection from the pole of a magnet*. The London, Edinburgh, and Dublin Philosophical Magazine and Journal of Science, 1877. **3**(19): p. 321-343.
59. Schatz, P. and A. McCaffery, *The faraday effect*. Quarterly Reviews, Chemical Society, 1969. **23**(4): p. 552-584.
60. Bland, J.A.C., et al., *An intensity-stabilised He-Ne laser for measuring small magneto-optic Kerr rotations from thin ferromagnetic films*. Journal of Physics E: Scientific Instruments, 1989. **22**(5): p. 308.
61. Qiu, Z.Q. and S.D. Bader, *Surface magneto-optic Kerr effect*. Review of Scientific Instruments, 2000. **71**(3): p. 1243-1255.
62. Zak, J., et al., *Magneto-optics of multilayers with arbitrary magnetization directions*. Physical Review B, 1991. **43**(8): p. 6423-6429.

63. You, C.-Y. and S.-C. Shin, *Generalized analytic formulae for magneto-optical Kerr effects*. Journal of Applied Physics, 1998. **84**(1): p. 541-546.
64. You, C.Y. and S.C. Shin, *Derivation of simplified analytic formulae for magneto-optical Kerr effects*. Applied Physics Letters, 1996. **69**(9): p. 1315-1317.
65. Yang, Z.J. and M.R. Scheinfein, *Combined three-axis surface magneto-optical Kerr effects in the study of surface and ultrathin-film magnetism*. Journal of Applied Physics, 1993. **74**(11): p. 6810-6823.
66. Allwood, D., et al., *Characterization of submicrometer ferromagnetic NOT gates*. Journal of applied physics, 2004. **95**(12): p. 8264-8270.
67. Allwood, D., et al., *Submicrometer ferromagnetic NOT gate and shift register*. Science, 2002. **296**(5575): p. 2003-2006.
68. Dzyaloshinskii, I.E., *Theory of helicoidal structures in antiferromagnets. 1. Nonmetals*. Sov. Phys. JETP, 1964. **19**.
69. Moreau-Luchaire, C., et al., *Additive interfacial chiral interaction in multilayers for stabilization of small individual skyrmions at room temperature*. Nature Nanotechnology, 2016. **11**: p. 444.
70. Rößler, U.K., A.N. Bogdanov, and C. Pfleiderer, *Spontaneous skyrmion ground states in magnetic metals*. Nature, 2006. **442**: p. 797.
71. Nagaosa, N. and Y. Tokura, *Topological properties and dynamics of magnetic skyrmions*. Nature Nanotechnology, 2013. **8**: p. 899.
72. Sampaio, J., et al., *Nucleation, stability and current-induced motion of isolated magnetic skyrmions in nanostructures*. Nature Nanotechnology, 2013. **8**: p. 839.
73. Iwasaki, J., M. Mochizuki, and N. Nagaosa, *Current-induced skyrmion dynamics in constricted geometries*. Nature Nanotechnology, 2013. **8**: p. 742.
74. Heide, M., G. Bihlmayer, and S. Blügel, *Dzyaloshinskii-Moriya interaction accounting for the orientation of magnetic domains in ultrathin films: Fe/W(110)*. Physical Review B, 2008. **78**(14): p. 140403.
75. Bode, M., et al., *Chiral magnetic order at surfaces driven by inversion asymmetry*. Nature, 2007. **447**: p. 190.
76. Bandiera, S., et al., *Asymmetric Interfacial Perpendicular Magnetic Anisotropy in Pt/Co/Pt Trilayers*. IEEE Magnetics Letters, 2011. **2**: p. 3000504-3000504.
77. Lavrijsen, R., et al., *Asymmetric magnetic bubble expansion under in-plane field in Pt/Co/Pt: Effect of interface engineering*. Physical Review B, 2015. **91**(10): p. 104414.
78. Lavrijsen, R., et al., *Asymmetric Pt/Co/Pt-stack induced sign-control of current-induced magnetic domain-wall creep*. Applied Physics Letters, 2012. **100**(26): p. 262408.
79. Vaňatka, M., et al., *Velocity asymmetry of Dzyaloshinskii domain walls in the creep and flow regimes*. Journal of Physics: Condensed Matter, 2015. **27**(32): p. 326002.
80. Soucaille, R., et al., *Probing the Dzyaloshinskii-Moriya interaction in CoFeB ultrathin films using domain wall creep and Brillouin light spectroscopy*. Physical Review B, 2016. **94**(10): p. 104431.
81. Haazen, P.P.J., et al., *Domain wall depinning governed by the spin Hall effect*. Nature Materials, 2013. **12**: p. 299.
82. Mihai Miron, I., et al., *Current-driven spin torque induced by the Rashba effect in a ferromagnetic metal layer*. Nature Materials, 2010. **9**: p. 230.
83. Seo, S.-M., et al., *Current-induced motion of a transverse magnetic domain wall in the presence of spin Hall effect*. Applied Physics Letters, 2012. **101**(2): p. 022405.

84. Kim, K.-W., et al., *Magnetization dynamics induced by in-plane currents in ultrathin magnetic nanostructures with Rashba spin-orbit coupling*. Physical Review B, 2012. **85**(18): p. 180404.
85. Khvalkovskiy, A.V., et al., *Matching domain-wall configuration and spin-orbit torques for efficient domain-wall motion*. Physical Review B, 2013. **87**(2): p. 020402.
86. Bayreuther, G., et al., *Magnetic aftereffect in ultrathin ferromagnetic films*. Physical Review B, 1989. **40**(10): p. 7399-7402.
87. Lemerle, S., et al., *Domain Wall Creep in an Ising Ultrathin Magnetic Film*. Physical Review Letters, 1998. **80**(4): p. 849-852.
88. Kim, K.-J., et al., *Interdimensional universality of dynamic interfaces*. Nature, 2009. **458**: p. 740.
89. Khitun, A. and A. Kozhanov, *Magnonic Logic Devices*. Nanomagnetic and Spintronic Devices for Energy-Efficient Memory and Computing, 2016: p. 189.
90. Demokritov, S., et al., *Tunneling of dipolar spin waves through a region of inhomogeneous magnetic field*. Physical review letters, 2004. **93**(4): p. 047201.
91. Sadovnikov, A.V., et al., *Magnonic beam splitter: The building block of parallel magnonic circuitry*. Applied Physics Letters, 2015. **106**(19): p. 192406.
92. Wagner, K., et al., *Magnetic domain walls as reconfigurable spin-wave nanochannels*. Nature nanotechnology, 2016. **11**(5): p. 432.
93. Nanayakkara, K., A.P. Jacob, and A. Kozhanov, *Spin wave scattering and interference in ferromagnetic cross*. Journal of Applied Physics, 2015. **118**(16): p. 163904.

## APPENDICES

### Appendix A: Electromagnet design

#### Appendix A.1 FEMM simulations of magnetic field calculation for the designed electromagnet.

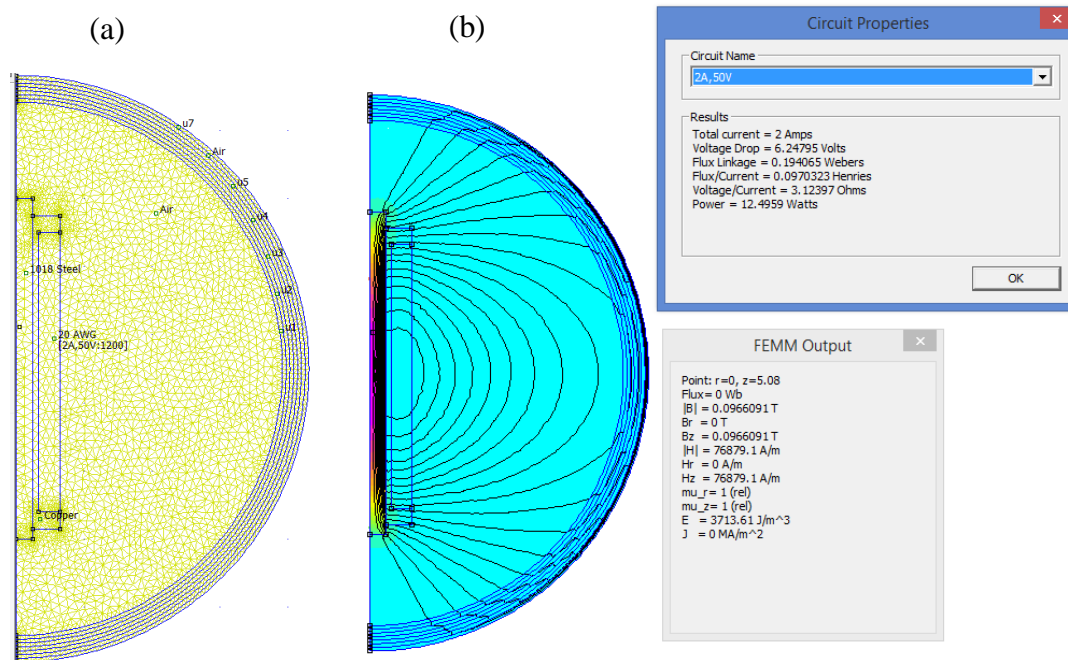


**Figure 0.1** FEMM simulations of electromagnet considering axisymmetric (a) Mesh generation and Material parameters. (b) Analysis results with the Flux density plot.

Finite element method magnetics (FEMM) which is an open source finite element analysis software is used to calculate the flux from the designed electromagnet. A 1018 steel rod with a 5 inch diameter was used as the electromagnet pole. An adapter spool with the same inner diameter was made from Cu, and 1100 turns of 20 AWG Cu wire was wound around the core. Driving 2.0 A, we obtained approximately 0.1 T magnetic field around 0.08 inches from the pole surface. A 2A, 50V power supply was used to drive the current in the electromagnet.

Appendix A.2 CAD designs of the electromagnet.

